Observing galaxies in the Southern Filament of the Virgo Cluster with KAT-7 and WSRT

Amidou Sorgho

University of Cape Town

A project submitted in partial fulfilment of the requirements for the degree M.Sc.
in the Department of Astronomy, as part of the National Astrophysics
and Space Science Programme
UNIVERSITY OF CAPE TOWN

Supervisors: Prof. C. Carignan, Prof. J. H. van Gorkom and Dr. K. M. Hess

The copyright of this thesis vests in the author. No quotation from it or information derived from it is to be published without full acknowledgement of the source. The thesis is to be used for private study or non-commercial research purposes only.

Published by the University of Cape Town (UCT) in terms of the non-exclusive license granted to UCT by the author.

University of Cape Town

Abstract

To date, our understanding of the formation and evolution of galaxies attributes a very important role to the neutral hydrogen (H I) gas since it constitutes the reservoir of fuel out of which galaxies form stars. In their evolution, galaxies interact with each other and with their environment, and very often these interactions leave fingerprints in the H I distribution. The extended H I envelopes of galaxies are sensitive tracers of those tidal interactions. In the present study, we map the H I distribution of galaxies in a ∼ 1.5° × 2.5° region of the Virgo cluster using the Karoo Array Telescope (KAT-7) and the Westerbork Synthesis Radio Telescope (WSRT). With a total observing time of ∼ 78 hours with the KAT-7 and 48 hours with the WSRT, we search for low H I column density features in the region. Despite the different observing time and beam size of the two telescopes, we reach similar column density sensitivities of $N_{\mathrm{HI}} \sim 1 \times 10^{18}\,\mathrm{atoms\,cm^{-2}}$ over $16.5\,\mathrm{km\,s^{-1}}$. With a new approach, we combine the two observations to map both the large and small scale structures. We detect, out to an unprecedented extent, an H I tail of ∼ 60 kpc being stripped off NGC 4424, a peculiar spiral galaxy. The properties of the galaxy, together with the shape of the tail, suggests that NGC 4424 is a post-merger galaxy undergoing a ram pressure stripping as it falls into the centre of the Virgo Cluster along a filamentary structure. We also give the H I parameters of the galaxies detected.

Acknowledgements

Foremost, I would like to express my deepest gratitude and special thanks to my supervisor, Prof. Claude Carignan. I thank him not only for all the support and understanding, but also for giving me the opportunity to consider a career in Astronomy.

I am deeply indebted to Dr. Kelley M. Hess for coaching me during my first steps in radio astronomy. A few brief sentences could not do her justice, so I will simply say to her *Thank you!*

Prof. Tom Oosterloo has played a tremendous role in the achievement of this thesis, I am grateful to him for providing us the WSRT data and helping me with the data reduction. I also thank Prof. Jacqueline van Gorkom for the X-ray data and all the advice she gave me. To Prof. Tom Jarrett I also give a big thank, for the 2MASS data and the fruitful discussions we had.

Dr. Danielle Lucero has been a support throughout my thesis, I cannot thank her enough.

This work has been performed through the National and Space Science Programme (NASSP) and was funded by the National Research Fund (NRF). Additional funding was received from the South African Square Kilometre Array (SA SKA) project.

Plagiarism Declaration

I, Amidou Sorgho, know the meaning of plagiarism and declare that all of the work in the document, save for that which is properly acknowledged, is my own.

Contents

List of Figures

List of Tables

Introduction

In the history of radio astronomy, several telescopes were built to carry specific science, in both single dish and interferometers. Different HI surveys such as the The HI Nearby Galaxy Survey (THINGS, Walter et al. 2008), the Arecibo Legacy Fast ALFA (ALFALFA, Haynes et al. 2011), the HI Parkes All Sky Survey (HIPASS, Meyer et al. 2004) and the COSMOS HI Large Extragalactic Survey (CHILES, ongoing survey, see Fernández et al. 2013 for pilot survey) revealed different properties of galaxies in the local universe. Although these surveys are limited to low redshift (CHILES aims to detect out to $z = 0.45$), they give us tremendous informations about galaxy evolution, in combination with numerical models.

However, the challenge in HI observations is not only the detection of neutral gas inside galaxies, but also in their outer regions. The HI usually happens to be faint in the outskirts of galaxies, which makes their detection more complicated. This therefore requires adapted instruments. The Karoo Array Telescope (KAT-7) is a newly built telescope in South Africa, designed to be an early precursor and testbed for the Square Kilometre Array (SKA). Its short baselines allow the telescope to be sensitive to low surface brightness structures.

The project of this thesis is to perform deep observation on a field of galaxies in the Virgo Cluster containing galaxies undergoing environmental effects. To reach low column density levels, we use the short-baselined KAT-7 telescope. Although KAT-7 allows us to detect the structure of galaxies on large scale, it fails to reveal their fine details. We therefore decide to combine the KAT-7 observations to data obtained with the Westerbork Synthesis Radio Telescope (WSRT), an interferometer with higher spatial resolution. This is the first time that such work is attempted with KAT-7. Combination of data from different telescopes is generally performed between interferometers and single-dish telescopes (e.g. Stanimirovič 1999), and these processes are implemented in most data reduction packages (e.g. MIRIAD, CASA). On the other hand, combination of different interferometric data is not widely attempted. Because of the large difference in the respective beam areas of the two different interferometers, the process presents some challenges on how to weight the respective datasets to account for the different features from both telescopes.

Chapter 1

Astrophysical context

1.1 The Cosmic Web

Observational evidence strongly suggests that the matter distribution of the Universe on large scales is not uniform, but forms a complex web-like pattern, known as the *Cosmic Web* (Bond et al. 1996, van de Weygaert & Bond 2008), containing dense clusters, sparsely populated voids, planar walls and thread-like filamentary structures linking overdense regions. Over time, numerical simulations such as the Millenium simulations (Springel et al. 2005, Boylan-Kolchin et al. 2009) and large surveys in the Local Universe such as 2dFGRS (Colless et al. 2001), SDSS (York et al. 2000) and 2MASS redshift survey (Huchra et al. 2005) have helped reveal the geometry and dynamics of the cosmic web. More recently, Cautun et al. (2014) found that clusters and filaments are the most prominent components of the cosmic web, while underdense voids and walls – devoid of group-sized and more massive haloes – occupy most of the volume. Most of the baryonic matter is then expected to be found in filaments and clusters.

However, only a small fraction of all baryons at the current epoch (as predicted by models) can be recovered by adding up the masses of visible baryons (Persic & Salucci 1992, Fukugita et al. 1998, Fukugita & Peebles 2004), suggesting that a fraction of the baryons making up the Universe is unseen. An ultraviolet spectroscopic survey of HI Lyman lines and metal ions in the low-redshift at $z < 0.4$ (Danforth & Shull 2008) revealed only about 40% of the baryons, with 30% residing in Lyα forest and 10% in the warm-hot intergalactic medium (WHIM). The WHIM, with temperatures ranging from 10^5 to $10^7\,\mathrm{K}$, is thought to contain approximately 30% to 40% of all baryons in the present-day universe (Davé et al. 2001). Although observational detections of the WHIM have been reported in QSO absorption using different lines (e.g., Tripp et al. 2000, Fang et al. 2002, Nicastro et al. 2005), its direct detection in emission remains very difficult. The presence of the WHIM is more inferred from hydrodynamical simulations (e.g., Cen et al. 1995, Cen & Ostriker 1999, Davé et al. 1999; 2001, Fang et al. 2005) to account for the missing fraction of the baryons. Simulations go further to predict that most of the warm-hot gas is not expected to be found in dense IGM regions but in diffuse, less dense large-scale structures such as filaments (Davé et al. 2001).

1.2 The 21-cm line of neutral hydrogen

In the low-density regions of the interstellar medium (ISM) and below about 10^4 K, the hydrogen exists in its atomic form, the HI, which is detectable in the $\lambda 21\,\mathrm{cm}$ hyperfine line. First predicted by van de Hulst (1945) and later detected by Ewen & Purcell (1951), the line is a product of the magnetic interactions between the proton and electron of the atom. It results from a forbidden spin-flip transition in the ground state of the hydrogen atom. The transition occurs very rarely, its spontaneous emission rate is only $\sim 1/11\,\mathrm{Myr}$; however, the enormous column densities of atomic hydrogen in the ISM – and often in the intergalactic medium (IGM) – makes its detection possible.

Since its discovery, the HI line has widely been used to study the neutral gas in galaxies, including our own. Unlike the traditional optical observations (excluding the Fabry-Pérot), the HI line provides, on top of the 2-dimensional images of emitting gas, information about their velocity thanks to the Doppler shift. On one hand, this provides important information on the physical properties of the interstellar gas such as its size and density; and on the other hand, it allows us to study the associated kinematics of the ISM. Moreover, the 21-cm emission is optically thin, implying that one can directly convert the total amount of HI seen along a particular line of sight into an HI mass density. Hence, integrating over an entire galaxy, one can determine its total HI mass (see Eq. 4.3).

There exist many advantages in using the HI line for galactic and extragalactic studies. One of them is certainly the fact that the HI emission does not suffer from extinction by stellar dust (unlike optical or ultraviolet radiation), making the HI line a powerful tool in mapping the extragalactic gas. Its observations can also in principle be done, in contrast to most of other frequency bands, in the day as well as at night. However, day observations are often affected by solar interference, especially when the source is located near the sun.

1.3 HI gas in galaxies

Despite the complexity of its study, neutral atomic hydrogen remains the easiest observable component of the ISM in galaxies. The hydrogen remains abundant in the ISM and in the IGM, though it very often happens to be mostly ionised. While the stellar and other baryonic components of galaxies are confined to their disks, the HI generally extends far beyond. This makes the HI gas a sensitive tracer of past and current interactions of galaxies with their environment, since most interactions happen at large scale.

Moreover, star formation in disks of galaxies from cold molecular clouds is made possible thanks to the surrounding atomic gas, distributed in extended envelopes. These envelopes of atomic gas constitute the reservoir of gas out of which stars are formed, making the HI content a proxy for a star formation potential of galaxies. Thus, the atomic gas quantity inside galaxies becomes important in the study of the galaxy formation and evolution.

The hierarchical models describing galaxy evolution (e.g. White & Rees 1978, White & Frenk 1991, Springel et al. 2005) suggest that large galaxies result from mergers between smaller galaxies which, supposedly, are formed from gas clouds that – under gravity – collapse to form star forming discs (Eggen et al. 1962). When the merger occurs between a pair of late-type, blue spiral galaxies, the resulting galaxy is generally (depending of the relative size of the merging galaxies) an early-type, red elliptical galaxy (Toomre & Toomre 1972, Mihos & Hernquist 1996). The HI in these elliptical galaxies is barely existent, as this was depleted during the high star formation activity and tidal interactions that took place during the merger. In contrast, spiral galaxies that have not undergone these processes are expected to have a relatively large amount of neutral gas. This dependence of neutral gas content on morphological type is confirmed by observations.

Furthermore, as first noted by Hubble & Humason (1931) and later quantified by Dressler (1980), and known as the "morphology-density" relation, galaxies exhibit a clear trend between their morphological type and the density of the region they evolve in. In this picture, early-type elliptical and lenticular galaxies tend to reside in the dense regions of clusters while the late-type spirals and irregulars are more likely to be found on the outskirts. Nonetheless, although late-type galaxies are outnumbered by early-type galaxies in clusters, they do generally exist in the outskirts. When this is the case, they undergo different environmental effects traceable through the observation of their HI component as mentioned above.

1.4 Effects of environment on the HI gas

What is the physical origin of the morphology-density relation? The answer to this question is still a subject of debate in extragalactic astronomy. The first hypothesis, the so-called *nature* hypothesis, supports that the observed relation surfaces during galaxy assembly, the process being different in overdense regions. On the other hand, the *nurture* hypothesis argues that the trend is the end product of the different physical processes caused by the environment. Although recent studies show evidence that both *nature* and *nurture* are important in galaxy evolution and are intertwined (see Kauffmann et al. 2004, De Lucia et al. 2012), there is a tremendous amount of evidence in favour of an environment-driven evolution of galaxies.

Indeed, numerous studies based on both observations and simulations have come to the conclusion that the environment plays a critical role in the evolution of galaxies (e.g. Dressler 1980, Catinella et al. 2013).

Whether a galaxy resides in a dense region such as a cluster or a group, it undergoes different effects that determine its morphology and gas properties. For example, galaxies evolving in dense environments tend to be HI deficient with respect to their morphological counterparts evolving in less dense regions (Haynes et al. 1984a).

1.4.1 Effects of clusters

More specifically in clusters of galaxies, the small scale structure ISM of spiral galaxies interacts with the large scale structure intra-cluster medium (ICM) through physical processes that drive the evolution of the galaxies inside clusters. The most widely known process is the ram pressure stripping (e.g. Gunn & Gott, J. Richard 1972, Vollmer et al. 2001). It occurs when a galaxy moves through the ICM of a galaxy cluster, and is known to be partly responsible for the HI deficiency (Bothun et al. 1982, Giovanelli & Haynes 1985, Vollmer et al. 2001) and star formation quenching (e.g. Balogh et al. 2000) inside spiral galaxies in clusters. More specifically, ram pressure occurs when the intra-cluster 'wind' experienced by the moving galaxy is strong enough to overcome the gravitational potential of the galaxy. As a consequence, the galaxy is deprived of its cold gas, especially at its regions in contact with the hot wind. Typical examples of galaxies undergoing ram pressure stripping include NGC 4522 (Kenney et al. 2004, Vollmer et al. 2004) and NGC 4402 (Crowl & Kenney 2005).

Although this effect is strongest in the central regions of clusters, cosmological simulations reveal that it remains an important mechanism of gas stripping of galaxies out to the virial radius of clusters (Tonnesen et al. 2007). This was seen in observations when Chung et al. (2007) mapped the neutral gas in a few Virgo galaxies with long one sided HI tails. The authors found that some galaxies, located at projected distances of $0.6 - 1$ Mpc from the cluster centre (M87), exhibit an HI tail extending beyond the optical disc and on one side of the galaxy, and pointing roughly away from M87 (see figure 1.1). After investigation of the different mechanisms that might cause these tails, they concluded that these galaxies are most likely falling into the cluster for the first time, and are being ram-pressure-stripped of their gas at a virial radius from the cluster centre. More generally, ram pressure stripping starts once galaxies on highly radial orbits are within a virial radius of the cluster they are falling into.

Another major process driving the morphological evolution of galaxies in clusters is the repeated galaxy-galaxy interactions, or the galaxy "harassment" (Moore et al. 1996; 1998). Unlike the ram pressure stripping, these interactions have the ability to transform disk galaxies into spheroidal galaxies by affecting not only the gas, but also the stellar disk through dynamical heating.

1.4.2 Effects of groups

Groups of galaxies constitute intermediate systems between the extreme voids and galaxy clusters, and are moderately populated of a few to hundred gravitationally bound galaxies. But unlike clusters, groups are difficult to identify mainly because of their lower concentration (and therefore lower amount of detectable, hot X-ray emitting gas in comparison to clusters). Over the three last decades or so, group-finding techniques have been applied to optical and infrared all-sky redshift surveys to construct group catalogues (Geller & Huchra 1983, Giuricin et al. 2000, Crook et al. 2007, Dawson et al. 2013) and it is argued that over half of all galaxies live in the group environment (Eke et al. 2004). There is also observa-

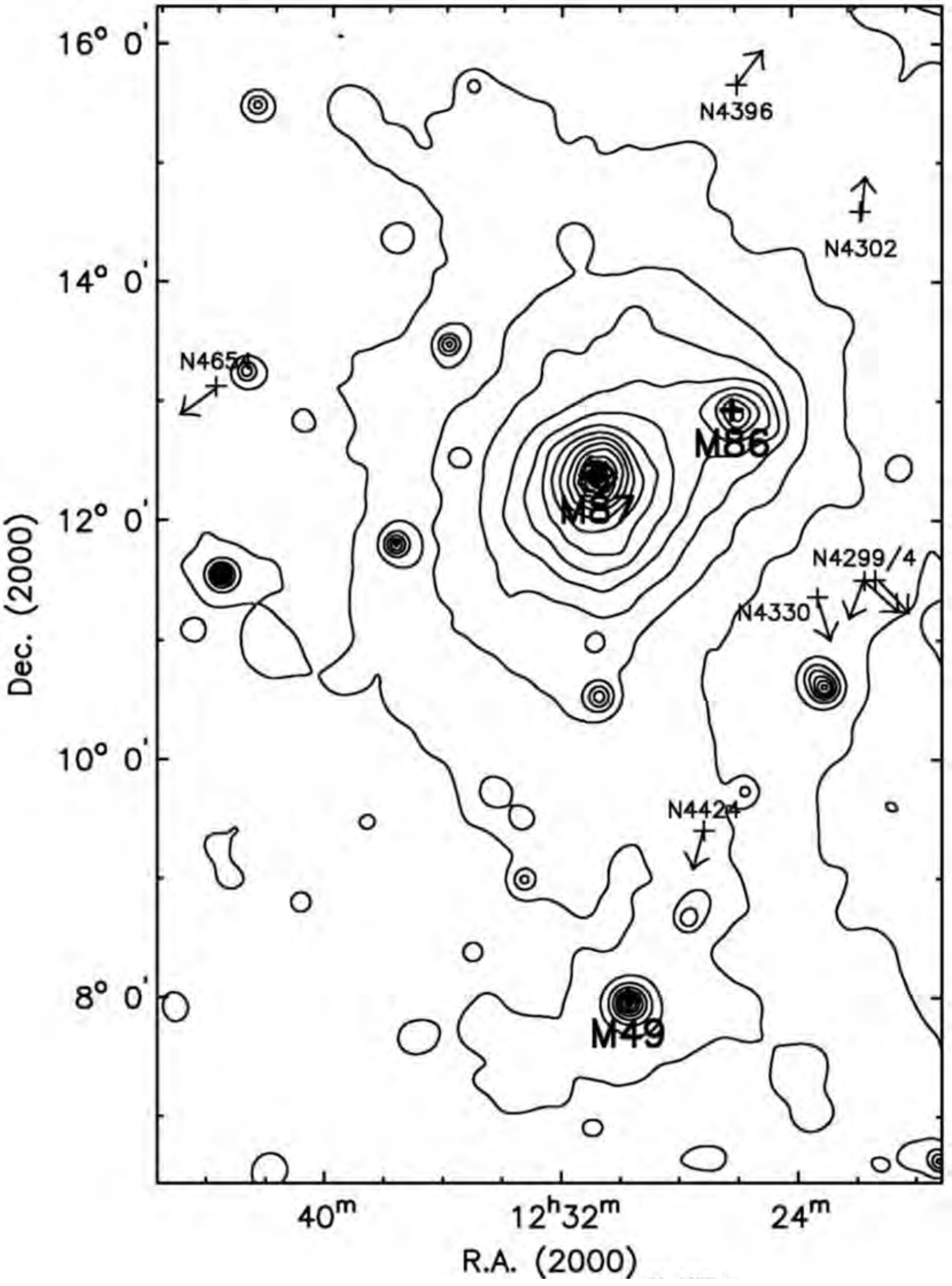

Figure 1.1: HI tail galaxies in the Virgo Cluster (crosses) and the direction of their tails (arrows) on the X-ray background of the cluster. As one can clearly see, the tails are pointing roughly away from the central elliptical M87, suggesting that the galaxies are falling into the centre of the cluster. Figure from Chung et al. (2007)

tional evidence that galaxies residing in group-like densities, like those in clusters, present a lower SFR (e.g. Lewis et al. 2002, Gomez et al. 2003, Rasmussen et al. 2012) than field galaxies, suggesting a star formation suppression happening inside groups.

In recent years, studies of groups from the HI emission perspective were intensified to understand their contribution to the evolution of galaxies (e.g. Pisano et al. 2007; 2011, Freeland et al. 2009, Rasmussen et al. 2012, Hess & Wilcots 2013) and these allowed us to take a step forward in understanding the impact of environment on galaxy evolution. There is for example strong evidence that many galaxies experience, before falling into clusters, some high-density environment effects as group members. This process, known as "pre-processing" (Zabludoff & Mulchaey 1998, Mahajan 2013, Hess & Wilcots 2013, Vijayaraghavan & Ricker 2013), places group environments at the origin of the properties of an important fraction of galaxies observed at present time in clusters. This comes as a major piece of the puzzle of galaxy evolution and attributes an important role to groups of galaxies in this process.

Groups – especially poor groups – are, on the other hand, the most favorable environment for mergers between galaxies because of their low velocity dispersion and their short crossing time (Zabludoff & Mulchaey 1998, Mamon 2007, Vijayaraghavan & Ricker 2013). These mergers, along with the tidal interactions acting on galaxies, seem to be efficient in removing the hot gaseous halo of galaxies in groups (Larson et al. 1980, McCarthy et al. 2008, Kawata & Mulchaey 2008). The resulting effect of these on the HI content of group galaxies is, as in cluster environments, the HI deficiency. Kilborn et al. (2009) found that an important fraction of HI deficient spirals lie within about 1 Mpc of group centres, suggesting that group environment increases the gas loss. In addition, how much HI rich galaxies can be found in a group depends on its size: Hess & Wilcots (2013) found that HI rich galaxies in the centre of groups become rarer as their number of optical members increases.

1.5 Galaxies in large scale filaments

While the characteristics of galaxies in dense environments seem well understood, a complete picture of galaxy evolution remains far from being found. For example, the mechanisms leading to the growth and depletion of the cold gas and star formation quenching in galaxies are not fully understood, though numerical simulations are helping improve our understanding.

The structure of the universe, as per our current understanding, suggests that galaxy clusters and superclusters are connected by filamentary structures (e.g., Zeldovich et al. 1982, Jenkins et al. 1998). Hierarchical models and observations also suggest that clusters feed from accretion of small galaxies through these filaments (e.g., Zabludoff & Franx 1993, Benson 2005, Cortese et al. 2006). Furthermore, numerical simulations predict that most of the low redshift baryonic matter is hidden in the filaments (Cen & Ostriker 1999, Davé et al. 1999; 2001). Filaments, through their constituent galaxies and also their IGM, are therefore key structures in understanding evolution of galaxies in dense environments.

Several wide-field surveys in different wavelengths such as optical (Pimbblet et al. 2004, Molinari et al. 2010, Alpaslan et al. 2013, Cantalupo et al. 2014), infrared (Fadda et al. 2008) and HI (e.g., Haynes et al. 2011), have reported the detection of large-scale filaments in the local universe by mapping the distribution of galaxies. It is found that galaxies located in filaments show an enhanced star formation activity (e.g. Raychaudhury & Porter 2005, Fadda et al. 2008, Porter et al. 2008) compared to those in other regions, which is in agreement with our current understanding of galaxy evolution, which correlates with the picture that galaxies falling into clusters through filament undergo an accelerated evolution at some stage of their infall during which they experience a short period of starburst. However, despite the membership of a galaxy to a filament, its star formation activity is still influenced by its local density and morphological type (e.g., Mahajan 2011).

1.6 Low-density gas in filaments

The low column density neutral gas, spanning a column density range of about 10^{14} to $10^{19}\,\mathrm{cm}^{-2}$, has an important fraction in the Lyman Limit regime at column densities of $\gtrsim 10^{17}\,\mathrm{cm}^{-2}$ (see e.g. Péroux et al. 2003). This implies that, in hope to detect the filamentary neutral gas, one must go to a very low column density, which is a limitation to most of radio telescopes. Using the WSRT, Braun & Thilker (2004) carried a wide-field survey of HI emission feature and reported the detection of a diffuse filament between M31 and M33 at $N_{\mathrm{HI}} = 5 \times 10^{17}\,\mathrm{cm}^{-2}$ (Fig. 1.2) which might be associated with the WHIM predicted by numerical models (Davé et al. 1999; 2001).

1.7 Extended HI Envelopes around galaxies

The HI gas in late-type spiral galaxies is generally known to extend beyond their stellar disks, however, how far beyond it extends is function of the environment. In the less dense gas-rich regions, some galaxies exhibit large HI envelopes that can extend out to 5 times the optical radius (Chin & O'Neil 2000) and in some cases, connect the galaxies to their interacting neighbours (e.g. NGC 4490/85 system, Clemens et al. 1998). Extended HI envelopes are believed to be a source of gas replenishment in most spiral galaxies, when their star formation activities deplete the gas (Larson et al. 1980, Heald et al. 2011, Wang et al. 2013).

The observation of extended HI envelopes undoubtedly offers a unique opportunity to practically investigate the interactions that galaxies undergo with their environment. It also provides one of the most direct methods to determine the mass distribution of a galaxy, by allowing the measurement of its circular velocity in the very outer parts. However, extended HI envelopes are not common around galaxies (Briggs et al. 1980), even in HI-rich environments. Moreover, most galaxies present a sharp cutoff in their HI distribution at their outer disks, resulting in a dramatic drop of their column density at values below $10^{19}\,\mathrm{cm}^{-2}$. These sharp edges, which could be the result of extragalactic photoionisation as first proposed by Silk & Sunyaev (1976), are better illustrated in Figure 1.3 from Dove & Shull (1994). The figure compares the predicted HI column density in galaxies as a function

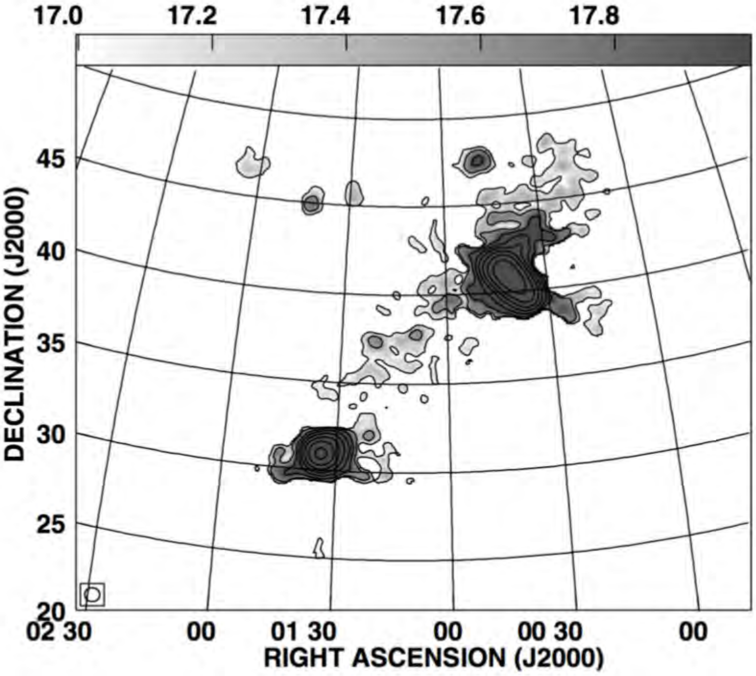

Figure 1.2: Filamentary low HI column density feature detected between M31 *(top right)* and M33 *(bottom left)* by Braun & Thilker (2004). The contours levels are $\log N_{\rm HI}$ = 17, 17.5, 18, ...20.5. Figure from Braun & Thilker (2004).

of their radius from a photoionisation model using different ionising photon fluxes (*lines*), with HI observations of NGC 3198 (*filled dots*). The top solid line is the total hydrogen of the galaxy. In the inner region of the galaxy, the column density of the atomic gas is more or less similar to the total column density because the gas in these dense environments is dominated by self-shielding (i.e, very few photons can reach these regions to ionise the gas). However, as we move to the outer parts, the HI column density decreases more rapidly than the total column density, owing to the decrease of the effect of self-shielding. More photons can penetrate the external regions of the galaxy, hence increase the fraction of ionised hydrogen in these regions. Moreover, an increase in the ionising photons flux causes the effect of self-shielding to decrease, creating a rapid decline of the neutral gas column density. This emphasises the importance of photoionisation as cause of sharp edges in galaxies.

van Gorkom (1991) also observed NGC 3198 and found that the HI column density drops from a few times $10^{19}\,\mathrm{cm}^{-2}$ to less than $4 \times 10^{18}\,\mathrm{atoms\,cm}^{-2}$ in only less than 3 kpc. As mentioned above, this can be attributed to the photoionisation effects observed in hydrogen. It constitutes a limitation in observing the HI on large scales around galaxies, especially with long baseline telescopes which are less sensitive to low surface brightness structures.

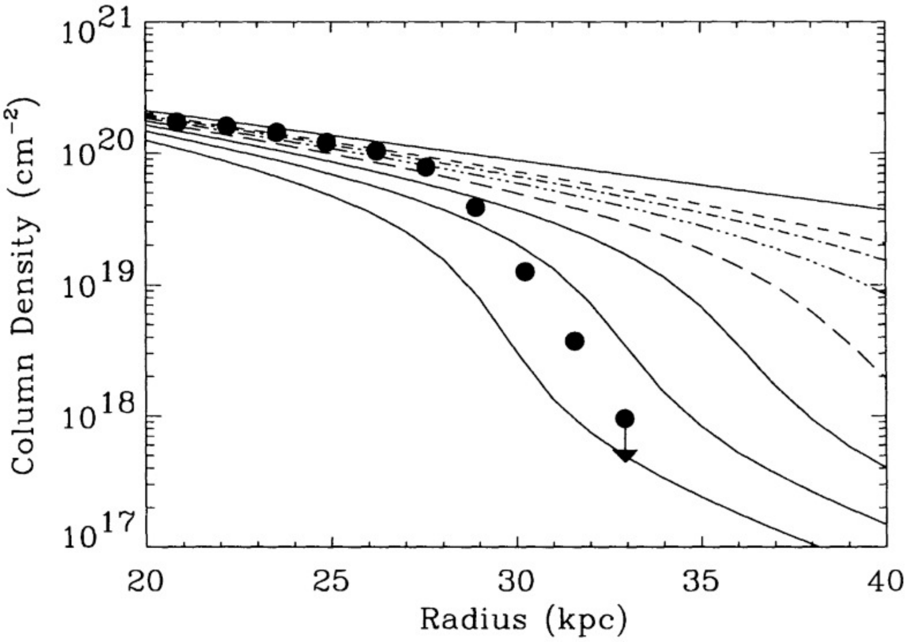

Figure 1.3: Column density vs. radius of total hydrogen *(top solid line)*, modelled HI with different ionising photon fluxes *(other lines)*, and observed HI in NGC 3198 *(filled dots)*. For the model, the ionising photon fluxes increase from top to bottom. Figure adapted from Dove & Shull (1994)

1.8 This thesis

It is clear that the mechanisms driving the evolution of galaxies in dense environments are diverse and complex. These mechanisms contribute to both the growth and the depletion of the gas reservoir of galaxies, hence affect their evolutionary paths. Observations of the gas in these environments offer a window to test numerical simulations and models, and therefore set better constrains on the theories of galaxy evolution. In particular the neutral gas provides an opportunity to map the outer regions of galaxies and their surrounding environment, allowing us to directly probe their interactions with the IGM and with their neighbours.

In this thesis we use the KAT-7 and WSRT telescopes to observe a region of the M49 subcluster located south of the Virgo Cluster. It is a rich and dynamically young cluster, hosting a number of interacting galaxies. The distribution of the hot X-ray emitting gas in the observed region resembles a filamentary structure, connecting the subcluster to the main cluster. Also, the region contains an HI-tailed spiral galaxy, NGC 4424, that shows signs of interaction with the ICM. In attempt to map the low surface brightness structures, we observe the region down to sensibly a same column density with the two telescopes.

This thesis is organised as follows. In chapter 2 we describe the observations and present the characteristics of the observed region. Chapter 3 gives an overview of the reduction of the data from the two different telescopes, and describes the technique we used to combine them. The results of the work are presented in chapter 4. In chapter 5 we discuss and analyse the results. Infrared data are combined to the HI observations to study the star formation rates of the galaxies detected, and the environmental effects are investigated. Finally, we conclude in chapter 6 and give an outline of the future work.

Chapter 2

Observational technique

The data presented in this thesis have been obtained using two different interferometers: the Karoo Array Telescope (KAT-7*) in South Africa and the Westerbork Synthesis Radio Telescope (WSRT) in The Netherlands.

2.1 The Karoo Array Telescope (KAT-7)

2.1.1 Specifications

The KAT-7, completed in December 2010, is made of seven 12m dishes and is a prototype and testbed of the MeerKAT, which is itself a precursor of the Square Kilometre Array (SKA†). The MeerKAT‡, on its completion by 2017, will have a total of 64 dishes. The KAT-7 is located in the desert of the Karoo in South Africa. An advantage of KAT-7 is its short baselines, together with its low system temperature ($T_{\rm sys} \sim 30\,K$), that make the interferometer sensitive to low surface brightness structures, and its large primary beam (FWHM = 1.08°) that gives a wide instantaneous field of view. One drawback though is the beam dilution that may occur when observing small scale structures, because of the low spatial resolution. Table 2.1 summarises the KAT-7 parameters. The telescope is for now equipped with one receiver whose waveband ranges from 1.2 to 1.95 GHz. Its 3 outermost antennas form an almost equilateral triangle, while its 4 innermost form a trapezoid (figure 2.1).

2.1.2 Radio Frequency Interference

Radio frequency interference (RFI) constitutes one of the major issues that one has to account for when building a radiotelescope. Especially human-made RFIs, which are generated by different sources ranging from cellphones to airports, including orbiting satellites. Fol-

---

[*] http://www.ska.ac.za/meerkat/kat7.php

[†] http://www.skatelescope.org

[‡] http://www.ska.ac.za/meerkat/

Table 2.1: Specifications of the KAT-7 (Carignan et al. 2013) and the WSRT interferometers (see WSRT documentation).

Parameter	KAT-7	WSRT
Number of antennas	7	14
Dish diameter	12 m	25 m
Minimum baseline	26 m	36 m
Maximum baseline	185 m	2.7 km
Frequency range	1.2∼1.95 GHz	115 MHz − 8.6 GHz
System temperature	26 K	∼ 27 K
Aperture efficiency	65%	54%
Primary beam (at 1.4 GHz)	1.08°	30′
System sensitivity	37.54 Jy K^{-1}	10.41 Jy K^{-1}

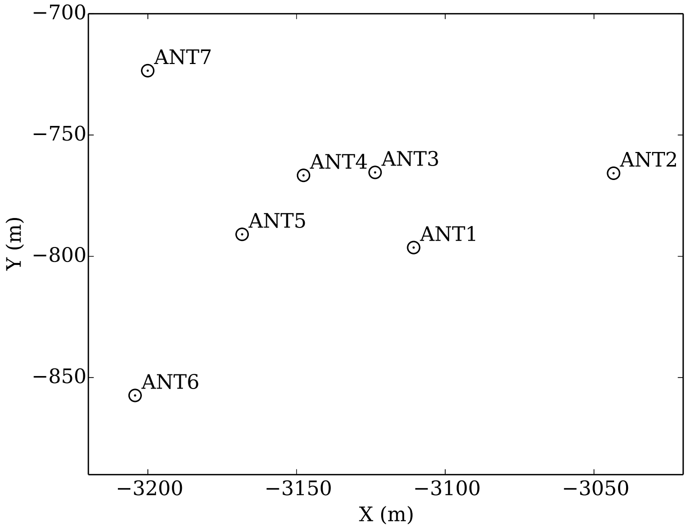

Figure 2.1: KAT-7 antennas positions.

lowing this issue, the KAT-7 was built in the far desert of the Karoo, where noise sources are rare. The site of the telescope is, like most of the radiotelescope sites, radio-quiet (radio-transmitting devices are not allowed on site); allowing to minimise as much as possible the interferences. However, a major source of RFI that remains hard to eliminate are the global positioning satellites, that are seen by all radio telescopes regardless of where they are built.

Nonetheless, since the KAT-7 is still in the commissioning phase, the response of the telescope is not fully understood and not all the RFI sources are known. This implies that a careful and interactive RFI flagging has to be performed whenever one intends to reduce radio data from the KAT-7.

2.1.3 Sensitivity

The KAT-7, like any other interferometer, works on the two-element basis. Indeed, the 7 antennae of the telescope are connected to one another, forming a set of 21 baselines (each

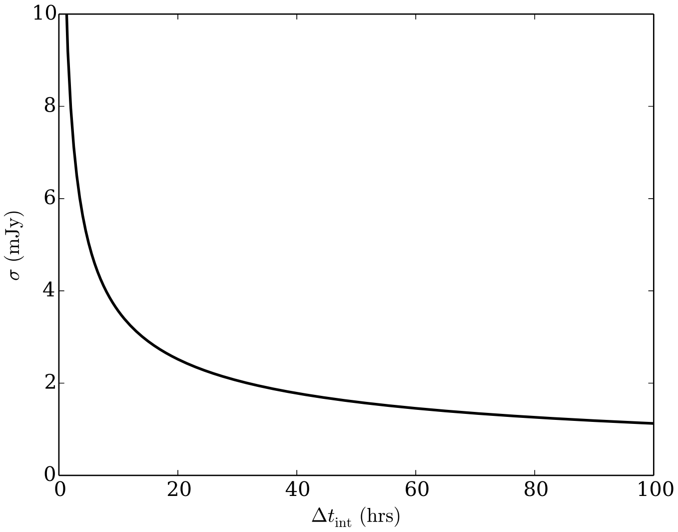

Figure 2.2: Point source sensitivity of the KAT-7 vs. total integration time per pointing.

baseline being a pair of two antennae). An interferometric data is a combination of the data collected by each of the single baselines.

The expected point-source *rms* noise of an output image of the KAT-7 can be approximated to

$$\frac{\sigma}{\mathrm{mJy}} = \frac{1.065 \times 10^5}{\sqrt{\Delta\nu \, \Delta t_{\rm int}}} \tag{2.1}$$

where $\Delta\nu$ is the channel bandwidth in Hz, and $\Delta t_{\rm int}$ the total integration time per pointing, in seconds. Figure (2.2) gives the *theoretical* variation of the noise as a function of the integration time, for the 25MHz band. The above equation does not account for atmosphere influence and various factors that would contribute in increasing the noise, and would therefore represent *ideal* noise level.

2.2 The Westerbork Synthesis Radio Telescope

2.2.1 Specifications

The construction of the Westerbork Synthesis Radio Telescope (WSRT) was completed in 1970 but it has been upgraded since then. Its primary beam FWHM at 1.4 GHz is $\sim 30'$, roughly half that of KAT-7. It covers the frequency band ranging from as little as 115 MHz to 8.6 GHz.

To date, the interferometer is made up of 14 dish-shaped antennas of 25m each. The array of these antennas has a linear structure in the East-West direction. The advantage of such configuration is that it offers long baselines, i.e, the high resolution data. However, observations at low elevations in the East-West direction result in an elongated synthesised beam (see 3.3.3).

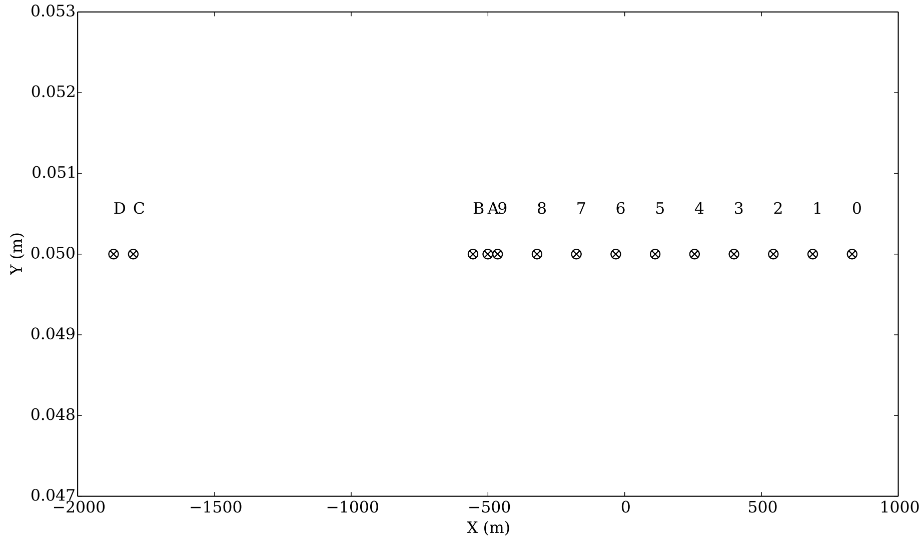

Figure 2.3: Antenna layout of the WSRT array in the *Maxi-Short* configuration. The variations of the y coordinates were neglected to show the linear configuration of the array. The labels show the RT identifiers of the anntennas.

Unlike the KAT-7, the WSRT's antennas are not all fixed: only 10 of the 14 dishes are fixed, at 144 m apart and spanning a total of 1.3 km; the 4 others are movable along the direction of the baselines, in such a way that the baselines are adjustable from 36 m to 2.7 km. The spacing between the last fixed antenna, RT9, and the first movable antenna, RTA, and the relative spacing between the 4 movable antennas determine the configuration of the array. Thus, there exist a total of 5 major types of configurations. Among these types of configurations, are the one in which RT9 and RTA have a particular separation, while the 2 pairs of movable antennas, RTA-RTB and RTC-RTD, are each kept at a fixed separation of 72m; moreover, the RTC-RTD pair is such that the separation RT9-RTC is $\sim$ 1.3 km (9×144 m). These configurations, called "traditional" configurations and designed to provide the best u, v sampling for 12h runs, are the most suitable configurations for observations exceeding 12h per pointing (see e.g. Dahlem et al. 2005). The second configuration, used in the present work, is the *Maxi-Short* configuration. It uses the shortest baselines possible, providing an optimum imaging performance for very extended sources within a single track observation. The positions of the movable antennas in this configuration are such that the distances RT9-RTA, RT9-RTB, RT9-RTC and RT9-RTD are 36, 90, 1332 and 1404m, respectively. The drawback of this configuration is the relatively high overall sidelobe levels in the reconstructed image.

2.2.2 Sensitivity

Although the WSRT is less brightness sensitive compared to the KAT-7, its larger collecting area and higher angular resolution result in a much greater point-source sensitivity. For example, for a 12h observation with a L-band 20 kHz bandwidth (i.e, a $\sim 4.1\,\mathrm{km\,s^{-1}}$ channel width), the expected *rms* noise is only $0.9\,\mathrm{mJy\,beam^{-1}}$ per channel while that of the KAT-7 approximates $4\,\mathrm{mJy\,beam^{-1}}$ per channel.

2.3 The observations

2.3.1 The field selection

In the present work, we study a region located in the outskirts of the Virgo Cluster, containing a modest number of late-type galaxies. Nucleus of the Local Supercluster, the Virgo Cluster is the nearest and best-studied cluster of galaxies. The observations of the cluster's members goes back as early as 1784 with Charles Messier, and since Hubble's discovery of the Andromeda Galaxy (Messier 31, member of the Local Group) as an extragalactic object, the interest for the Virgo Cluster continued increasing. To date, about 1300 galaxies have been identified, based on their morphology and radial velocities, as true members of the Virgo Cluster (e.g. Sandage et al. 1985, Binggeli et al. 1987). The six biggest ellipticals of the cluster are members of the Messier Catalogue, namely M85, M86, M84, M87, M60, and M49. M87 is the central dominant galaxy of the cluster, and is located $\sim 1^\circ$ southeast of the cluster's centre. The recession velocity of the cluster is about $1050\,\mathrm{km\,s^{-1}}$, and its velocity dispersion is about $700\,\mathrm{km\,s^{-1}}$ (Binggeli et al. 1993). Detailed X-ray observations of the hot cluster gas by Böhringer et al. (1994) revealed several substructures, suggesting that the cluster is not virialised, but is instead still growing. They found that subclusters around M86 and M49 are merging with the main cluster around M87 (see Fig 2.4). Several HI imaging surveys of the cluster revealed that the HI disks of its central late-type galaxies are truncated to well within the optical disks, suggesting that ICM - ISM interactions might play an important role in driving the evolution of galaxies in the inner region of the cluster (Warmels 1988, Cayatte et al. 1990, Chung et al. 2009).

The field of interest for the present work is a region in the M49 subcluster. It is located south of the Virgo Cluster, $\sim 3^\circ$ away from the elliptical M87, and contains the elliptical M49 (see Fig 2.4). The field also contains the one-sided HI tail galaxy, NGC 4424, previously observed using the VLA (Chung et al. 2007; 2009). We attempt to map late-type galaxies in the region, and study their properties with respect to what seems to be a filament connecting the subcluster to the main cluster.

2.3.2 The KAT-7 observations

The KAT-7 observations were conducted between July 2013 and May 2014 during a total of 18 sessions. Among these 18 sessions, 14 were done at night and 4 during the day. These

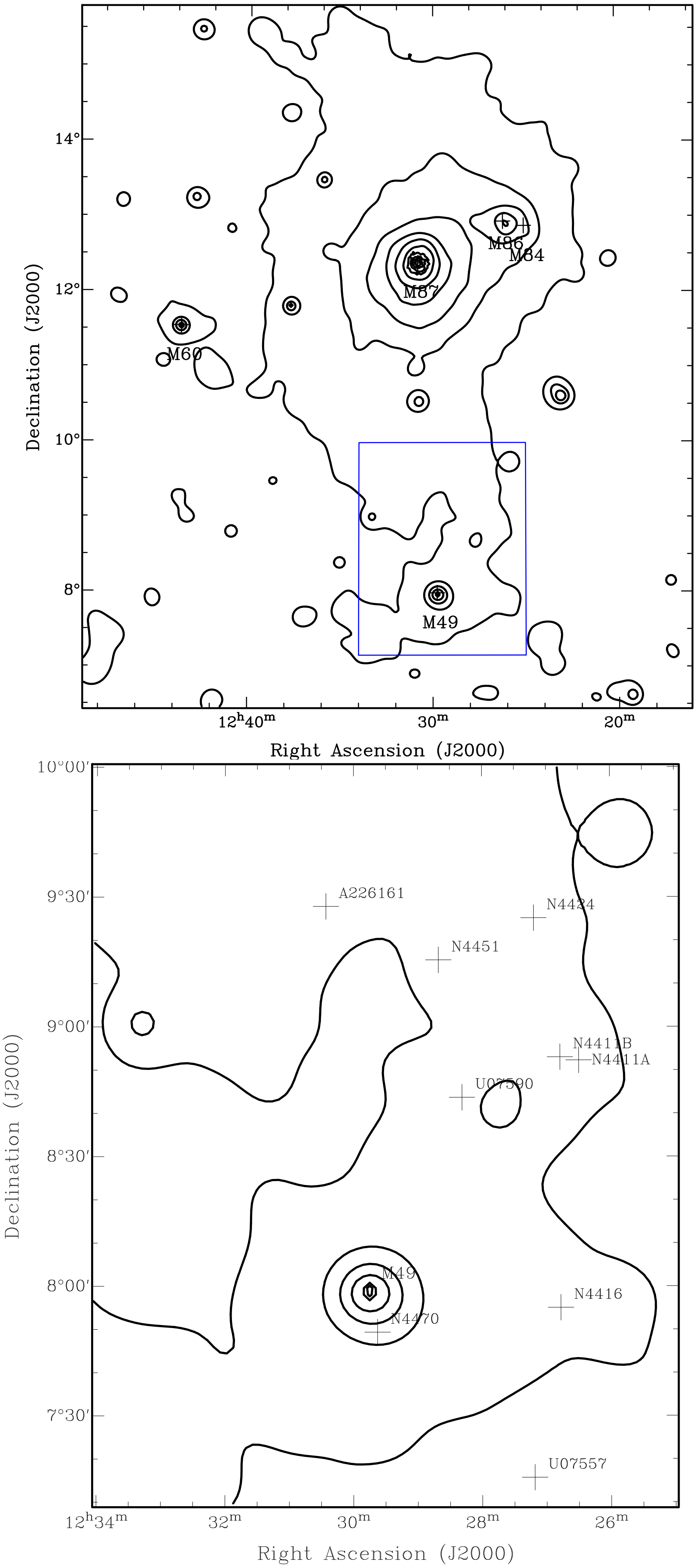

Figure 2.4: An overview of the Virgo Cluster *(top)* and the observed region *(bottom)*. The contours show the X-ray emitting gas at $0.5 - 2.0$ keV from *ROSAT* (Böhringer et al. 1994). The blue rectangle marks out the observed region, zoomed in on the lower panel.

latter 4 sessions, because of the solar interferences, are unusable so only 14 sessions are accounted for. All observations were centred at a frequency of 1418 MHz and the correlator mode used, `c16n25M4k`, provided a total bandwidth of 25 MHz, covering the velocity range -2115 to $3179\,\mathrm{km\,s^{-1}}$. The correlator contains 4096 channels, each channel being 6.1 kHz wide or $1.28\,\mathrm{km\,s^{-1}}$.

The observation technique used at the KAT-7 consists in alternating the exposures between the target and a phase calibrator, and a flux calibrator was observed two or three times per session. The phase calibrator was observed every 20 min or so, to constantly keep an eye on the phase variations during the session. The choice of the different calibrators, given in Table 2.2, lies on their angular distance from the target and their quality status as given by the ATCA Calibrator Database[*] and the VLA Calibrator Manual[†]. The calibrator must be as close as possible to the target, and have a good quality rating in the 21cm L-band. And since the two telescopes are in different hemispheres (e.g., the WSRT calibrator 3C 147 is not visible to KAT-7), a same flux calibrator could not be used for the both observations.

We performed a total of three pointings to cover the desired field, uniformly separated and following the direction of the objects NGC4424 – M49 (see Fig. 2.5). The upper pointing was observed for ~ 30 hrs split in 6 sessions, while the two others were given 24 hrs each during a total of 8 sessions. This is because initially, the observations were focused on NGC 4424 and its HI tail. However, to have a complete view of the tail and to probe the whole region between the galaxy and the elliptical M49, the upper pointing was later expanded to a mosaic. But given that the observations were limited by the availability of sources on the sky and the availability of the telescope, the extra two mosaic pointings could not receive as much time as the first.

2.3.3 The WSRT observations

A total of 4 sessions of 12h observation each were conducted in April 2006 with the WSRT. An individual pointing was observed during each session; two calibrators were also observed, 3C 147 and CTD 93. Because the phase of the WSRT system is quite stable, the calibrators were observed only at the beginning and at the end of the individual observations. To be more sensitive to extended features, the *Maxi-Short* configuration (see section 2.2.1) was adopted for the observations, and the centre of the individual pointings were chosen such that the sensitivity is uniform across the field (see Fig. 2.5). The L-band correlator used provides a 20 MHz band split over 1024 channels, i.e, $4.1\,\mathrm{km\,s^{-1}}$ per channel.

2.3.4 Sensitivity

Despite the difference in the observing times with the two telescopes as listed in Table 2.2, and given the difference in the respective beams, the observations allowed us to approach

---

[*] `http://www.narrabri.atnf.csiro.au/calibrators/`

[†] `https://science.nrao.edu/facilities/vla/docs/manuals/cal`

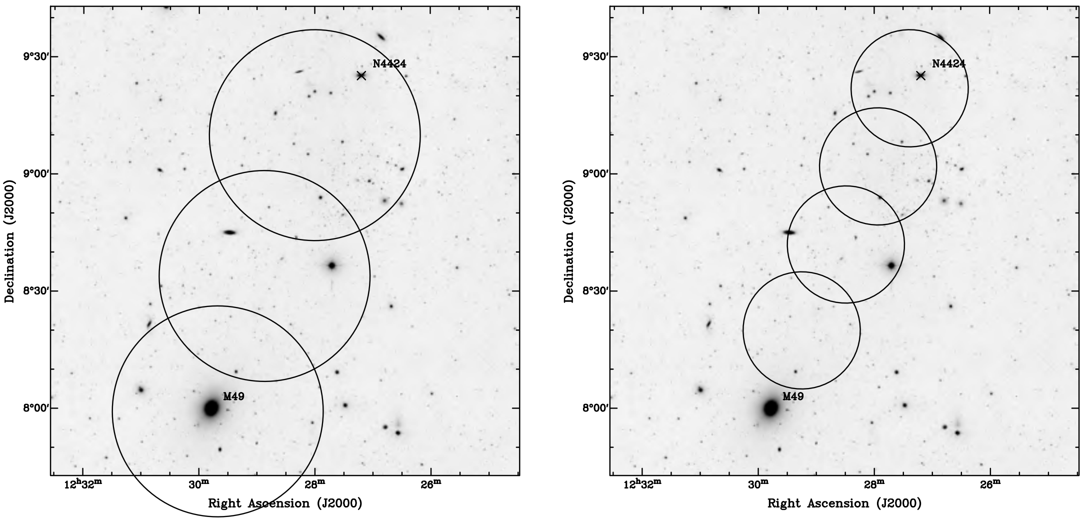

Figure 2.5: KAT-7 (*left*) and WSRT (*right*) primary beams on optical *r*-band grayscale, showing the pointings positions of the observations.

Table 2.2: Summary of the different observations. The pointings of the KAT-7 observations received different observing time due to source and time availability (see text).

Parameter	KAT-7	WSRT
Central frequency	1418.0 MHz	1415.6 MHz
Number of mosaic pointings	3	4
Integration time per pointing	upper: $\sim$ 30h central: 24h lower: 24h	12h
Total integration time	$\sim$ 78h	48h
Velocity range	$\sim$ -2115 – 3179 $\mathrm{km\,s^{-1}}$	$\sim$ -1030 – 2800 $\mathrm{km\,s^{-1}}$
Total bandwidth	25 MHz	20 MHz
Number of channels	4096	1024
Channel bandwidth	6.1 kHz - 1.28 $\mathrm{km\,s^{-1}}$	19.5 kHz - 4.13 $\mathrm{km\,s^{-1}}$
Flux calibrators	PKS 1934-638 & 3C 286	3C 147
Phase calibrator	1254+116	CTD 93

similar column density sensitivities after smoothing the data. This will be discussed in much depth in section 3.4.

Chapter 3

Data reduction

We discuss in this chapter the reduction of the observations described in the previous chapter. The very first step of these reductions is the data flagging. This consists in removing the data affected by radio frequency interference (RFI) discussed in section 2.1.2. We dedicate section 3.1 discussing the flagging process, before describing in section 3.2 the techniques used to calibrate the data.

3.1 RFI flagging

3.1.1 KAT-7 data flagging

As mentioned before, the KAT-7 is still in the commissioning phase and the RFI monitoring is still ongoing. Therefore special care needs to be given to the inspection of the data beforehand. We started by applying an automatic flagging routine to remove data affected by antenna shadowing. These are effects caused by the fact that an antenna being in front of another one in the direction of the source may screen the latter if the altitude of the source is low and the baseline short enough for this to happen. Because the system temperature of the receiver increases for observations at low elevations, we discarded the data of the calibrators below 20° in elevation, and removed two bad channels located outside the desired frequency range. We then proceeded to further visual examination of the data along the frequency and baseline axes, during which we performed manual flagging. Several tests were performed during the manual flagging to ensure the minimisation of the artifacts and baseline-based interferences. The most recurrent RFI was certainly a system-generated narrow RFI, that affected all baselines with a constant amplitude. It occurred at 1408 MHz and spanned two channels, i.e, 12.2 kHz or $2.56\,\mathrm{km\,s^{-1}}$. Luckily, besides being very narrow, this was outside the spectral region of interest and was easily removed. Another noticeable RFI was, this time, broader and baseline-based (probably system-generated). It occurred on short baselines such as ANT3-ANT4 and ANT4-ANT5. It mostly affected the beginning and end of the observations, although the elevations were high enough ($> 20°$). Also, the Galactic

HI was – as one would expect – constantly present in the data and although we did not flag it, special care was taken to suppress its effects on the sources of interest (see section 3.2.1).

3.1.2 WSRT data flagging

The WSRT data was quite stable over time, and not much flagging were done. Only an automatic flagging was performed to remove data affected by antenna shadowing.

3.2 Calibration

In this section we briefly describe the main steps adopted to reduce the datasets from both telescopes. Different packages (namely CASA and MIRIAD) were used in this work to reduce the data from the two arrays. This is because data reduction pipelines were previously developed for the two telescopes based on these packages. We will not go into much detail regarding the procedures, since extensive materials exist online regarding data reduction with CASA* and MIRIAD†.

3.2.1 KAT-7 data

The entire reduction process of the KAT-7 data was done using the CASA software (Common Astronomy Software Applications) version 4.1.0. The different steps described in this section are, unless stated otherwise, applied to single observations.

As mentioned in section 2.3.2, three VLA calibrators were observed during the sessions. These are PKS 1934-638 and 3C286 (a single source was observed at a time, depending on the availability) for the bandpass calibration, and 1254+116 for the phase calibration. The former two are generally used as flux calibrators and for this reason, a model is available for each of them in CASA along with their standard fluxes. The standard flux values used in the present work are those of Perley & Butler (2013). CASA task `SETJY` allows to specify this.

After the flagging process, we first set up the values of the keywords `MEAS_FREQ_REF` and `REF_FREQUENCY` in the `SPECTRAL_WINDOWS` of the data sets tables to ensure a proper velocity coordinates along the frequency axis. This is because KAT-7 does not use Doppler tracking and CASA does not fully recognise frequency keywords. Next the datasets were individually averaged over 4 channels ($\sim 5.1\,\mathrm{km\,s^{-1}}$) and $20s$ in time to increase the signal-to-noise ratio. We furthermore removed the channels at the edges of the spectral axes of the data, where the amplitude falls off due to low sensitivity (∼ 150 channels each side). This helps minimise the bad data flagging rate when applying the calibrations.

The preliminary steps executed were the initial phase calibrations. Because the observations were done on a broad range of time, the sources were observed at quite different elevations. This could induce variations on the gain of the bandpass calibrator from a scan

---

[*] http://casa.nrao.edu/

[†] http://www.atnf.csiro.au/computing/software/miriad/

to another. Since one wants to prevent as much as possible the biases when computing the bandpass solutions (described below), it becomes necessary to initially calibrate the phase. In other words, we reduce as much as possible the phase variations with time. This was done with the task `GAINCAL` with the *phase only* calibration mode (`calmode = 'p'`).

Next, a bandpass solution was determined by either solving for a complex gain in each channel, or by fitting the bandpass with a fifth order polynomial as a function of frequency channels. These solution types are known as `B` and `BPOLY` modes and are handled with the parameter `bandtype`. They are only function of frequency – not time – with the approximation that they are constant or slowly varying. In determining the solutions, we excluded the region of the spectrum dominated by the Galactic HI emission. The `BPOLY` type were applied only in those cases where the `B` mode had failed, mostly due to a large fraction of the data being previously flagged.

Having determined the bandpass solutions, we then calibrated the antenna-based gains as a function of time. This consists of using the previously determined solutions to derive corrections for the complex antenna gains as a function of time, for both targets and calibrators. `GAINCAL` was once again used to perform this, this time using the *amplitude and phase* calibration mode (`calmode = 'ap'`). These solutions, along with the "bandpass" solutions, are written in separated tables which will later be applied to the targets visibilities.

The last step before applying the calibrations to the targets of interest is to determine the "true" flux density of the phase calibrator. In other words, we scale the flux of the phase calibrator using the flux calibrator as reference, since the latter's flux is catalogued and has been previously set using `SETJY`. To this end we used the task `FLUXSCALE`, which writes a new table containing the actual flux values. This table, along with the ones containing the solutions previously determined, are then applied to the targets using the task `APPLYCAL`.

After applying the different calibration tables, the targets were `SPLIT` from the calibration sources. To those individual targets, a continuum subtraction was performed to get rid of the continuum sources in the field. Two strong continuum sources were present in the region: M49 which lies in the bottom pointing and M87 located $\sim 3^\circ$ north the centre of the field. The continuum subtraction was done using the task `UVCONTSUB`, and a linear continuum model was fitted on the line-free frequency channels.

To avoid any ambiguity in the spectral coordinates in the output images, we set the output frame to optical, barycentric frame using the task `CVEL`.

At this step, the individual datasets were completely calibrated and were just waiting to be put together. We combined them into a single measurement set using `CONCAT`. And once again, a spectral smoothing was performed from a channel width of $\sim 5.1\,\mathrm{km\,s^{-1}}$ to $\sim 15.2\,\mathrm{km\,s^{-1}}$. It is the latter measurement set that will later be imaged (section 3.3.2).

3.2.2 WSRT data

A preliminary step was taken, after importing the WSRT data to MIRIAD, to perform an initial system temperature (T_{sys}) correction manually to the data, and set the reference frequency (`restfreq` keyword) with the `PUTHD` task.

The overall calibration scheme adopted for the WSRT data was somewhat different from the one used for the KAT-7 data with the major difference lying in the way the phase was calibrated. In the following we will only focus on this phase calibration.

Unlike the KAT-7 data reduction, the WSRT data reduction made use of a single calibration source. This is because the target fields were used to calibrate themselves, through a *self-calibration* process. After applying the bandpass and gain calibrations (like previously done for the KAT-7 data) to the data, a polynomial was fitted and extracted from it. This continuum visibility set was then imaged using the `INVERT` task and iteratively deconvolved (CLEANed, see below) until the output continuum map was satisfactory. Then the continuum data was self-calibrated – with the `SELFCAL` task – using the CLEAN continuum map as model. Then the gain solutions were copied and applied to the bandpass- and gain-calibrated line data. A second order polynomial was finally fitted to the continuum and subtracted from the line data.

As a last step, the bandpass edges were cut off the line data ($\sim 10\%$ on each side) and a spectral Hanning smoothing was applied over every 4 channels , i.e, from a $4.12\,\mathrm{km\,s^{-1}}$ to a $16.49\,\mathrm{km\,s^{-1}}$ resolution.

3.3 From UV data to image cube

Once the calibration appeared successful, the calibrated measurement sets were converted into images. Though the principle is the same for the two datasets, the methods used to achieve this are somewhat different since one is using two different packages. Before we discuss separately the methods adopted to image the two calibrated datasets, it is necessary to describe the theory of the image reconstruction principle.

3.3.1 The theory

This is generally a three-step process (see Cornwell 1995):

- A *dirty* image construction. This consists of applying a Fourier transform (FT, hereafter) to the measurement sets, to convert the data from the visibility (u,v) plane to the image (x,y) plane. If V and I are respectively the visibility and the sky brightness, then the functions $V(u,v)$ and $I(x,y)$ form a Fourier pair; that is, one can convert from one to the other. Practically, the visibility observed is not the true visibility but instead a noisy and sampled visibility $S(u,v)V(u,v)$, where $S(u,v)$ is the sampling function. The FT of this sampled visibility therefore provides a *dirty* image I^D written

  $$I^D(x,y) = \mathcal{F}^{-1}\left(S(u,v)V(u,v)\right) \tag{3.1}$$

  This *dirty* image may also be seen as the convolution of the true image I with the synthesised *dirty* beam B:

  $$I^D(x,y) = B(x,y) * I(x,y) \tag{3.2}$$

The *dirty beam* B, also called point spread function (PSF), is the FT of the sampling function, i.e, $B(x, y) = \mathcal{F}^{-1}(S(u, v))$. It is the response of the interferometer to a point-like source.

The shape of the *dirty* image depends on the *dirty beam* which in turn, is function of the sampling function S; moreover, the sampling function is related to the weight w

$$S(u, v) = \sum_k w_k \, \delta(u - u_k) \, \delta(v - v_k) \tag{3.3}$$

where δ is the Dirac delta function. Therefore, the characteristics of the dirty image depend on the weighting mode given to the sampling, i.e., the weights by which each visibility is multiplied before gridding. Several weighting modes exist to date, with the most popular being the *natural*, the *uniform* and the *robust* modes (Sramek & Schwab 1989, Briggs 1995). The *natural* weighting scheme minimises the noise in the *dirty* image by affecting a higher weight to the shorter baselines to the detriment of the longer ones. While this offers an optimum signal-to-noise, a drawback of this weighting mode is the resulting strong sidelobes around the bright sources and a lower spatial resolution. On the other hand, the *uniform* weighting mode – which gives the same weight to every baseline – reduces the sidelobe level and gives a better resolution to the image, but also gives a higher noise level. As for the *robust* weighting scheme, this is an intermediate mode that offers an adjustable parameter – the robustness R – that varies between -2.0 (close to *uniform* weighting) and 2.0 (close to *natural* weighting). This latter mode is known in CASA as the `Briggs` mode, and R is the `robust` parameter.

- The deconvolution. This second step serves to correct for the sampling effects in the image plane. The most widely used deconvolution algorithm in radio interferometry, which is also used in the present work, is the CLEAN algorithm (Högbom 1974). To minimise the computation time, the algorithm approximates the sky brightness distribution to a finite number of point sources and that the surrounding region of the sky is "empty"; it then finds the position and the intensity of the peak in the dirty image $I^D(x, y)$ and shifts the *dirty beam* on it. Next it subtracts from it a fraction of the dirty beam $B(x, y)$, and iteratively repeats the process by selecting fainter peaks until either the desired noise level or the maximum number of iteration is reached. However in practice, since one wants to limit the computation time and seeks for a convergent solution (i.e., we want the iterations to stop *only* when the desired noise is reached), it is more suitable to manually select the bright sources to be CLEANed. This is detailed below. Another case in which this is useful is when the source has a complex morphology and the sidelobes are strong in the dirty image.

  At the end, the CLEANed sources are convolved with a Gaussian approximation of the central peak in the dirty beam (*not* the dirty beam) and added to the residual noise image to form the CLEAN map.

- The last step of the process is the *self-calibration*. Because the visibility measurements obtained are subject to atmospheric and instrumental errors which may cause phase fluctuations, this last step may be needed to correct for these, especially for long baseline arrays where fluctuations in phase are more significant. It consists in finding, from the data, a model of the source being observed. This model is then used to calibrate the actual data on the source.

3.3.2 KAT-7 data synthesis imaging

The imaging and deconvolution of the measurement set in CASA was achieved with a single task: `CLEAN`. The phase centre was set to the centre of the field, i.e at J2000 coordinates ($12^{\mathrm{h}}\,28^{\mathrm{m}}\,30.5^{\mathrm{s}}$, $+08^\circ\,43'\,00''$) in a mosaic mode. Once again, the reference frequency (corresponding to the HI line rest frequency) was set to ensure proper spectral coordinates. The *robust* weighting scheme was used to construct the dirty image, with a robustness $R = 0$. This allows us to achieve a good compromise between resolution and sensitivity, and produces moderate sidelobes. In search for low surface brightness extended structures, the appropriate weighting scheme to adopt would be the natural weighting. However, this produced a low resolution image dominated by sidelobes. Furthermore, to obtain a good representation of the *u,v* plane, the cell size (or pixel size) was chosen to be $55''$, i.e, approximately the third of the beam width along the minor axis of the beam. This resulted in a dirty image made of 256 pixels per spatial axis and 250 channels.

After visual inspection of the dirty cube, the CLEAN algorithm was then used to interactively deconvolve the dirty image. This was done using a mask to select (by hand) regions of HI emission throughout the frequency axis. After each major cycle, since the sidelobes become fainter after each iteration, fainter emissions appear in the image and the mask was further expanded to cover those emission regions. After this process a final mask was created and saved, which was later used to reproduce the CLEAN image cube in a non-interactive mode.

KAT-7 image cube

The CLEAN image is a mosaic of three different pointings covering a sky region of $\sim 1.8^\circ$ wide in Right ascension and $\sim 2.6^\circ$ in Declination. In velocity, it covers a range of -1465 to $2350\,\mathrm{km\,s^{-1}}$ at a resolution of $15\,\mathrm{km\,s^{-1}}$. Since the individual pointings had different observing time (see 2.3.2) hence different sensitivity, the final sensitivity of the cube is a combination of the different weighted signal-to-noise ratios. This is $\sim 2.5\,\mathrm{mJy\,beam^{-1}}$, which, as expected, is slightly higher than the theoretical noise of $\sim 2.1\,\mathrm{mJy\,beam^{-1}}$ (see Fig. 2.2). Table 3.1 summarises the parameters of the KAT-7 image cube.

3.3.3 WSRT data synthesis imaging

The image formation from the WSRT visibility data was done with the `INVERT` task in MIRIAD. This performs a FT of the data from the visibility plane to the image plane, as described in section 3.3.1. A cell size of 5″ was chosen, and a dirty image cube was produced in a mosaic mode. Here again, the weighting mode adopted was the *robust* mode, with a robustness $R = 0.5$. The WSRT synthesised beam is elongated in the North-South direction because of the East-West orientation of the array. This affects the output image, especially the compact sources which tend also to be elongated in the same direction. We reduced this effect by applying a symmetric Gaussian taper of FWHM = 30″ (or $\sim 3\,\mathrm{k}\lambda$ in the *u,v* plane) to the visibility data. This improves the SNR of the data, at the expense of the resolution.

In the Fourier Transform process, `INVERT` produces, along with the dirty image cube, a (synthesised) beam map. But unlike the `CLEAN` task in CASA which produces a beam dataset for each plane of a cube, `INVERT` produces a single beam map for all the planes. In doing so, the task requires all the planes in a given visibility to be unflagged which, for the present data, is too restrictive. A large fraction of the data were therefore rejected when imaging. To correct for this, we set a tolerance of 10% using the `slop` parameter. That is, for a visibility to be rejected, the fraction of bad channels in it must be > 10%. In cases where the fraction is non-zero and less than one, then a linear interpolation was performed to replace the flagged channels. To achieve this, the parameter was set to `slop = 0.1,interpolate`. This method brought the fraction of rejected visibilities to a negligible value.

Next, the MIRIAD task `CLEAN` was used to deconvolve the dirty cube. But since the task does not offer an interactive CLEANing mode, `CGCURS` was beforehand used to write a mask file by manually selecting regions of HI emission along the planes. This mask file, along with the dirty map and dirty beam produced earlier, were the input to the `CLEAN` task. The iterations were constrained by the noise level (i.e the maximum number of iterations were set very high), and we ensured that there was a converging solution on each CLEANed plane. As output, we had a map containing the CLEAN components that was later added to the residual using the task `RESTOR`.

WSRT image cube

The resulting data cube covers the region ($12^{\mathrm{h}}\,32^{\mathrm{m}}\,00^{\mathrm{s}}$, $+07^\circ\,32'\,00''$) to ($12^{\mathrm{h}}\,24^{\mathrm{m}}\,45^{\mathrm{s}}$, $+09^\circ\,55'\,00''$), that is, 1.8° in R.A and 2.3° in Dec. The total area covered is a little smaller than that covered in the KAT-7 data, and its rms noise is $\sim 0.35\,\mathrm{mJy\,beam^{-1}}$. The cube contains 1232 × 1642 pixels per channel, with each pixel being 5″ × 5″ and the channel width is $16.5\,\mathrm{km\,s^{-1}}$. The restoring beam of the cube is 0.6′ × 2.9′ (see Table 3.1 for a summary).

3.4 Combining KAT-7 and WSRT data

While the rms noise in the KAT-7 data is $\sim 2.5\,\mathrm{mJy\,beam^{-1}}$, that in the WSRT is much smaller, $\sim 0.35\,\mathrm{mJy\,beam^{-1}}$. Since the weight applied to the datasets during combination goes as $1/\sigma_{\mathrm{rms}}^2$, the WSRT data ends up having a much larger weight relative to the KAT-7 data. In fact, if I_K, w_K are respectively the intensity and weight of a given pixel in the KAT-7 data and I_W, w_W those of the corresponding pixel in the WSRT data, the intensity

Table 3.1: Summary of the KAT-7 and WSRT image cubes.

Parameter	KAT-7	WSRT
Weighting function	Robust = 0	Robust = 0.5
Channel width	$15.2\,\mathrm{km\,s^{-1}}$	$16.5\,\mathrm{km\,s^{-1}}$
FWHM of synthesized beam	$4.4' \times 3.1'$	$2.9' \times 0.6'$
Position Angle of synthesized beam	$\sim -8°$	$\sim 1°$
Map gridding	$55'' \times 55''$	$5'' \times 5''$
Map size	256×256	1232×1642
RMS noise	$2.5\,\mathrm{mJy\,beam^{-1}}$	$0.35\,\mathrm{mJy\,beam^{-1}}$

the corresponding pixel in the resulting combined data is

$$I_c = \frac{I_K\, w_K + I_W\, w_W}{w_K + w_W}. \tag{3.4}$$

So, for $w \propto 1/\sigma^2_{\mathrm{rms}}$, $w_K \ll w_W$ and $I_c \sim I_W$.

Therefore, the traditional combination in the u, v plane using the MIRIAD task INVERT results in a largely WSRT feature-dominated data, with the KAT-7 features being essentially nonexistent. To avoid this, we performed the combination in the image plane. In this section we describe the procedure we adopted to combine the KAT-7 and WSRT data, to obtain greater detail of the tail seen in NGC 4424.

Although the two datasets have different noise sensitivities, their u, v coverages are also different (see Fig. 3.2). The ratio between the rms noises is more or less equal to the ratio between the respective synthesised beam areas.

Also, the column density of a source is given by

$$\left(\frac{N_{\mathrm{HI}}}{\mathrm{atoms\,cm^{-2}}}\right) = 1.1 \times 10^{21} \left(\frac{b_{\mathrm{min}}\, b_{\mathrm{maj}}}{\mathrm{arcsec^2}}\right)^{-1} \left(\frac{I^{i,j}_{\mathrm{HI}}}{\mathrm{mJy\,beam^{-1}\,km\,s^{-1}}}\right) \tag{3.5}$$

where b_{min} and b_{maj} are respectively the minor and major FWHM of the synthesised (or *dirty*) beam, and $I^{i,j}_{\mathrm{HI}}$ the HI intensity of a pixel of coordinates (*i,j*). It is clear that the column density is proportional to the flux and inversely proportional to the beam area. Therefore, the two datasets end up having the same order of column density sensitivity (see section 4.1.1). The most convenient way of combining them is by first converting the cubes into the units of column density per unit velocity. The whole process was done in MIRIAD.

The continuum-subtracted and non-regridded KAT-7 data of section 3.2.1 (data before applying the `CVEL` task) was first exported from CASA to MIRIAD in UVFITS format. The regridding from topocentric to barycentric frame of the velocity axis using the CASA task `CVEL` causes a variation in the channel width, producing a problem when exporting the data with `EXPORTUVFITS`.

Once imported into MIRIAD, the velocity axis of the KAT-7 u, v data was modified to match that of the WSRT data in velocity range and width. An image was then produced in mosaic mode with a cell size of $5''$, same size as in the WSRT cube. The spatial centre of the mosaic was set to be that of the WSRT cube, and a gaussian taper of $30''$ was also

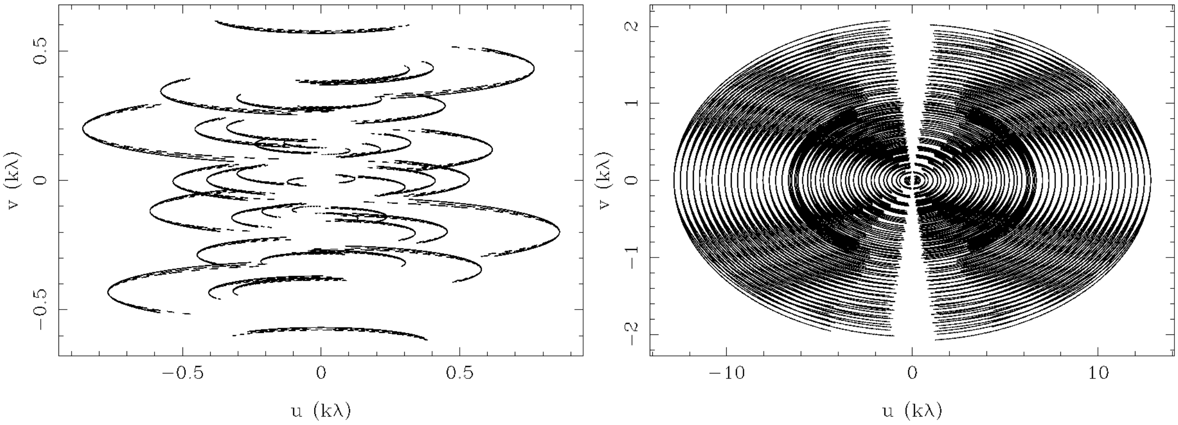

Figure 3.1: KAT-7 (*left*) and WSRT (*right*) *uv* coverage. Notice the narrowness of the range of values along the *v* axis on the KAT-7 panel.

applied. The resulting cube was then CLEANed using the `MOSSDI` task and the dirty beam produced during the image formation, as described in section 3.3.3. Nonetheless, the new KAT-7 cube is spatially larger than that of the WSRT; we then used `REGRID` to regrid the spatial axes of the WSRT cube to the KAT-7 new cube.

At this stage, both image cubes have the same dimensions, coordinate grids, reference pixel and pixel size. This way, any pixel in one cube has the same world coordinates as its corresponding pixel in the other cube. Equation 3.5 was then used, with the `MATHS` task, to convert them into column density cubes. Since the cubes had initially units of flux and Eq. 3.5 uses integrated flux, the output cubes have in reality units of column density per unit velocity that is, units of atoms $\mathrm{cm^{-2}\,(km\,s^{-1})^{-1}}$. The rms noise levels are 5.6×10^{16} and 6.3×10^{16} atoms $\mathrm{cm^{-2}\,(km\,s^{-1})^{-1}}$ respectively in the output KAT-7 and WSRT data cubes, that is, a weight ratio of the variances of 1.26.

Finally, the `MATHS` task was once again used to linearly combine the two data cubes, with the expression

$$I_c = \frac{1.26\,I_K + I_W}{2} \tag{3.6}$$

The rms noise in this final cube is 4.8×10^{16} atoms $\mathrm{cm^{-2}\,(km\,s^{-1})^{-1}}$.

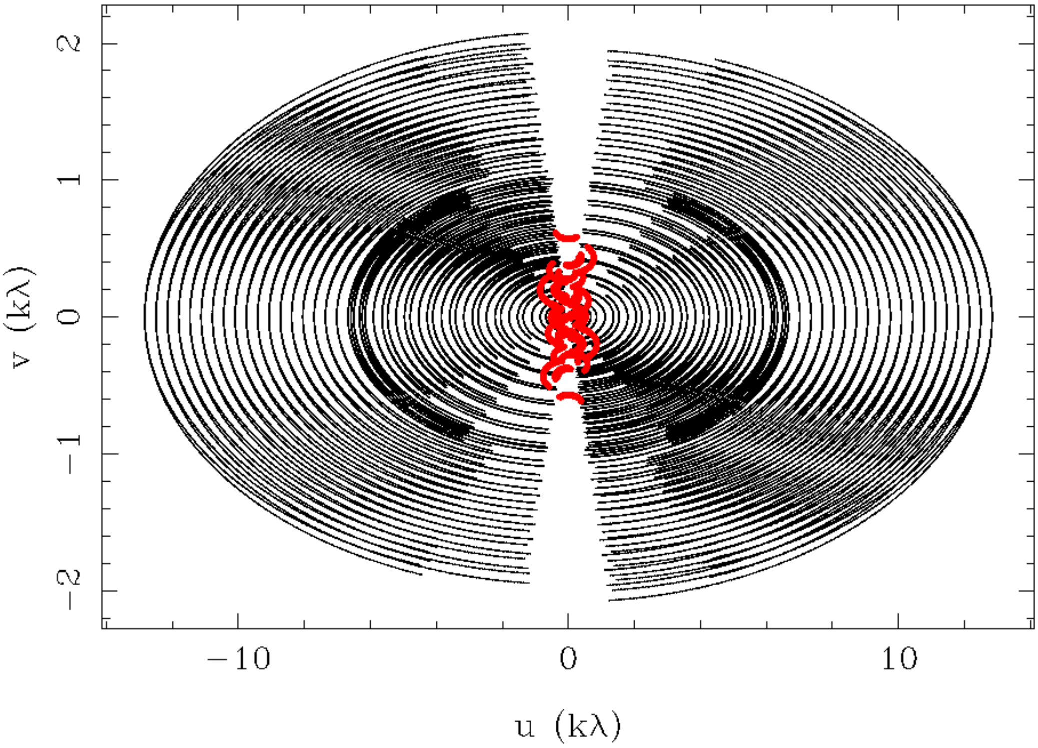

Figure 3.2: An overplot of the *uv* coverage of the two datasets. The *black* lines are the WSRT coverage and the *red* are the KAT-7's.

Chapter 4

Results

The reduction of the H I data allowed the detection of galaxies in the field. In Table 4.1 we present a list of these detections, together with their signal-to-noise ratio (SNR) defined as SNR $= f_{\mathrm{peak}}/\sigma_{\mathrm{rms}}$. f_{peak} is the peak signal of the source and σ_{rms} the rms noise in the image cube containing the source. In this chapter we present the reduced data as well as the methods used to obtain the H I properties of the detections.

Table 4.1: List of detected objects.
(1) Object name.
(2) J2000 coordinates.
(3) Morphological type from LEDA.
(4) Signal-to-noise ratio.

Object (1)	R.A	Dec. (2)	Type (3)	SNR (4)
NGC 4424	12 27 11.6	09 25 14	SBa	4.2
NGC 4451	12 28 40.5	09 15 31	Sab	3.1
NGC 4470	12 29 37.8	07 49 27	Sa	6.2
UGC 7590	12 28 18.8	08 43 46	Sbc	5.7
Cloud 7c	12 30 25.8	09 28 01	H I cloud	3.1
NGC 4411A	12 26 30.0	08 52 18	Sc	11.7
NGC 4411B	12 26 47.2	08 53 04	Sc	19.9
UGC 7557	12 27 11.1	07 15 47	Sm	5.9
NGC 4416	12 26 46.7	07 55 08	Sc	1.4

The locations of these detections with respect to the Virgo cluster are given in Figure 4.1.

4.1 Moment maps

From the `CLEAN`ed cubes previously obtained, we generated the zeroth and first moment maps using the MIRIAD task `MOMENT`. These correspond to the total integrated H I maps and velocity fields, respectively.

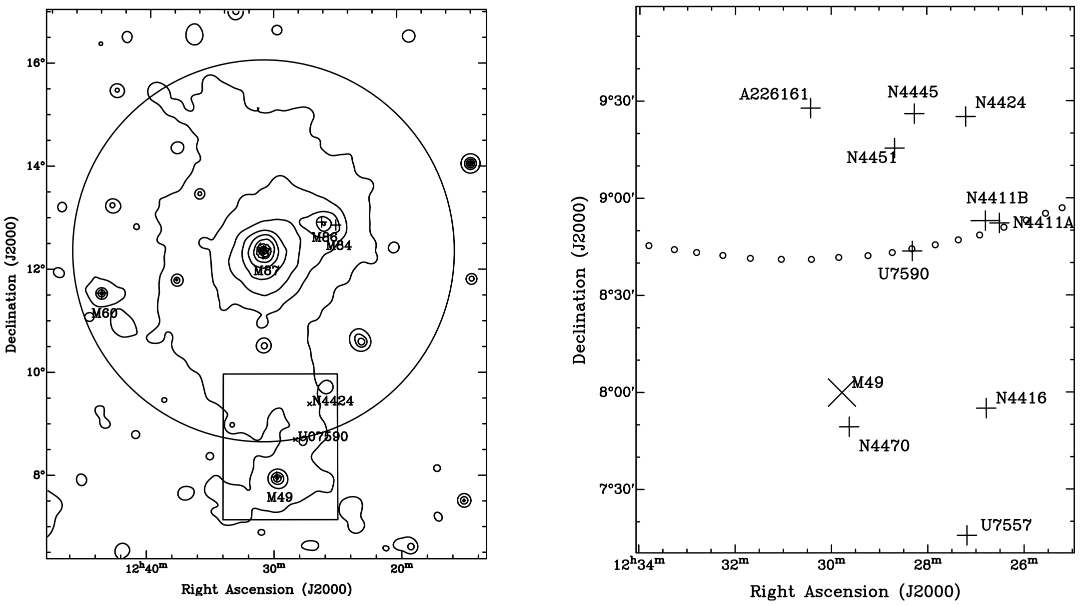

Figure 4.1: *Left:* X-ray map of the Virgo Cluster (0.5 – 2.0 keV, *ROSAT*; Böhringer et al. 1994). The circle shows the virial radius of the cluster ($\sim 3.7°$) around M87, and the box is the region observed in the present work. *Right:* A zoomed-in in the observed region to show the locations of the detections. The circled dots delimit the virial radius of the cluster.

4.1.1 Total integrated map

The total integrated map was obtained by integrating the intensity in the column-density-converted data cubes over spatial and spectral regions containing H I emission:

$$I_{\rm HI}^{i,j} = \sum_{k}^{n} S_k(i,j) \times \Delta v_k \qquad (4.1)$$

with k being the k-th channel and n the total number of channels over which the integration is done; $S_k(i,j)$ and Δv_k are respectively the intensity of the pixel (i,j) on channel k in atoms $\mathrm{cm}^{-2}\,(\mathrm{km\,s}^{-1})^{-1}$, and the velocity gap between channels k and $k+1$ in atoms cm^{-2}. The integrated intensity map has units of atoms cm^{-2}.

More practically, we started by manually drawing plane-by-plane regions to enclose the emission features in a smoothed version of the datacube. The regions were drawn using a 3σ confidence level. Pixels outside these defined regions were blanked, to isolate the emission from noise. Channels of the original cube in which regions were defined (i.e, those containing emission) were then added together to build up the integrated maps.

These integrated maps were then corrected for the primary beam effect. In fact, during observations, the sensitivity is highest at the centres of the pointings. Since the primary beam of the telescopes are gaussian-shaped, the sensitivity falls off when moving to the peripheries of the beam. Thus, at the edge of the beam, only 50% of the true signal is observed. Since we need a uniformity in the sensitivity distribution across the map, we need to correct for this effect. This is done using the MIRIAD task `LINMOS`. We end up with a non-uniform noise level across the maps, with highest values in the outer parts, but it allows us to measure the correct HI flux of the objects across the entire mosaic.

Over $16.5\,\mathrm{km\,s^{-1}}$, the reached column density sensitivities in the maps are 9.2×10^{17}, 1.0×10^{18} and $7.9 \times 10^{17}\,\mathrm{atoms\,cm^{-2}}$, respectively for the KAT-7, WSRT and combined data. The column density maps of the different detections are presented in the appendix.

4.1.2 Velocity fields

The velocity field (or intensity-weighted velocity) map contains the velocity distribution in the image cube. It is obtained (still in MIRIAD) by

$$\langle v^{i,j} \rangle = \frac{\sum_k^n S_k(i,j) \times v_k}{\sum_k^n S_k(i,j)} \tag{4.2}$$

where v_k is the velocity in channel k.

Using the same `CLEAN`ed image cubes and the regions of section 4.1.1, we computed the first moment maps for the different datasets.

Because of the limited resolution in the maps, the velocity dispersion fields (moment 2 maps) were not computed. An example of integrated map and velocity fields of NGC 4424 for the higher resolution (WSRT) image cubes are given in Fig. 4.2. The data cubes used to produce the maps were obtained with a cell size of $10 \times 10''$ (instead of $5 \times 5''$ as listed in Table 3.1) to reduce the scatter in the first moment map. This was done by producing new cubes from the same data, but setting now the cell size to $10''$.

4.1.3 The combined KAT-7 + WSRT data

As mentioned in section 3.4, the main goal of combining the two observations is to achieve a better sensitivity that will allow us to detect the fainter structures. In the case of the galaxy NGC 4424, we seek to map the full extent of the HI tail.

To show the improvement of the data after combination, we show in Fig. 4.3 a comparison of the HI map of NGC 4424 as obtained in the three different datasets. While the tail is seen in the KAT-7 data, its lower end is not detected in the WSRT data. When combined, the data reveal the structure of the tail with a better sensitivity. Compared to the map from the WSRT data in Fig. 4.2, the last panel of Fig. 4.3 shows a tail that is much better seen in the combined data. Assuming a distance of 15.2 Mpc to the galaxy (Cortés et al. 2008), the tail extends out to ∼ 60 kpc from the main envelope. In previous VLA observations of the galaxy by Chung et al. (2007) down to $\sim 2 \times 10^{19}\,\mathrm{atoms\,cm^{-2}}$, only ∼ 20 kpc of tail was seen. The present observations then reveal an HI tail three times longer than previously observed.

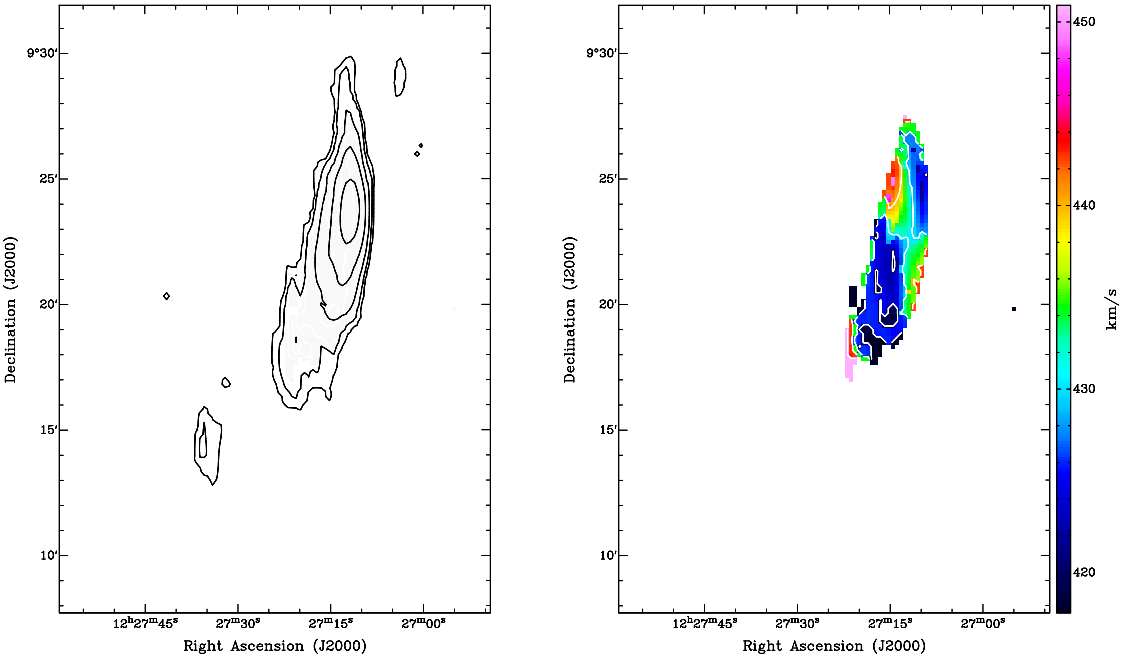

Figure 4.2: Intensity map *(left)* and velocity field *(right)* of NGC 4424 from the WSRT data. The contours of the intensity map are taken at 0.75 (3σ), 1.5, 3.0, 6.0, 12.0×10^{19} atoms cm^{-2}. The white contours of the velocity fields are 413, 423, 433, 443, 453 km s^{-1}.

4.2 HI metrics

In this section we use the obtained HI cubes and maps to derive the HI parameters of the detections listed in Table 4.1.

4.2.1 HI diameter

The size of a galaxy is usually estimated at a surface density of 1 M$_\odot$ pc^{-2}, that is, a column density level of 1.25×10^{20} atoms cm^{-2}. However, our sample of galaxies contains small objects which peak at column densities lower than 1.25×10^{20} atoms cm^{-2}; for instance, the column density of NGC 4424 peaks at $\sim 1.2 \times 10^{20}$ atoms cm^{-2}. Therefore, we measured the HI diameter of all objects in the sample at a column density isophote of 2×10^{19} atoms cm^{-2}.

To estimate the size of the galaxies, we fit a two-dimensional Gaussian to the integrated maps of the objects by considering the aforementioned HI column density isophote. This was done using the `IMFIT` task in MIRIAD. These diameters will later be used to determine the mean HI surface density (section 4.2.3).

4.2.2 HI mass

The HI masses of the individual objects detected in the HI maps were computed using the equation

$$\left(\frac{M_{\mathrm{HI}}}{\mathrm{M}_{\odot}}\right) = 2.36 \times 10^{5} \left(\frac{D}{\mathrm{Mpc}}\right)^{2} \left(\frac{I_{\mathrm{HI}}}{\mathrm{Jy\,km\,s^{-1}}}\right) \tag{4.3}$$

where D is the redshift-independent distance to the object in Mpc (see 4.5), and I_{HI} its total integrated flux. In Table 4.2 we list the HI mass of the detections as derived from the observations. The KAT-7 image cube was used to obtain these HI masses, except for the unresolved galaxies NGC 4411 A&B, for which the WSRT cube was used. The uncertainties on the mass, $\sigma_{M_{\mathrm{HI}}}$, was obtained from an error propagation:

$$\sigma_{M_{\mathrm{HI}}} = M_{\mathrm{HI}} \left[\left(\frac{\sigma_{I_{\mathrm{HI}}}}{I_{\mathrm{HI}}}\right)^{2} + \left(2\frac{\sigma_{D}}{D}\right)^{2}\right]^{1/2} \tag{4.4}$$

where the error $\sigma_{I_{\mathrm{HI}}}$ on the integrated flux is obtained from the measurement and the error σ_D on the distance is estimated to be $\sim 10\%$ of the distance.

We also list in the last column of Table 4.2, for comparison, the HI mass of the detections as found in the literature (ALFALFA[*] for most, except for the galaxies UGC 7590 and UGC 7557 where the GOLDMine database[†] was used to retrieve the data). For five (5) out of the nine (9) objects, the derived HI mass is consistent with the literature value. The HI mass of UGC 7590 is larger by a factor of 2, compared to the value listed on the GOLDMine database. For the galaxies NGC 4411A, UGC 7557 and NGC 4470, the HI masses derived in this work are lower, probably suggesting that we are missing some flux in the measurement. However, for the latter galaxy, the GOLDMine database lists an HI mass of $M_{\mathrm{HI}_{\mathrm{N4470}}} = 4.26 \times 10^{8}\,\mathrm{M}_{\odot}$ which is consistent with our derived mass.

4.2.3 Mean HI Surface Density

Another critical parameter in estimating the HI content of a galaxy is the HI surface density Σ_{HI}, or the HI mass per unit area. We calculated the mean HI surface density by

$$\left(\frac{\Sigma_{\mathrm{HI}}}{\mathrm{M}_{\odot}\,\mathrm{pc}^{-2}}\right) = \frac{(M_{\mathrm{HI}}/\mathrm{M}_{\odot})}{\frac{\pi}{4}\,(D_{\mathrm{HI}}/\mathrm{pc})^{2}} \tag{4.5}$$

with M_{HI} being the HI mass enclosed in a diameter D_{HI} as measured in section 4.2.1.

Applying an error propagation on equation 4.5, we obtain the uncertainty on the HI surface density to be

$$\sigma_{\Sigma_{\mathrm{HI}}} = \Sigma_{\mathrm{HI}} \left[\left(\frac{\sigma_{M_{\mathrm{HI}}}}{M_{\mathrm{HI}}}\right)^{2} + \left(\frac{\sigma_{D_{\mathrm{HI}}}}{D_{\mathrm{HI}}}\right)^{2}\right]^{1/2} \tag{4.6}$$

An uncertainty of $\sigma_{D_{\mathrm{HI}}} \sim 10\%$ was considered for the measured HI diameter of the galaxies.

---

[*] Haynes et al. 2011

[†] Gavazzi et al. 2003

The HI surface densities of the detections as well as their uncertainty is listed in Table 4.2

Table 4.2: HI mass and surface density of the detections.

Object	R.A	Dec.	$M_{\rm HI}$	$\sigma_{M_{\rm HI}}$	$\Sigma_{\rm HI}$	$\sigma_{\Sigma_{\rm HI}}$	$M_{\rm HI_{lit}}$
	J2000		10^8M$_\odot$		M$_\odot$ pc^{-2}		10^8M$_\odot$
NGC 4424	12 27 11.6	09 25 14	1.88	0.45	0.49	0.15	2.19$^{\rm a}$
NGC 4451	12 28 40.5	09 15 31	3.98	1.27	0.14	0.05	3.55$^{\rm a}$
NGC 4470	12 29 37.8	07 49 27	3.16	1.07	0.41	0.15	10.00$^{\rm a}$
UGC 7590	12 28 18.8	08 43 46	28.05	8.51	1.93	0.70	16.59$^{\rm b}$
Cloud 7c	12 30 25.8	09 28 01	1.99	0.49	0.71	0.21	1.78$^{\rm a}$
NGC 4411A	12 26 30.0	08 52 18	1.58	0.34	4.05	1.18	10.23$^{\rm a}$
NGC 4411B	12 26 47.2	08 53 04	15.85	1.12	7.95	2.29	13.18$^{\rm a}$
UGC 7557	12 27 11.1	07 15 47	4.12	0.91	0.80	0.24	26.91$^{\rm b}$
NGC 4416	12 26 46.7	07 55 08	3.99	0.34	5.32	1.66	2.69$^{\rm a}$

References are:
a) ALFALFA, Haynes et al. 2011
b) GOLDMine, Gavazzi et al. 2003

4.3 HI line widths and maximum rotation velocities

The HI line width (or velocity width) is defined as the distance (in velocity unit) between two points on opposite edges of the HI profile taken at some intensity level, commonly at 20% or 50% of the peak flux. In the same context, the systemic velocity is nothing but the halfway between the aforementioned points.

We derive, from the CLEANed image cube previously obtained, the velocity width for the individual detected objects. This is done by first extracting the spectrum of the individual objects along the velocity axis, and according to the shape of the profile (either single or double horn), applying one of the two algorithms described below:

4.3.1 Method 1: Gaussian fit for single-horn profiles

Velocity width

This method is the most straightforward and consists in applying a gaussian fit to the profile. We use this method only on single-horn profiles. First the peak flux is identified and the 50% flux level is estimated from it. From the fitted profile we determine the velocities v_l and v_u respectively on the left and right edges of the profile at the 50% level, where the broadening effects are less pronounced. The width W_{50} at 50% flux level is then $W_{50} = v_u - v_l$ and the systemic velocity is given by $v_{sys} = (v_l + v_u)/2$. We afterwards apply a correction δW_{50} to the linewidth for the broadening effects. For this purpose, we followed the descriptions given by Verheijen & Sancisi (2001) and used the equation

$$\delta W_{50} = \sigma_c \sqrt{8 \ln 2} \left[1 - \sqrt{1 - \frac{(R/\sigma_c)^2}{8 \ln 2}} \right] \tag{4.7}$$

where R is the velocity resolution of the image cube and σ_c is the dispersion of the observed (broadened) Gaussian. Because a spectral Hanning smoothing has been applied to the spectra, the observed profile is the convolution of the "real" profile with the smoothing function. Therefore $\sigma_c = \sqrt{\sigma_0^2 + \sigma_R^2}$ is the combination of the dispersion of the "real" profile (σ_0) and that induced by the Hanning smoothing ($\sigma_R = R/\sqrt{8\ln 2}$). The instrumental effect-corrected width, W_i is then written

$$W_{50,i} = W_{50} - \delta W_{50}. \tag{4.8}$$

This resulted in a typical broadening of less than 10% in both the KAT-7 and WSRT data cubes.

The gaussian fit is illustrated in Figure 4.4 for the profile of the galaxy NGC 4424.

4.3.2 Method 2: Polynomial fit

Velocity width

The Gaussian fit to HI lines works best for single-peaked profiles, which are the exception, not the rule for most galaxies. In fact, the majority of galaxies (except face-on and often dwarf galaxies) have a double-peaked profile caused by double side – approaching and receding – rotation, combined with little HI at the systemic velocity due to the large velocity gradient. Because these profiles are poorly described by Gaussian curves, applying the above method may lead to an inaccurate estimation of the velocity width. Instead, we apply to those objects the method described in Haynes et al. (1999) and more discussed in Springob et al. (2005). This widely used method (see e.g. Schneider et al. 1986, Chengalur et al. 1993, Dale et al. 1998) considers the two peaks of the profile individually and therefore, provides a better representation of the velocity width. It consists in fitting a first order polynomial at both rising sides of the profile over a flux value ranging from 15% to 85% of the peak flux f_p minus the rms noise in the cube, $f_p - \mathrm{rms}$. The subtraction of the rms noise from the peak flux is to minimise the dependence of the velocity width on the signal-to-noise ratio (SNR) of the spectrum (Springob et al. 2005). The velocities V_u and V_l are then interpolated on the fitted line at the 50% level of $f_p - \mathrm{rms}$. As in the previous case, one must also correct the observed width W_{50} for instrumental effects (δW_s), cosmological broadening (δW_z) and the effects of turbulent motions (δW_t). For the instrumental corrections, we followed Springob et al. (2005) and used

$$\delta W_s = 2\lambda \Delta v \tag{4.9}$$

where Δv is the resolution of the instrument. The broadening of the width measurement λ is function of both the SNR of the spectrum and Δv, and is given in Springob et al. (2005). Like the authors, we adopted $\delta W_s = 6.5\,\mathrm{km\,s^{-1}}$. An example of the fit for the galaxy UGC 7590 is shown in Figure 4.5.

4.3.3 Maximum rotation velocity

The linewidth is tightly related to the rotation of the galaxy, and in this section we attempt to use it to derive the maximum rotation velocity. The width previously determined has only been corrected for instrumental broadening. In reality, the observed width is also stretched with redshift z, and one has to account for that fact. This effect is often referred to as the cosmological broadening and is corrected for as

$$W_{50,z} = \frac{W_{50,i}}{1+z}. \tag{4.10}$$

Since the galaxies in the Virgo Cluster are local galaxies (very low redshift), this correction is negligible.

The final step before deriving the maximum velocity of the objects from their respective linewidths is to apply a correction accounting for the broadening caused by turbulent and random motions. To this end, we adopt the quadratic equation given by Tully & Fouqué (1985)

$$W_{R,50}^2 = W_{50,z}^2 + W_{t,50}^2 - 2\,W_{50,z}\,W_{t,50}\left[1 - e^{-(W_{50,z}/W_{c,50})^2}\right] - 2\,W_{t,50}^2\,e^{-(W_{50,z}/W_{c,50})^2} \tag{4.11}$$

where $W_{R,50}$ is the turbulent-corrected profile width, $W_{t,50}$ the broadening caused by (random) turbulent motion and the quantity $W_{c,50}$ provides the transition from linear to quadratic summation. The turbulent motion is estimated by:

$$W_{t,50} = 2\,k_{50}\sigma_z \tag{4.12}$$

with σ_z being the dispersion velocity caused by random motions out of the plane of the disk galaxies and k_{50} an adjustable parameter. Though many discussions have been going on about the parameters values ever since (see e.g Verheijen & Sancisi 2001), we will adopt in the present work those provided by Fouqué et al. (1990) who assumed an isotropic distribution of the non-circular motions ($\sigma_x = \sigma_y = \sigma_z$) and adopted $\sigma_z = (12 \pm 4)\,\mathrm{km\,s^{-1}}$ from Lewis (1987). They also adopted $k_{50} = 1.13$, which corresponds to $W_{t,50} \sim 27\,\mathrm{km\,s^{-1}}$ and finally a $W_{c,50}$ typical value of $100\,\mathrm{km\,s^{-1}}$. This reduces Eq. 4.11 to

$$W_{R,50}^2 = W_{50,i}^2 - 27\,W_{50,i}\left[1 - e^{-(0.01\,W_{50,i})^2}\right] - 1458\,e^{-(0.01\,W_{50,i})^2} + 729 \tag{4.13}$$

which is solely function of the value of the instrumental-corrected linewidth $W_{50,i}$. Finally, the maximum rotation velocity is given by

$$v_{\max} = \frac{W_{R,50}}{2\,\sin i} \tag{4.14}$$

where i is the inclination of the galaxy along the line of sight obtained from HYPERLEDA*.

---

*http://leda.univ-lyon1.fr

4.4 Dynamical mass

We next proceeded to derive the dynamical mass of the galaxies. If we approximate the mass distribution of the galaxies to be spherically symmetric, then the total mass of a galaxy enclosed in a radius r is given by the equation

$$\left(\frac{M_{\rm dyn}}{\rm M_\odot}\right) = 2.5 \times 10^5 \left(\frac{v_c}{\rm km\,s^{-1}}\right)^2 \left(\frac{r}{\rm kpc}\right) \tag{4.15}$$

where v_c is the maximum rotation velocity corrected for inclination.

Table 4.3: HI diameter (along the major axis) and dynamical mass of the detected objects, in both the KAT-7 and WSRT data.

Object	$d_{\rm HI}$ ($'$)		$M_{\rm dyn}/{\rm M_\odot}$	
	KAT-7	WSRT	KAT-7	WSRT
NGC 4424	5.1	4.4	9.35	8.98
NGC 4451	7.6	3.2	11.04	10.85
NGC 4470	4.6	–	10.25	–
UGC 7590	4.8	6.5	10.59	10.71
UGC 7557	5.2	–	10.65	–
Cloud 7c	4.1	–	9.50	–
NGC 4411A	–	4.0	–	9.75
NGC 4411B	–	6.0	–	10.53

4.5 Independent Tully-Fisher distances

The Tully-Fisher relation Tully & Fisher (TFr, 1977) empirically relates the rotation velocity of a spiral galaxy to its luminosity. The relation provides one of the most reliable secondary distance indicators, since it is independent of the redshift. The TFr has since been widely used to determine distances to clusters and single galaxies, and different calibrations in different bands have been attempted (e.g Dale et al. 1998, Haynes et al. 1999, Solanes et al. 2002, Masters et al. 2014a). In the present work, we use the near infrared J, H and K_s bands of the Two Micron All Sky Survey (2MASS, Jarrett et al. 2000) and the calibrations of the TFr of Masters et al. (2014b) to determine the independent Tully-Fisher distances of the detected galaxies.

4.5.1 Mid-Infrared photometric data

We obtained the $J\,(1.11 - 1.36\,\mu$m), H$\,(1.50 - 1.80\,\mu$m) and $K_s\,(2.00 - 2.32\,\mu$m) "total" extrapolated photometry and axial ratio of the individual objects from the extended source catalogue (XSC) of 2MASS (Jarrett et al. 2000). The absolute magnitudes were then derived by correcting the observed magnitudes as follows (Masters et al. 2014b):

$$M_{{\rm corr}_X} - 5\,logh = m_{obs} - A_X - I_X + k_X - T_X \tag{4.16}$$

where X represents the different J, H, K_s bands. The corrections for extinction due to the Milky Way A_X and intrinsic to the galaxy itself I_X, and the redshift $k-$correction k_X were applied following Masters et al. (2003). For the Galactic extinction and redshift corrections in the different bands, we took (Schlegel et al. 1998):

$$A_J = 0.902\,E(B-V) \qquad A_H = 0.576\,E(B-V) \qquad A_K = 0.367\,E(B-V) \tag{4.17}$$

$$k_J = -0.68\,z \qquad k_H = -0.40\,z \qquad k_K = -1.52\,z \tag{4.18}$$

where the reddening coefficients $E(B-V)$ are from Schlafly & Finkbeiner (2011). The internal extinction is parameterised therein as

$$I_X = \gamma_X \,\log{(a/b)_X} \tag{4.19}$$

with $(a/b)_X$ being the axial ratio of the galaxy in the X band, and γ_X the extinction law. Different works such as Giovanelli et al. (1994) and Tully et al. (2008) led to different values of γ_X, but in the present work we use the values in Masters et al. (2003) who found a dependency of γ_X on $(a/b)_X$.

We further corrected for the different morphological types to an "Sc" type (term T_X) using the corrections given in Masters et al. (2014b). The morphologies of the galaxies in the present work are taken from HYPERLEDA. These correction terms are function of the HI line width and have the form $T_X = a_{X_T} + b_{X_T}(\log W - 2.5)$ where constants a_{X_T} and b_{X_T} (not to confuse with the axial ratio of the galaxy) depend on the band X and the morphological type T of the galaxy, and are given therein.

4.5.2 Distance moduli

The distance modulus of a galaxy is characterised by the difference between its apparent and absolute magnitudes. In the Mid IR 2MASS bands, the magnitude of a galaxy based on its rotation is given by (Masters et al. 2014b):

$$\begin{aligned} M_{W_J} - 5\,\log h &= -21.370 \pm 0.018 - 10.61 \pm 0.12\,(\log W - 2.5) \\ M_{W_H} - 5\,\log h &= -21.951 \pm 0.017 - 10.65 \pm 0.11\,(\log W - 2.5) \\ M_{W_K} - 5\,\log h &= -22.188 \pm 0.015 - 10.74 \pm 0.10\,(\log W - 2.5) \end{aligned} \tag{4.20}$$

For every object, the distance modulus in band X is then obtained by

$$\mu_X = M_{\mathrm{corr}_X} - M_{W_X} \tag{4.21}$$

where M_{corr_X} is from Eq. 4.16 and M_{W_X} from Eq. 4.20. The distance to the object is finally

$$\frac{D_X}{\mathrm{pc}} = 10^{0.2\mu_X+1} \tag{4.22}$$

The values of μ_X and D_X for the detected objects with IR data are given in Table 4.4. For comparison, we compile in Table 4.5 the distance to the objects as found in the literature. For many of the galaxies, the derived distance is lower than what is found in the literature; for instance, Cortés et al. (2008) reported a distance of 15.2 Mpc for NGC 4424, using the measurements from the stellar kinematics of the galaxy. This underestimation of the TF distance is an indication of a disturbed gas kinematics due to the environment (see also Kenney et al. 2004).

Table 4.4: Maximum rotation and systemic velocities, and distances of the detected objects having optical counterpart.

Object	v_{rot}	v_{sys}			μ			D	
		Helio	3K	J	H	K	J	H	K
	$\mathrm{km\,s^{-1}}$	$\mathrm{km\,s^{-1}}$			mag			Mpc	
NGC 4424	29.3	433	769	21.82	22.63	21.81	0.23	0.33	0.23
NGC 4451	126.9	864	1200	30.90	31.04	31.07	15.13	16.14	16.37
NGC 4470	68.4	2321	2660	26.61	27.19	26.80	2.10	2.74	2.29
UGC 7590	88.6	1113	1450	31.23	31.75	31.44	17.62	22.39	19.41
UGC 7557	122.6	924	1264		—			—	
NGC 4411A	52.6	1271	1609		—			—	
NGC 4411B	76.9	1261	1598	29.99	30.03	29.50	9.95	10.14	7.94
Cloud 7c	37.0	497	832		—			—	

Table 4.5: Literature distances of the detections.

Object name	Distance (Mpc)	References
NGC 4424	15.2	a
NGC 4451	29.3	b
NGC 4470	24.1	c
UGC 7590	30.5	b
UGC 7557	16.8	d
NGC 4411A	15.1	e
NGC 4411B	27.9	e
Cloud 7c	16.8	d

References are:
a) Cortés et al. 2008
b) Springob et al. 2009
c) Theureau et al. 2007
d) Taken to be the distance to M87
e) Solanes et al. 2002

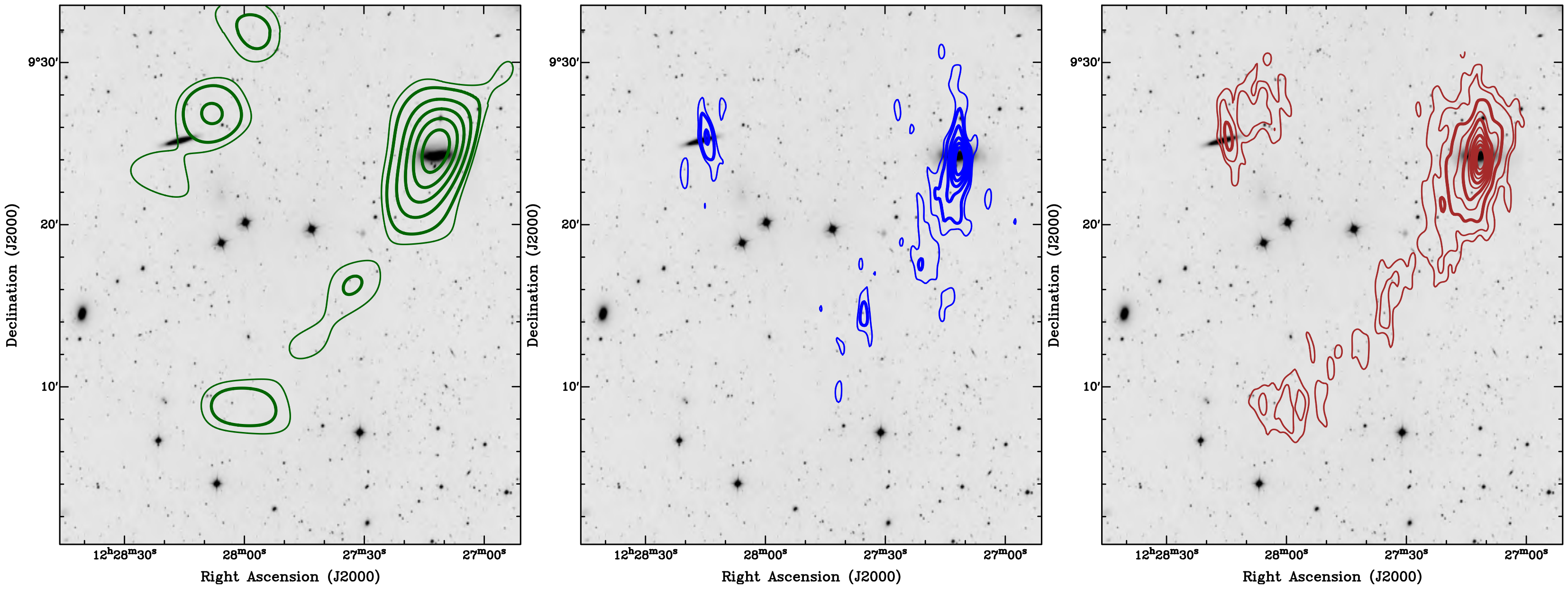

Figure 4.3: NGC 4424 as seen in the KAT-7 (*left*), WSRT (*middle*) and combined (*right*) data, overlaid on SDSS r-band grayscale. The contour levels of the KAT-7 and WSRT maps are respectively 0.7 (3σ), 1.0, 2.0, 3.0, 4.0, 5.0×10^{19} atoms cm^{-2} and 0.75, 1.5, 3.0, 6.0, 12.0, 15.0×10^{19} atoms cm^{-2}, and those of the combined map are 0.5, 1, 2, 3 ... 10 $\times 10^{19}$ atoms cm^{-2}.

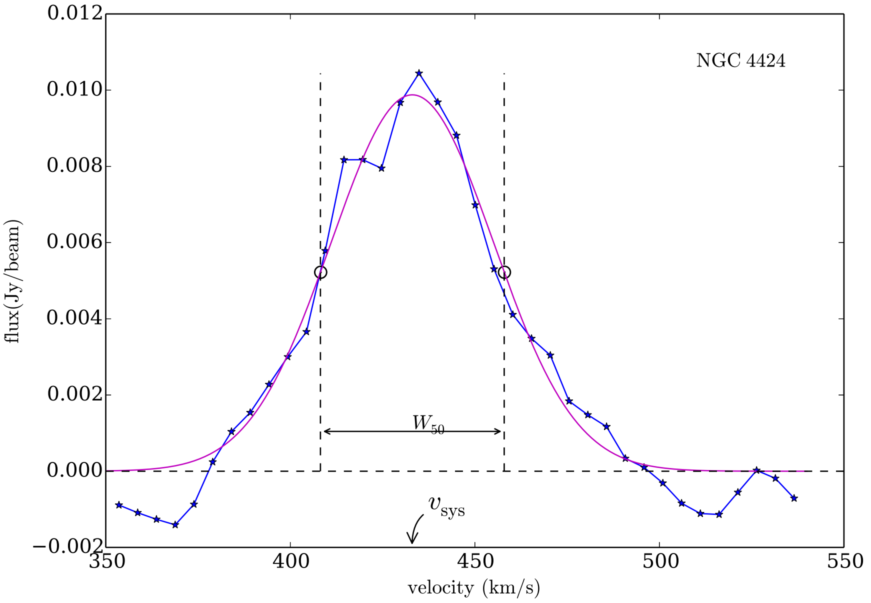

Figure 4.4: The global profile of the spiral NGC 4424 with a Gaussian fit (*magenta line*). The left and right small circles give the positions of v_l and v_u, respectively. The velocity width W_{50} as well as the systemic velocity $v_{\rm sys}$ are shown.

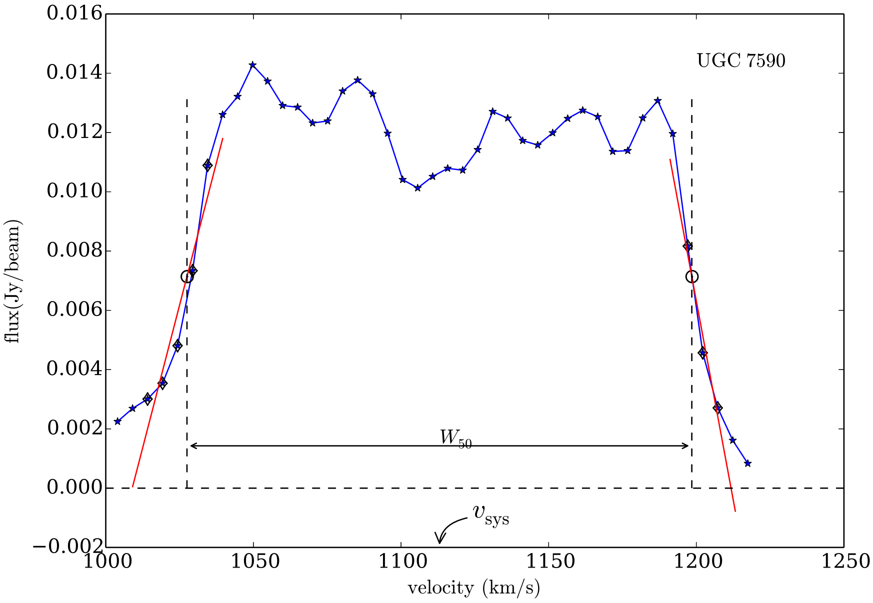

Figure 4.5: Polynomial fit of the velocity width W_{50} and systemic velocity $v_{\rm sys}$ applied to the galaxy UGC 7590. The diamond symbols show the data points used in the fit, and the red lines are the straight lines fitted to the slopes of the profile. The small circles are the same as in Fig. 4.4.

Chapter 5

Analysis

5.1 H I deficiency

A question we seek to investigate in the present work is the influence of the environment on galaxy evolution, through the study of their gas content. It is then necessary, to obtain a broad picture of the processes, to compare the gas content of galaxies of different environments. One reliable parameter used to this end is the H I deficiency. The H I deficiency was first noticed by Davies & Lewis (1973) from the survey of about 25 galaxies in the Virgo Cluster, when the authors compared the gas content of those galaxies to that of a similar sample of nearby field galaxies. By using both the H I mass to luminosity ratio $M_{\text{H I}}/L$ and the H I surface density $\Sigma_{\text{H I}}$, they concluded that the Virgo Cluster spirals were H I poor with respect to their field sample. Even though their result was later questioned (e.g. Bottinelli & Gouguenheim 1974, Tully & Shaya 1984), their conclusion remains in agreement with more recent observations (e.g. Haynes & Giovanelli 1986, Solanes et al. 2002).

Over the years, discussions have been going on in the definition and quantification of the H I deficiency parameter (see e.g. Haynes et al. 1984a, Giovanelli & Haynes 1988, Solanes et al. 2002, Safonova 2011). For spiral galaxies, the best normalisation seems to be provided by the disk: the H I, as a disk constituent, is characterised by a nearly constant surface density $\Sigma_{\text{H I}}$. Using the morphologies and H I contents of spiral galaxies, some authors (e.g. Chamaraux et al. 1980, Haynes et al. 1984b, Solanes et al. 1996) quantified the H I deficiency as

$$\langle \text{DEF}_{\text{H I}} \rangle = \langle \log M_{\text{H I}}(D, T) \rangle - \log M_{\text{H I}} \tag{5.1}$$

where $M_{\text{H I}}$ is the H I mass of the galaxy in solar mass. The term $\langle \log M_{\text{H I}}(D, T) \rangle$ is the expected value of the H I mass inferred from a sample of field galaxies of the same optical linear diameter D and morphological type T. Equation 5.1 was later approximated by Solanes et al. (1996; 2002) to a distance-independent relationship. The authors considered the fact that for the $M_{\text{H I}} - D$ relationship do not substantially deviate from a constant H I surface density, and therefore an approximation based on H I surface density rather than H I mass is reasonable. This distance-independent calibrator is given by (Solanes et al. 2002):

$$\mathrm{DEF}_{\text{H\,I}} = \langle \log \overline{\Sigma}_{\text{H\,I}}(T) \rangle - \log \overline{\Sigma}_{\text{H\,I}} \tag{5.2}$$

where the *hybrid* H I surface density

$$\overline{\Sigma}_{\text{H\,I}} = \int S \, dv / a^2 \tag{5.3}$$

is defined as the ratio of the line flux and the apparent optical diameter a of the galaxy (Solanes et al. 1996). The term $\langle \log \overline{\Sigma}_{\text{H\,I}}(T) \rangle$ is the expected *hybrid* H I column density value for a field galaxy of the same morphological type T.

In the present work, we estimate the neutral gas deficiency parameters in our sample galaxies using Eqs 5.2 and 5.3. We also adopt, for the expected *hybrid* H I column density, the values given in Solanes et al. (2002). The uncertainty on the deficiency was obtained by propagating Eq. 5.2, accounting for only the error on $\overline{\Sigma}_{\text{H\,I}}$.

The derived deficiency parameters of the different objects are listed in Table 5.2 for both the KAT-7 and WSRT data, respectively. As one can notice, most galaxies in the sample are H I deficient, with deficiency parameter ranging up to as high as ~ 0.7. Only two galaxies, namely late-type spirals UGC 7590 and NGC 4411B, do not present H I deficiency.

5.2 Star formation in the detected galaxies

Star formation in galaxies generally occurs in their disks, where cold molecular clouds form. How frequent a galaxy forms stars define its evolutionary path. In fact, in the course of its evolution, a galaxy undergoes different stages of star formation; and since stars form out of gas, their atomic (and molecular) gas content varies. SFRs of nearby galaxies can be studied either locally or globally. While the former focuses on individual sub-kpc regions within galaxies (e.g. Scoville et al. 2001), the latter bears interest to the overall SFR of an entire galaxy, using its average luminosity across local variations in star formation history and physical conditions.

For about three decades, different techniques and indicators have been used to estimate the star formation rate in galaxies (see Donas & Deharveng 1984, Kennicutt 1998, Rieke et al. 2009, Kennicutt & Evans 2012, Calzetti 2013). These imply observations across the full electromagnetic spectrum, from the X-ray all the way to the radio. Different empirical relations have been established and calibrated using different indicators, with the most widely used that of Schmidt-Kennicutt (Kennicutt, Jr. 1998)

$$\frac{\mathrm{SFR}}{\mathrm{M}_\odot\,\mathrm{yr}^{-1}} = \frac{L_{\mathrm{FIR}}}{5.8 \times 10^9\, L_\odot} \tag{5.4}$$

making use of the total FIR luminosity L_{FIR}.

In the infrared, SFRs of galaxies are estimated using dust properties. The interstellar dust attenuates the short-wavelength (UV-optical) radiation from stars and ionised gas and re-emits in infrared (see Draine 2003, Sauvage et al. 2005). With the launch of the *Spitzer Space Telescope* (Werner et al. 2004), studies have been intensified to calibrate infrared SFR indicators at different redshifts (e.g. Wu et al. 2005, Calzetti et al. 2007; 2010, Galametz et al. 2013, Lee et al. 2013). These calibrations seek to minimise the uncertainties in the estimate of galaxies SFRs, and offer better empirical relationships.

5.2.1 Star formation rates

We investigate the star formation (SF) in the galaxies in the observed region using empirical relations. To this end, we retrieved Wide-field Infrared Survey Explorer (*WISE,* Wright et al. 2010) W3 band data at 12 μm of the detected galaxies. This band is mostly dominated by the 11.3 μm polycyclic aromatic hydrocarbon (PAHs; Leger & Puget 1984, Allamandola et al. 1985; 1989) and, at a lower magnitude, the [Ne II] emission lines. While the [Ne II] mostly comes from emission from HII regions, the 11.3 μm PAHs, are excited primarily by ultraviolet radiation from both young and evolved stars (Peeters et al. 2004b). They constitute a major component of dust models (Zubko et al. 2004) and, because of their high cumulative surface area, they are believed to be responsible for most of the photoelectric heating of the gas in photodissociation regions and the neutral ISM (e.g Hollenbach & Tielens 1997).

Different studies with the *Infrared Space Observatory (ISO)* and *Spitzer* have found trends between PAH band ratios and various properties of galaxies such as star formation rate and galaxy morphology (see Peeters et al. 2004a, Farrah et al. 2007, Galliano et al. 2008), making the PAH molecules a good tracer of star formation in galaxies. The W3 band is therefore a suitable band to study star formation rates in galaxies, especially nearby galaxies such as those in the outskirt of the Virgo Cluster observed in the present work.

From the W3 magnitudes $m_{12\,\mu\mathrm{m}}$, we estimated the W3 fluxes

$$F_{\nu_{12\,\mu\mathrm{m}}} = F_{\nu_{\mathrm{iso}_{12\,\mu\mathrm{m}}}}\, 10^{-0.4\, m_{12\,\mu\mathrm{m}}} \tag{5.5}$$

and luminosities

$$L_{12\,\mu\mathrm{m}} = \nu_{\mathrm{iso}_{12\,\mu\mathrm{m}}}\, L_{\nu_{12\,\mu\mathrm{m}}} \tag{5.6}$$

where $\nu_{\mathrm{iso}_{12\,\mu\mathrm{m}}} = 2.6753 \times 10^4$GHz is the band's isophotal central frequency and $F_{\nu_{\mathrm{iso}_{12\,\mu\mathrm{m}}}} = F_{\nu_{12\,\mu\mathrm{m}}}(\mathrm{Vega}) = 31.674\,\mathrm{Jy}$ is the "idealised" Vega in-band flux (Jarrett et al. 2011).

The luminosities are furthermore converted into optical SFR – as one would measure from Hα line – by using the empirical relationship by Cluver et al. (2014)

$$\log\left(\frac{\mathrm{SFR}_{\mathrm{H}\alpha}}{\mathrm{M}_{\odot}\,\mathrm{yr}^{-1}}\right) = 1.13\,\log\left(\frac{L_{12\,\mu\mathrm{m}}}{L_{\odot}}\right) - 10.24. \tag{5.7}$$

An error propagation on the above equation yields the uncertainty on $\log(\mathrm{SFR}_{\mathrm{H}\alpha})$:

$$\sigma(\log \mathrm{SFR}_{\mathrm{H}\alpha}) = 1.13\,\sigma(\log L_{12\,\mu\mathrm{m}}) \tag{5.8}$$

where $\sigma(\log L_{12\,\mu\mathrm{m}})$ is obtained from propagating Equation 5.6.

Figure 5.1 shows the plot of the SFR against the H I mass. For comparison, we also plotted on the same figure the relation

$$\log\left(\frac{\mathrm{SFR}}{\mathrm{M}_{\odot}\,\mathrm{yr}^{-1}}\right) = 1.1\,\log\left(\frac{M_{\mathrm{HI}}}{\mathrm{M}_{\odot}}\right) - 10.7 \tag{5.9}$$

derived in Cluver et al. (2010) by applying a linear least-squares fit to the *Spitzer* Infrared Nearby Galaxy Survey (SINGS, Dale et al. 2009) galaxies. The authors determined the sample galaxies SFRs from their Hα emission. The SINGS galaxies are *normal*, moderately bright ($L_{\mathrm{FIR}} < 10^{11}\,L_{\odot}$) galaxies with distances ranging out to $\sim$ 25 Mpc, and located in a wide range of environments (isolated galaxies, interacting galaxies, group and cluster members) (Dale et al. 2009). Although the SINGS galaxies do not cover a representative range of galaxy environments, they span a large range of galaxy physical properties such as nuclear activity, inclination, surface brightness, bar structure, etc. (Kennicutt, Jr. et al. 2003).

As Fig. 5.1 shows, the galaxies of our sample present a normal star formation activity compared to the SINGS sample; except for the late spiral UGC 7590 which appears to be relatively quiescent. The upward arrow on the error bar of UGC 7557 indicates an underestimation of the SFR of the galaxy. This is because the galaxy appears faint in the W3 12μm band, with a signal-to-noise ratio of 1.6. In fact, because we are dealing with resolved sources, the magnitudes of the individual objects are extracted by fitting an ellipse to their infrared images*. This approach is somewhat different from that used for point sources – or unresolved galaxies – to which a point spread function (PSF) is fitted. To UGC 7557, however, the latter approach was applied and the magnitude used was obtained from the profile fit (see Fig. 5.2). This resulted in a brightness lower than the true brightness, inducing a bias in the estimation of the galaxy's SFR. The derived SFR of the object therefore represents the lower limit.

5.2.2 Specific star formation rates

We further proceeded to investigate the specific star formation rates (sSFRs) of the galaxies, that is, their SFR per stellar mass ($\mathrm{sSFR} = \mathrm{SFR}/\mathrm{M}_{\star}$). While SFRs estimate the mass of stellar material being formed in the galaxies per year, the sSFRs go further to normalise the star formation as a function of the host galaxy. To achieve this, we first evaluate the stellar

---

*The photometry was provided by Thomas Jarrett

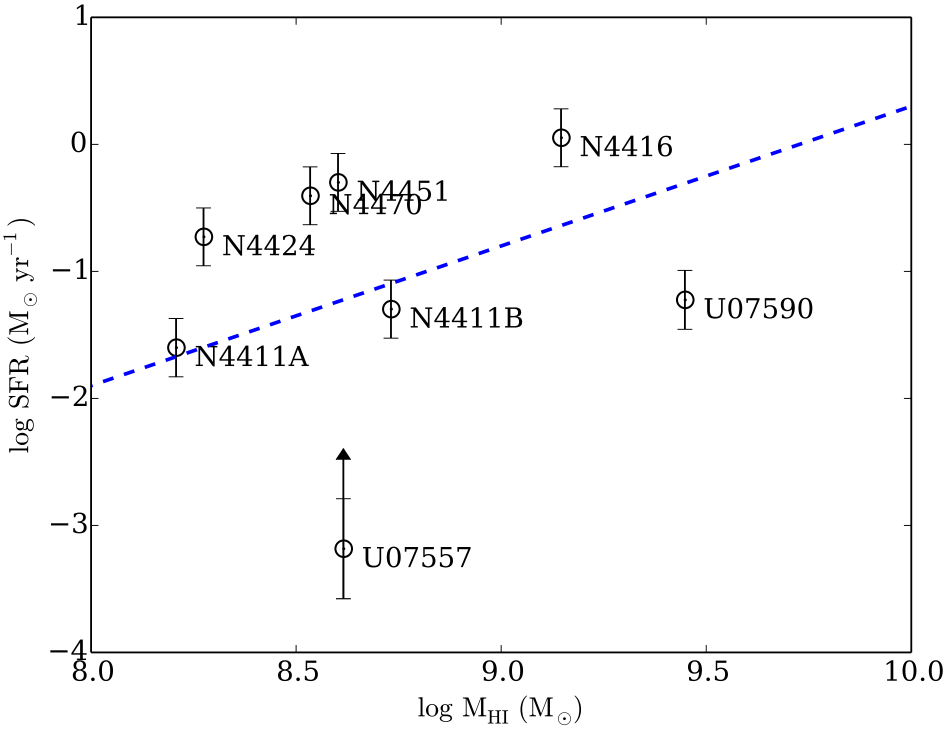

Figure 5.1: SFR vs. HI mass for galaxies detected in the KAT-7 and/or WSRT data and having optical counterpart. The blue dotted line represents the fit obtained by Cluver et al. (2010) with the SINGS galaxies. See text for details.

mass of the galaxies from their *WISE* luminosities and colours (Cluver et al. 2014)

$$\log\left(\frac{M_\star}{L_{3.4\,\mu\mathrm{m}}}\right) = -1.96(m_{3.4\,\mu\mathrm{m}} - m_{4.6\,\mu\mathrm{m}}) - 0.03 \tag{5.10}$$

with the W1(3.4μm) band luminosities $L_{3.4\,\mu\mathrm{m}}$ given by

$$L_{3.4\,\mu\mathrm{m}} = 10^{-0.4(M_{3.4\,\mu\mathrm{m}} - M_{\odot W1})} \tag{5.11}$$

where $M_{3.4\,\mu\mathrm{m}}$ and $M_{\odot W1} = 3.24$ are respectively the source's absolute magnitude and the Sun's magnitude in the W1 band.

The uncertainty on $M_\star$ was evaluated by propagating Equation 5.10, and combining with Equation 5.7, the uncertainty on sSFR was determined (see Table 5.1).

The left panel of Fig. 5.3, which plots the relative neutral gas content of the detected galaxies (i.e, their neutral gas to stellar mass ratio) versus their stellar mass, approximately shows the trend expected from star formation theories in galaxies: the gas fraction decreases with an increasing stellar mass (see e.g. Catinella et al. 2013). This suggests that higher mass galaxies, which have lower gas fraction, may have exhausted most of their gas by turning

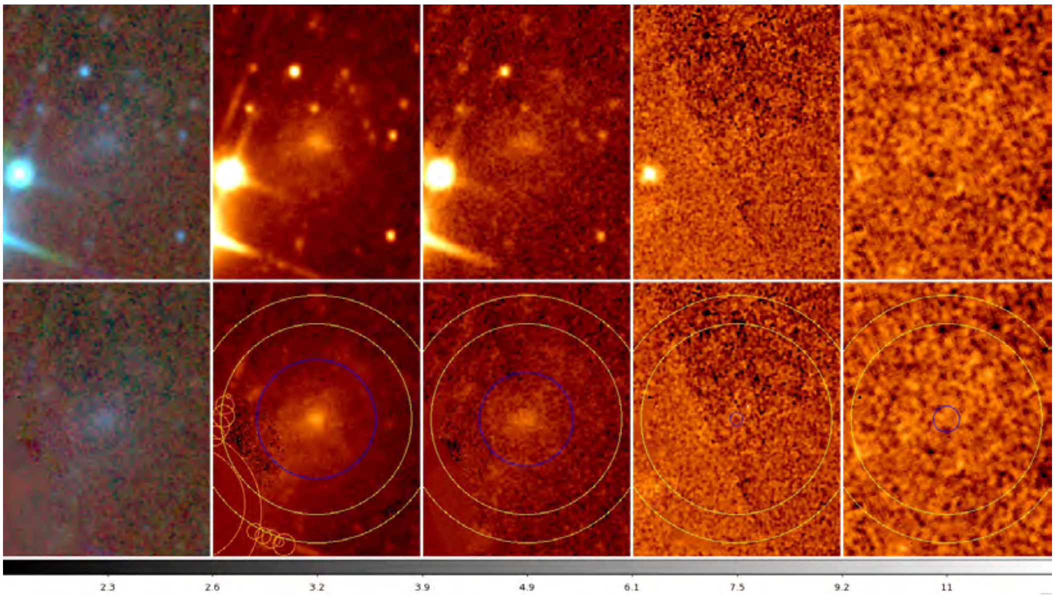

Figure 5.2: Optical and WISE images of UGC 7557. *From left to right:* Optical, W1, W2, W3 and W4 images of the galaxy. The *bottom panels* show the ellipses used to fit the magnitude of the object in the different bands.

them into stars. On the other hands, lower stellar mass galaxies still have a relatively higher gas fraction available to fuel future star formation activity. This implies that the star formation activity plays an important role in driving the gas removal in galaxies. The plot also shows that none of the detected galaxies is exceptionally big ($M_\star < 10^{10.5}\,\mathrm{M}_\odot$), and NGC 4424 happens to have the lowest gas fraction. Furthermore, for comparison, we plotted on the same panel a fit derived in Perez-Gonzalez et al. (2003) using a sample of 191 galaxies at an average redshift of $z = 0.026$ from the UCM Survey (Zamorano et al. 1994; 1996). Not only all the galaxies in our sample follow the trend and lie within the one standard deviation of their fit, but the majority of them – all but one – lie in below the fit. This suggests that our sample galaxies, which are nearby galaxies like the UCM sample galaxies, present lower neutral gas fraction than UCM galaxies. This is in agreement with the idea that cluster environments contribute in removing gas inside galaxies.

We then derived the sSFRs of the sample galaxies by dividing their SFR by their respective stellar masses. The right panel of Fig. 5.3 gives the plot of the sSFR against $M_\star$ for the sample. Also plotted on the same figure are the lines of constant SFR at 0.01, 0.1 and $1\,\mathrm{M}_\odot\,\mathrm{yr}^{-1}$. Unlike the SFR, the behaviour of the sSFR is in contrast with the expected trend: in fact, previous studies with large galaxy samples found a decrease of the sSFR with increasing stellar mass, independently of the redshift (e.g. Perez-Gonzalez et al. 2003, Bauer et al. 2005, Catinella et al. 2013, Cluver et al. 2014); suggesting, in the current understanding of galaxy evolution, that star formation contributes more to the growth of low-mass galaxies than to the growth of high-mass galaxies. This trend is not seen in the figure most likely because of the reduced size of the sample. Relative to the overall sample, NGC 4424, which has the lowest gas content, presents a *normal* sSFR despite its neutral gas being stripped off.

5.2.3 Star formation rate density

In this last section on investigating the star formation activity in the galaxies, we attempt to evaluate the relationship between the star formation rate density, or the disk-averaged SFR per unit area, and the HI surface density. This is given in Fig. 5.4. Unlike with the total and molecular gas with which the SFR density increases (see e.g. Kennicutt, Jr. 1998), the correlation seen in Fig. 5.4 presents a decrease of SFR density with increasing HI surface density. Also, this is in contrast with the correlation obtained by Duc et al. (2013) using a sample of star forming regions in mergers. This anticorrelation is not well understood and further investigation needs to be carried.

Table 5.1: Star formation properties of the detections.

Object	R.A	Dec.	log (SFR)	log (sSFR)	$M_\star$	log ($\Sigma_{\rm SFR}$)
	J2000		$M_\odot\,yr^{-1}$	yr^{-1}	$10^9 M_\odot$	$M_\odot\,yr^{-1}\,kpc^{-2}$
NGC 4424	12 27 11.6	09 25 14	-0.728 ± 0.228	-10.751 ± 0.246	10.539 ± 2.242	-3.017 ± 0.236
NGC 4451	12 28 40.5	09 15 31	-0.299 ± 0.228	-10.429 ± 0.246	13.475 ± 2.889	-2.850 ± 0.236
NGC 4470	12 29 37.8	07 49 27	-0.405 ± 0.228	-10.340 ± 0.246	8.620 ± 1.848	-3.181 ± 0.236
UGC 7590	12 28 18.8	08 43 46	-1.224 ± 0.232	-10.729 ± 0.251	3.195 ± 0.708	-3.769 ± 0.240
Cloud 7c	12 30 25.8	09 28 01	—	—	0.057 ± 0.027	—
NGC 4411A	12 26 30.0	08 52 18	-1.601 ± 0.229	-10.858 ± 0.249	1.807 ± 0.400	-3.941 ± 0.238
NGC 4411B	12 26 47.2	08 53 04	-1.297 ± 0.229	-11.168 ± 0.247	7.416 ± 1.615	-3.767 ± 0.237
UGC 7557	12 27 11.1	07 15 47	>-3.184 ± 0.394	>-12.314 ± 0.408	1.352 ± 0.334	-2.946 ± 0.398
NGC 4416	12 26 46.7	07 55 08	0.052 ± 0.228	-10.415 ± 0.246	29.315 ± 6.284	-2.944 ± 0.236

5.3 Environmental effects on the galaxies

In this section we try to understand the different environmental effects responsible of the properties of the detected galaxies, especially the HI tail of NGC 4424.

5.3.1 Disturbed gas kinematics

From Table 4.4 listing some parameters of the galaxies, it becomes apparent that their kinematics, at least from an HI point of view, is disturbed. The rotation velocities of the galaxies are low, and resemble those of dwarf galaxies. This resulted in an underestimation of their TF distances. In particular, NGC 4424 which is an early spiral, has an HI-derived maximum rotational velocity of only $29\,\mathrm{km\,s^{-1}}$, in agreement with values in the literature (e.g, HYPERLEDA lists a value of $30\,\mathrm{km\,s^{-1}}$ and Cortés et al. (2006) found $31 \pm 4\,\mathrm{km\,s^{-1}}$).

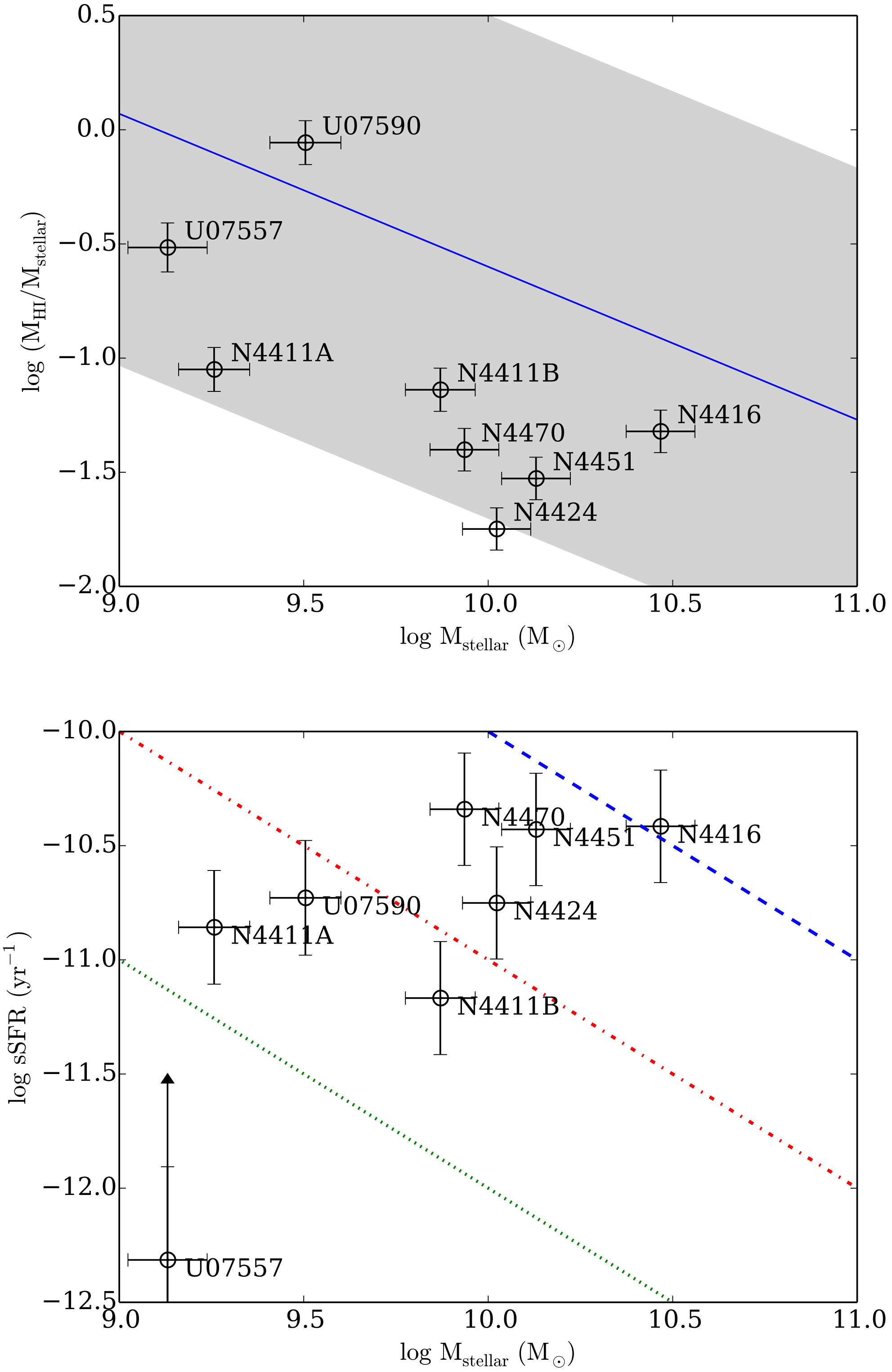

Figure 5.3: *Top panel:* HI gas fraction of the galaxies detected in the KAT-7 and/or WSRT data and having optical counterpart, as a function of their stellar mass. The *blue line* shows, for comparison, a fit obtained by Perez-Gonzalez et al. (2003) with the UCM sample. The *grey* area shows the error of the fit. *Bottom panel:* sSFR vs. stellar mass for the same galaxies. Lines of constant SFR of 0.01 *(green)*, 0.1 *(red)* and $1\,\mathrm{M_{\odot}\,yr^{-1}}$ *(blue)* are also shown.

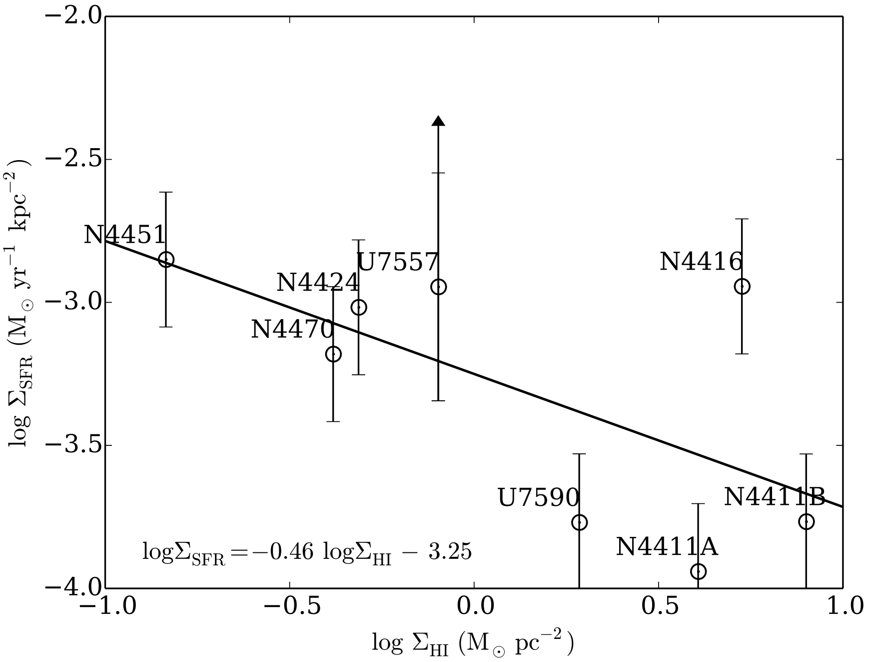

Figure 5.4: SFR density vs. average HI surface density for galaxies detected in the KAT-7 data and having optical counterpart. A linear least-squares fit is also presented.

A similar result was obtained by Rubin et al. (1999) when they observed 89 disk galaxies in the Virgo Cluster. They found that many Virgo galaxies, $\sim 50\%$ of the total, have experienced several significant kinematic disturbances during their lifetimes, with some galaxies having ionised gas in their central region and presenting anomalously low rotational velocities. This suggests that tidal encounters are relatively frequent in the cluster. In the next two sections, we discuss the particular case of NGC 4424, the most interesting galaxy in this respect. It presents a south-west HI tail pointing towards the elliptical M49.

5.3.2 Ram pressure stripping

The overall structure of NGC 4424, with the one-sided HI tail, is typical to ISM-ICM interactions, particularly the ram pressure. As mentioned in section 1.4.1, ram pressure stripping in galaxies occur in special conditions. A major factor influencing its intensity is the orbit followed by the galaxy: galaxies on radial orbits are more likely to undergo ram pressure stripping (Vollmer et al. 2001). This is because radial orbits allow galaxies to *travel* closer to the centre of the cluster where both the galaxy and the ICM density is substantially higher. In these regions, the gravitational potential of the galaxies increases, and their velocities considerably increase. Mathematically, galaxies can be gas-stripped by ram pressure only when the ram pressure is larger than the restoring force, i.e, when (Gunn

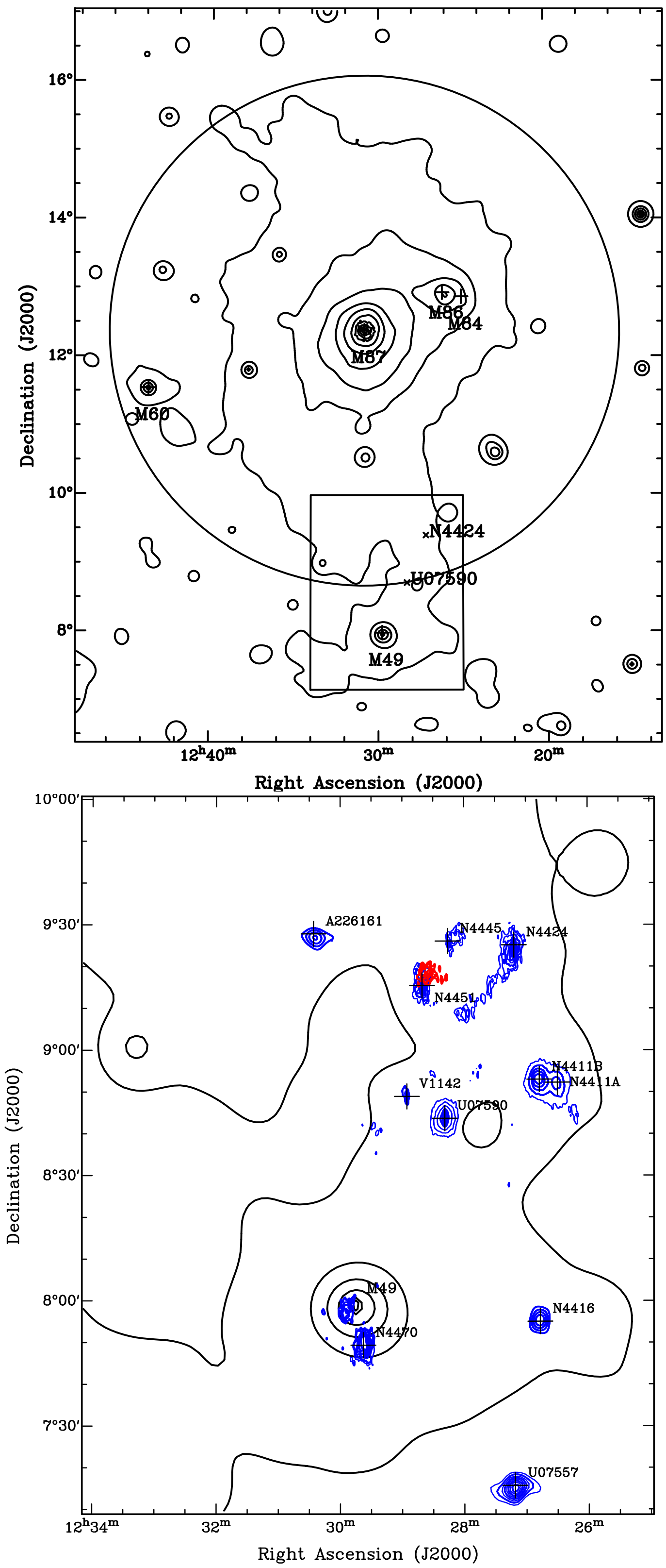

Figure 5.5: *Top:* Same as in Figure 4.1. The labelled plus signs show the major ellipticals of the cluster, and the crosses indicate, for guidance, the positions of the HI-tailed NGC 4424 and the galaxy UGC 7590. *Bottom:* The zoomed-in observed region, as covered by the KAT-7. As on the top panel, the black contours are the X-ray levels. The blue and red contours are HI column densities (as obtained from the combined map), ranging from 5×10^{18} to 8×10^{20} atoms cm^{-2}. The red contours show an HI cloud with no optical counterpart, $\sim 400\,\mathrm{km\,s^{-1}}$ behind NGC 4451.

& Gott, J. Richard 1972)

$$\rho_{\rm ICM}\, v_{\rm gal}^2 > \Sigma_{\rm ISM}\, v_{\rm rot}^2/R. \tag{5.12}$$

Here $p_{\rm ram} = \rho_{\rm ICM}\, v_{\rm gal}^2$ is the ram pressure and the right-hand side represents the restoring force. $\rho_{\rm ICM}$ is the ICM density and $v_{\rm gal}$ is the galaxy's velocity in the ICM. Additionally, $\Sigma_{\rm ISM}$ is the surface density of the ISM, $v_{\rm rot}$ is the galaxy's rotational velocity and R its radius. Chung et al. (2007) compared the ram pressure to the restoring force in HI-tail'ed Virgo galaxies using the simulations of Vollmer et al. (2001). They found that for NGC 4424, the ram pressure could exceed the restoring force, meaning that ram pressure is most likely at the origin of the HI tail.

Several observations and simulations showed that ram pressure may be effective in removing cluster galaxies' gas out to $1-2$ virial radii (e.g. Kenney et al. 2004, Crowl & Kenney 2005, Tonnesen et al. 2007, Bahe et al. 2013). Figure 5.5 (top panel) shows the position of NGC 4424 relative to the virial radius of the galaxy. The galaxy is located 3.1° away from M87, that is, ~ 0.8 virial radius away from the centre of the galaxy. The virial radius of the Virgo Cluster adopted here is $r_{\rm vir} = 1.08$ Mpc (Arnaud et al. 2005, Urban et al. 2011), which corresponds to a projected radius of $\sim 3.7°$ at M87's distance of 16.8 Mpc.

Furthermore, Chung et al. (2007) found that the HI disk of the galaxy is truncated to well within its stellar disk, direct evidence of ICM-ISM interaction. Fig. 4.3 (3rd panel) does not show a severe truncation, though we see an elongated HI distribution along the minor axis of the galaxy and in the direction of the tail. The attenuation of HI disk truncation might be due to an observational effect, the beam dilution, due to the lower resolution of the data.

From the star formation activity point of view, NGC 4424 does not present strong evidence of ram pressure. The derived SFR of the galaxy is relatively *normal*, with respect to the other galaxies of the region. Whether or not ram pressure can enhance or reduce star formation in a galaxy depends both on its position with respect to the cluster centre, and the ICM density. Using analytic models of galaxy evolution in clusters, Fujita & Nagashima (1999) predicted that SFRs of disk galaxies can increase to up to twice their initial value in a cluster with high gas density and a deep potential well (due to molecular gas compression), and change less significantly in a cluster with low gas density and a shallow potential well. Recent simulations (Bekki 2013) showed that the effect of ram pressure on star formation is function of the halo mass and inclination of the galaxy. They found that for low-mass halos ($M_{\rm h} \sim 10^{10}\,{\rm M}_\odot$), ram pressure can quench star formation at the pericentre passages in a cluster with $M_{\rm h} \sim 10^{14}\,{\rm M}_\odot$ ($M_{\rm h} \sim 10^{15}\,{\rm M}_\odot$ for Virgo, Fouqué et al. 2001). Although the dynamical mass derived for NGC 4424 (see Table 4.3) suggests that the galaxy has a low-mass halo, what stage of ram pressure it is currently undergoing as well as the pericentre of its orbit remain uncertain.

5.3.3 Tidal stripping

The ram pressure stripping is very likely to be occurring in NGC 4424, but it does not fully explain the complex morphology of the galaxy. In fact, it is classified as a *chaotic* early spiral in the Uppsala General Catalogue (UGC, Nilson 1973), a peculiar Sa by Binggeli et al. (1985), and an uncertain barred Sa by de Vaucouleurs et al. (1991). Its Hα morphology has been described as *truncated/compact* by Koopmann & Kenney (2004). Optical observations of the galaxy reveal that it has a heavily disturbed stellar disk, and shows a strong Hα emission confined to its central kpc (Kenney et al. 1996, Cortés et al. 2006). On the SDSS R-band images of the galaxy in Fig. 5.6, the unusual morphology is noticeable. The grayscale image (*left panel*) shows a broad S-shaped structure in the outer parts, while banana-shape isophotes are revealed by the contour lines (*right panel*).

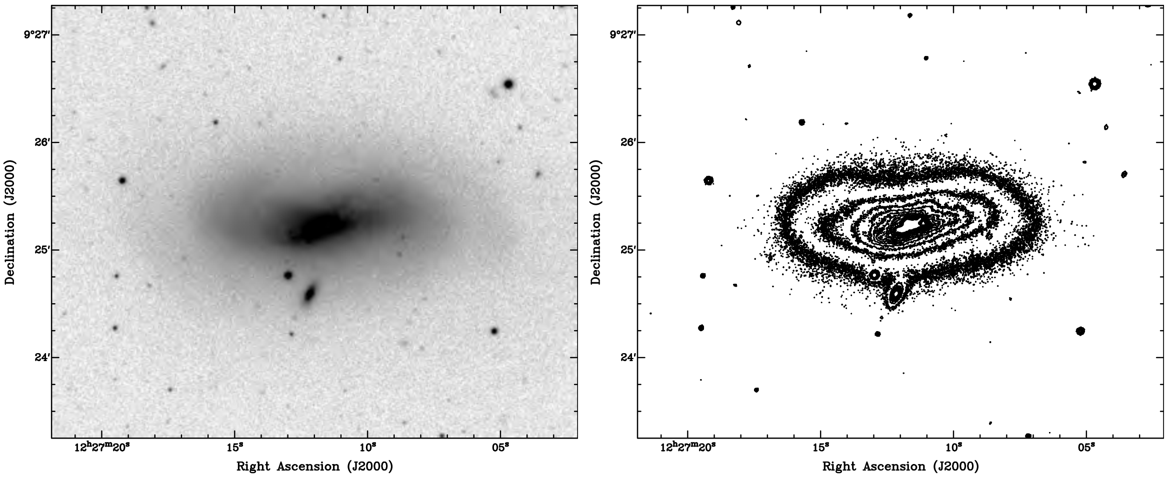

Figure 5.6: NGC 4424 in SDSS R-band grayscale (*left*) and contours (*right*). The small galaxy 1″ south of the nucleus is a background galaxy.

Kenney et al. (1996) found that the peculiar morphological properties of NGC 4424 are consistent with an intermediate mass ratio merger, and suggested that the galaxy might have undergone a significant recent merger. The authors also proposed that the galaxy is on its way to becoming a small-bulge lenticular galaxy within ∼ 1 Gyr. Figure 5.5 shows an HI cloud near the elliptical M49 and without optical counterpart, which is located at a projected distance of ∼ 440 kpc away from NGC 4424. This cloud, previously observed by Sancisi et al. (1987), is at the same systemic velocity as the NGC 4424's tail. Although Sancisi et al. (1987) believed that the cloud was tidally stripped from a dwarf irregular, UGC 7636 (located 5.′6 southeast of M49), they found no strong evidence since no neutral gas was observed at the position of the dwarf, and its radial velocity was furthermore found to be lower ($276 \pm 1\,\mathrm{km\,s^{-1}}$; Binggeli et al. 1993) than that of HI cloud.

Without excluding other possible scenarios, the direction and velocity of the NGC 4424's tail relative to the HI cloud, together with the peculiar properties of NGC 4424 suggests that the galaxy is a merger remnant. This is furthermore supported by the Hα distributions of the galaxy, which are more likely caused by tidal interactions, including minor mergers (Koopmann & Kenney 2004). The HI tail of the galaxy would then be a footprint of this merger.

5.3.4 Have the galaxies already been pre-processed?

The Virgo Cluster is not yet virialized, as there are still infall of galaxies in the cluster (e.g. Tully & Shaya 1984). It is believed, for instance, that the M49 subcluster is falling into the centre of the Virgo Cluster. One should therefore expect the galaxies in the subcluster to undergo, at some stage of their infall, a preprocessing (Fujita 2004, Boselli & Gavazzi 2006). The X-ray emission of the hot gas in the region (see Fig. 5.5) suggests that the galaxies may be following a filamentary structure in their infall in the centre of the Virgo cluster. However, in the observed sample of galaxies, only NGC 4424 shows signs if severe environmental effects. The lack of (severe) ram pressure stripping in the other galaxies may be explained, *inter alia*, by their different orbits.

Fig. 5.7 shows the neutral gas fraction and deficiency parameter ($\mathrm{DEF_{HI}}$), respectively, as a function of the projected distance from the centre of the cluster. The vertical line in the plots of Fig. 5.7 shows the approximate location of the cluster's virial radius, and the horizontal line of the right panel separates the HI-deficient galaxies from the non-deficient ones. The plots show no strong correlation of either the HI gas content or the deficiency with the galaxies distance from the cluster centre, although most of the low gas fraction galaxies lie within the virial radius. This lack of correlation is not surprising, given the relatively small volume of the probed region and the limited number of detected objects. Further analysis should extend the sample to include a broader range of radii.

The properties of the galaxies derived in the present work, including the SF activity, do not provide enough information to confirm whether or not the galaxies have already been pre-processed. However, given that ram pressure is already occurring in a galaxy in the field, namely NGC 4424, and accounting for the distribution of the hot X-ray gas, it is likely that the galaxies are falling into the centre of the cluster along a filament. Furthermore, previous works showed that pre-processing of galaxies occur well before they fall into clusters (e.g. Balogh et al. 1997, Cortese et al. 2006, Mahajan 2013). Therefore, it is more likely that pre-processing has already occurred in the observed galaxies. This might have contributed to the observed lower HI gas contents of the galaxies.

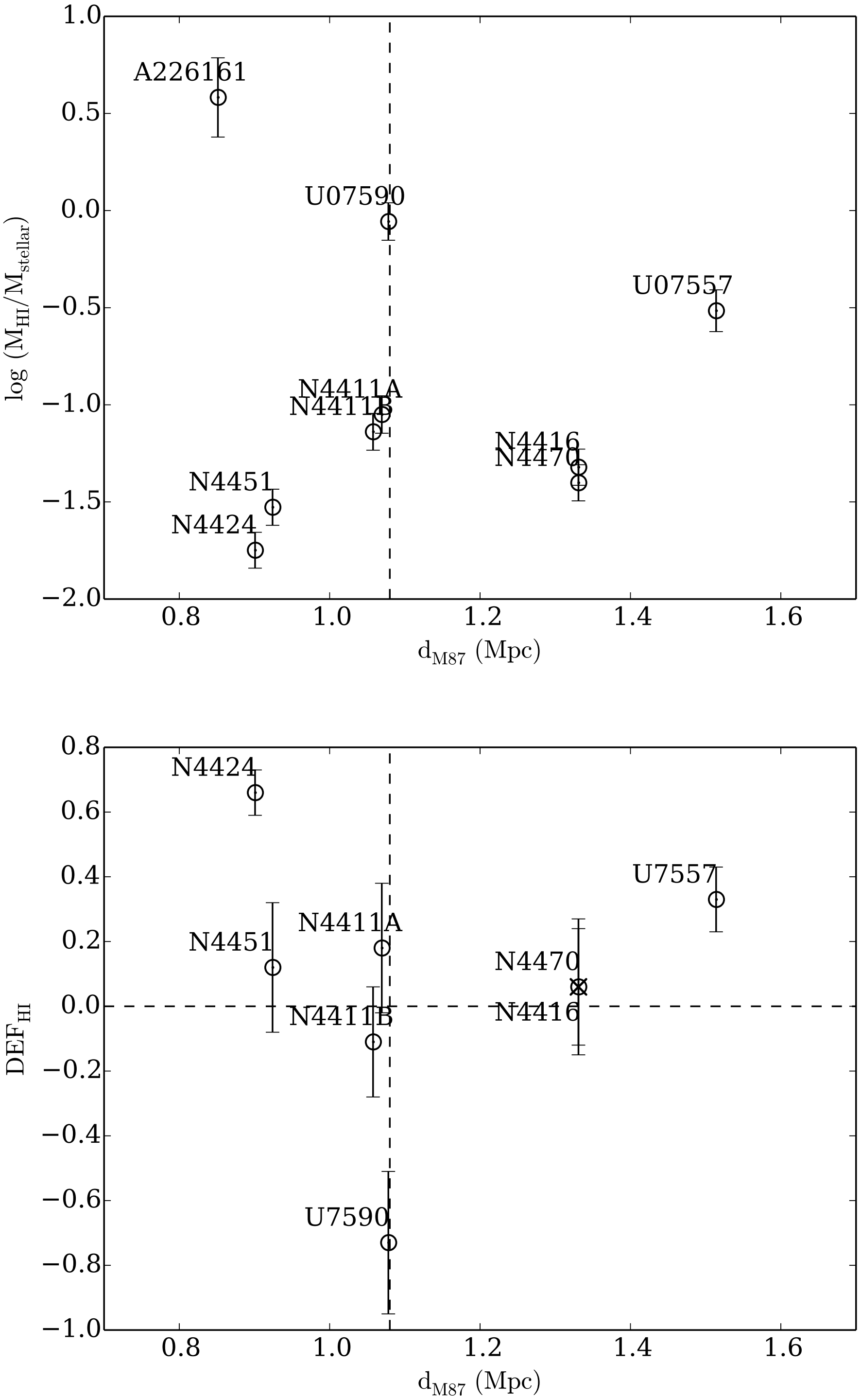

Figure 5.7: HI content (*top panel*) and deficiency (*bottom panel*) of the detected galaxies as a function of their projected distance from the centre of Virgo. The *vertical line* shows the virial radius of the cluster, and the *horizontal line* of the bottom panel separates the HI-deficient galaxies (*upper part*) from the non-deficient (*lower part*).

	(J2000)				KAT-7					WSRT					
Object (1)	R.A (2)	Dec.	Type (3)	D_{25} ($'$) (4)	$v_{\rm sys}$ ($\rm km\,s^{-1}$) (5)	W_{50}^c ($\rm km\,s^{-1}$) (6)	$\int S\,dv$ ($\rm Jykm\,s^{-1}$) (7)	$\log M_{\rm HI}$ ($\rm M_\odot$) (8)	DEF (9)	$v_{\rm sys}$ ($\rm km\,s^{-1}$) (10)	W_{50}^c ($\rm km\,s^{-1}$) (11)	$\int S\,dv$ ($\rm Jykm\,s^{-1}$) (12)	$\log M_{\rm HI}$ ($\rm M_\odot$) (13)	DEF (14)	$d_{\rm M87}$ (deg) (15)
NGC 4424	12 27 11.6	09 25 14	SBa	3.02	433	58.6	3.5	8.3	0.66	433	68.4	3.7	8.3	0.63	3.10
NGC 4451	12 28 40.5	09 15 31	Sab	1.35	864	253.8	2.4	8.6	0.12	855	254.0	1.9	8.5	0.12	3.18
NGC 4470	12 29 37.8	07 49 27	Sa	1.29	2321	136.8	2.5	8.5	0.06	–	–	–	–	–	4.58
UGC 07590	12 28 18.8	08 43 46	Sbc	1.17	1112	177.2	12.8	9.4	−0.73	1113	175.2	11.6	9.4	−0.69	3.71
Cloud 7c	12 30 25.8	09 28 01	HI cloud	–	496	74.0	3.3	8.3	–	–	–	–	–	–	2.93
NGC 4411A	12 26 30.0	08 52 18	Sc	1.62	–	–	–	–	–	1271	105.2	3.0	8.2	0.18	3.68
NGC 4411B	12 26 47.2	08 53 04	Sc	1.90	–	–	–	–	–	1260	153.9	8.1	9.2	−0.11	3.64
UGC 07557	12 27 11.1	07 15 47	Sm	2.75	924	245.2	6.1	8.6	0.33	–	–	–	–	–	5.21

Table 5.2: (1) Object name.
(2) Optical positions.
(3) Morphological type from LEDA.
(4) Optical diameter at surface brightness $\mu = 25$ mag arcsec^{-2}from LEDA.
(5) & (10) Systemic velocities from the KAT-7 & WSRT data respectively.
(6) & (11) HI profile widths from KAT-7 and WSRT respectively, corrected for instrumental effects, turbulence effects, redshift, and inclination, except for Cloud 7c where the correction for inclination has not been applied.
(7) & (12) Integrated total HI flux observed with the KAT-7 and WSRT, respectively.
(8) & (13) Base-10 logarithm of the HI masses in solar units $\log M_{\rm HI}$, assuming that the HI is optically thin.
(9) & (14) HI deficiency parameter defined in Solanes et al. (2002).
(15) Projected angular distance from the elliptical M87 in degrees.

Chapter 6

Conclusion

6.1 Summary of Results

In this work we have used the KAT-7 and WSRT telescopes to observe a region of ~ 2.5° × 1.5° located in the Virgo Cluster, ~ 3° away from the centre of the cluster and containing the elliptical M49. The distribution of the hot X-ray gas in the field suggests a filamentary structure joining the M49 subcluster to the Virgo cluster. With a total of ~ 78 and 48 hours of observations respectively with the KAT-7 and WSRT telescopes, we reached column densities of the order of $\sim 1 \times 10^{18}\,\mathrm{atoms\,cm^{-2}}$ over $16.5\,\mathrm{km\,s^{-1}}$. To detect both the low and high resolution features and benefit from the advantages of both telescopes, we combined the two observations. However, because of the large difference in the flux sensitivities in the two datasets due to the two respective beam areas being different, the combination could not be done in the Fourier plane, as is widely done. We then adopted a new approach, which consists in combining the data in the image plane after converting the fluxes into column densities. This provided us a dataset showing features of both telescopes, that is, a dataset in which both large and small scale structures are detectable down to $\sim 8 \times 10^{17}\,\mathrm{atoms\,cm^{-2}}$ over $16.5\,\mathrm{km\,s^{-1}}$. The column density sensitivity in the resulting data is therefore slightly higher than in the individual data.

A few galaxies with HI mass $M_{\mathrm{HI}} \gtrsim 10^8\,\mathrm{M}_\odot$ were detected, including NGC 4424, a one-sided HI-tailed, early-type spiral galaxy. At a column density of $N_{\mathrm{HI}} \sim 5 \times 10^{18}\,\mathrm{atoms\,cm^{-2}}$, we were able to detect the tail of the galaxy out to an extent of ~ 60 kpc. This is a tail three times longer than previously observed with the VLA telescope.

Various parameters of the detected galaxies such as their HI mass, their mean HI surface density, their velocity widths and their HI deficiency were derived from the observations. An analysis of these parameters shows that from a neutral gas point of view, the detected galaxies are modest in mass, with their HI mass varying from ~ 2 to $\sim 28 \times 10^8\,\mathrm{M}_\odot$. Compared to the values in the literature (mostly ALFALFA results), the extracted HI masses are consistent for ~ 2/3 of the detected galaxies. We also found that most of the detected galaxies are HI-deficient, with their deficiency parameter ranging up to as high as 0.66, which was expected, given their dense environment.

Combining the HI observations to infrared data, we investigated the neutral gas content and star formation rates of the detected galaxies. The HI fraction of the galaxies is found to decrease with their stellar mass, suggesting that star formation might be efficient, besides environmental effects, in depleting the neutral gas in the galaxies.

A comparison of the SFRs of the detected galaxies with those of the SINGS sample shows that half of detected galaxies, including the highly HI-deficient NGC 4424, have relatively high star formation rates. 25% of the detections are relatively quiescent, and the other 25% present normal SFRs.

In an attempt to explain the formation of the HI tail of NGC 4424, our analysis led us to suggest that both ISM-ICM and tidal interactions contributed to form the tail. NGC 4424 is likely to be a post-merger galaxy undergoing a ram pressure stripping as it falls in the Virgo cluster, along a filamentary structure mapped by the hot X-ray gas. From a statistical point of view, the distribution of the gas content in the observed galaxies (as a function of their distance to the cluster centre) do not allow us to derive a strong conclusion on the environmental effects, possibly due to the reduced number of the detections. However, their kinematical parameters derived from the HI data reveal that the galaxies are undergoing environmental effects, in agreement with previous studies.

6.2 Future Prospects

Performing observations to deeper sensitivities than previously obtained allowed us to reveal a hidden portion of NGC 4424's tail. We also detected an HI cloud near M49, that might be leftover gas from a previous merger that occurred in NGC 4424. This probable merger could have then left some gas in between NGC 4424 and M49. Deeper observations might help to detect these eventual clouds if they exist.

A better understanding of the environmental effects can be obtained by comparing the properties of the observed field to a different region of the cluster. A proposal has been submitted to the KAT-7, to observe a region located $\sim 8^\circ$ away from the region observed in the present work, and roughly in the opposite direction of M87. The region contains three galaxies (including NGC 4808) tentatively exhibiting an extended HI envelope, spanning an angular distance of about $\sim 1^\circ$. The galaxies will be observed down to column densities similar to the present observations, and will eventually provide informations about the evolution of the gas content along filaments.

Appendix A

Column density maps and HI profiles of detections

The HI column density maps (top panel) and global HI profiles (lower panels) of the different detections are presented in Figures A.1 to A.8.

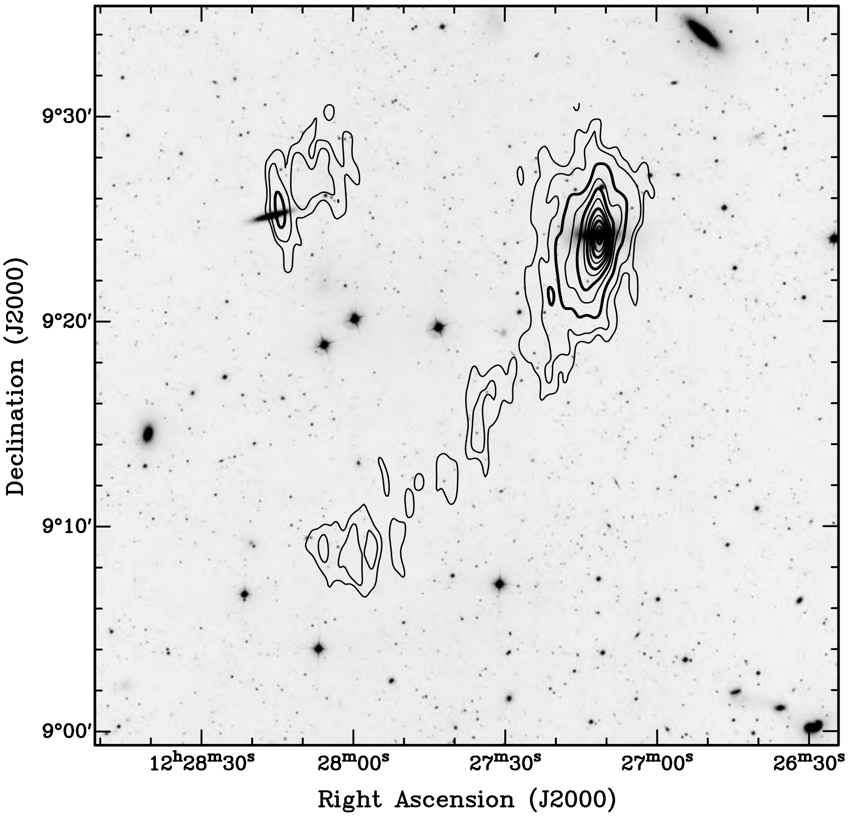

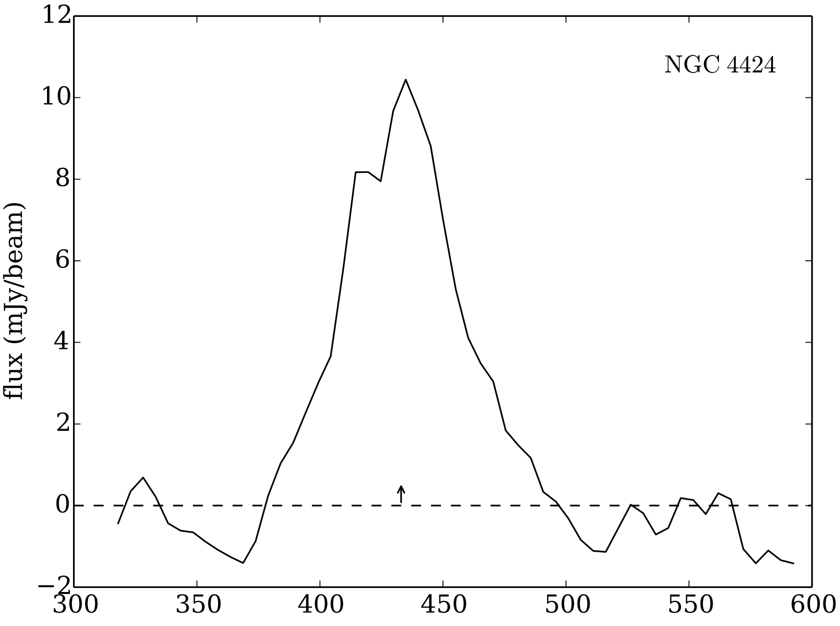

Figure A.1: **NGC 4424**. Contours: 0.5, 1, 2, 3 ... 10 $\times 10^{19}$ atoms cm^{-2}. Systemic velocity: $v_{\rm sys} = 433\,{\rm km\,s^{-1}}$.

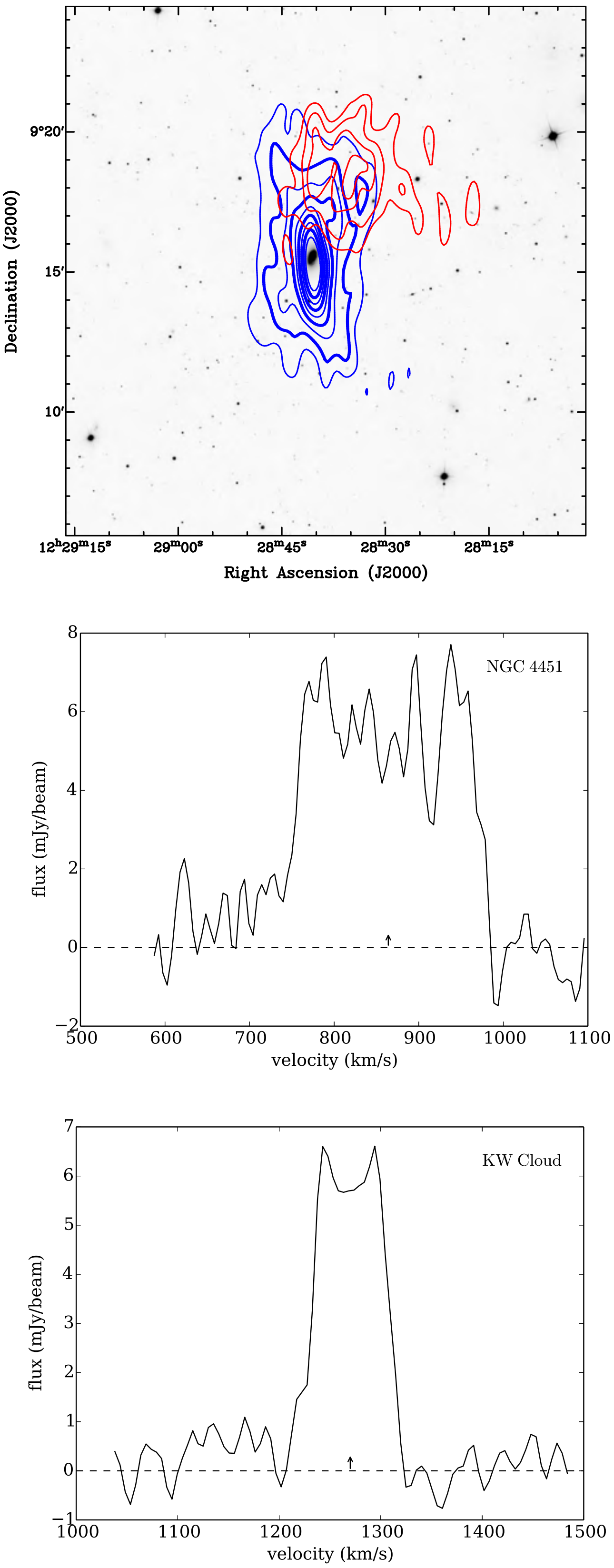

Figure A.2: **NGC 4451:** 1, 2, ..., 9 $\times 10^{19}$ atoms cm^{-2}. $v_{\rm sys} = 864\,{\rm km\,s^{-1}}$.
Gas cloud: 1, 1.5, 2, 2.5 $\times 10^{19}$ atoms cm^{-2}. $v_{\rm sys} = 1270\,{\rm km\,s^{-1}}$.

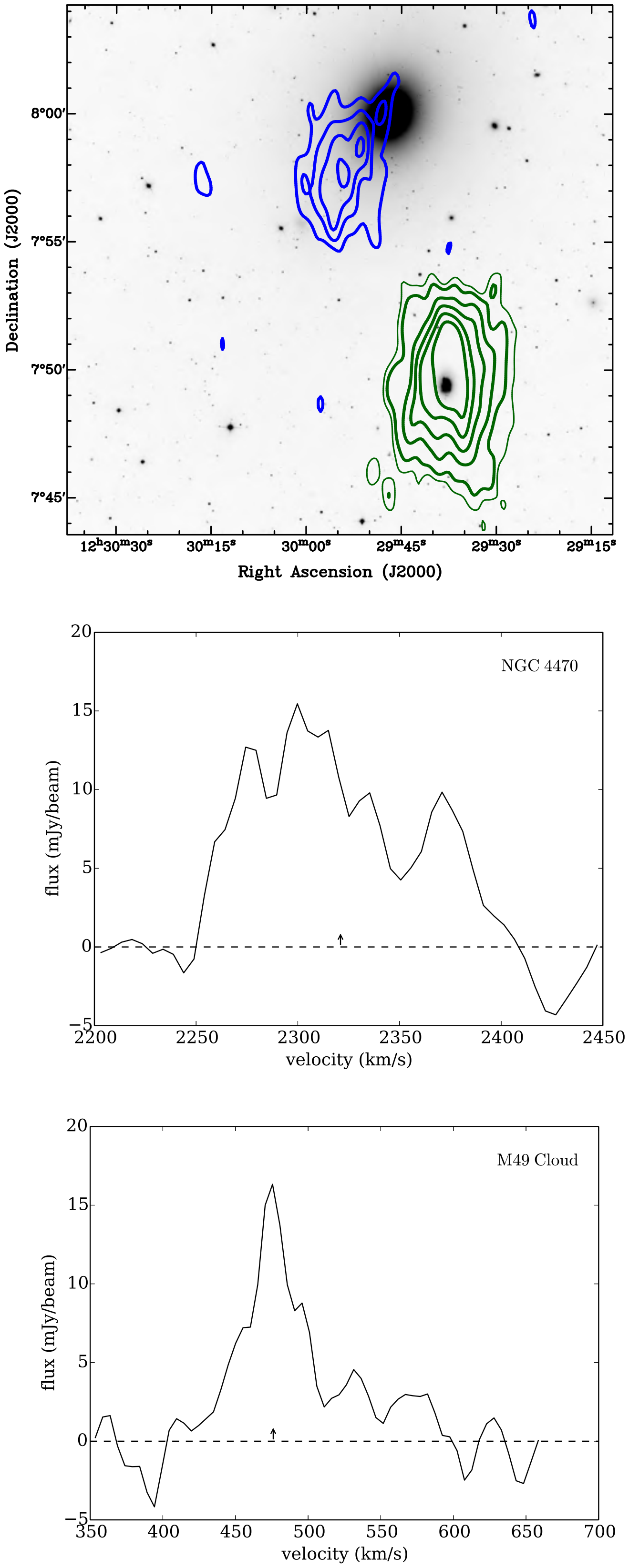

Figure A.3: **NGC 4470:** 0.5, 1, 2, ..., 5 $\times 10^{19}$ atoms cm^{-2}. $v_{\text{sys}} = 2321\,\text{km}\,\text{s}^{-1}$. **M49 Gas cloud:** 1, 1.5, 2, 2.5 $\times 10^{19}$ atoms cm^{-2}. $v_{\text{sys}} = 476\,\text{km}\,\text{s}^{-1}$.

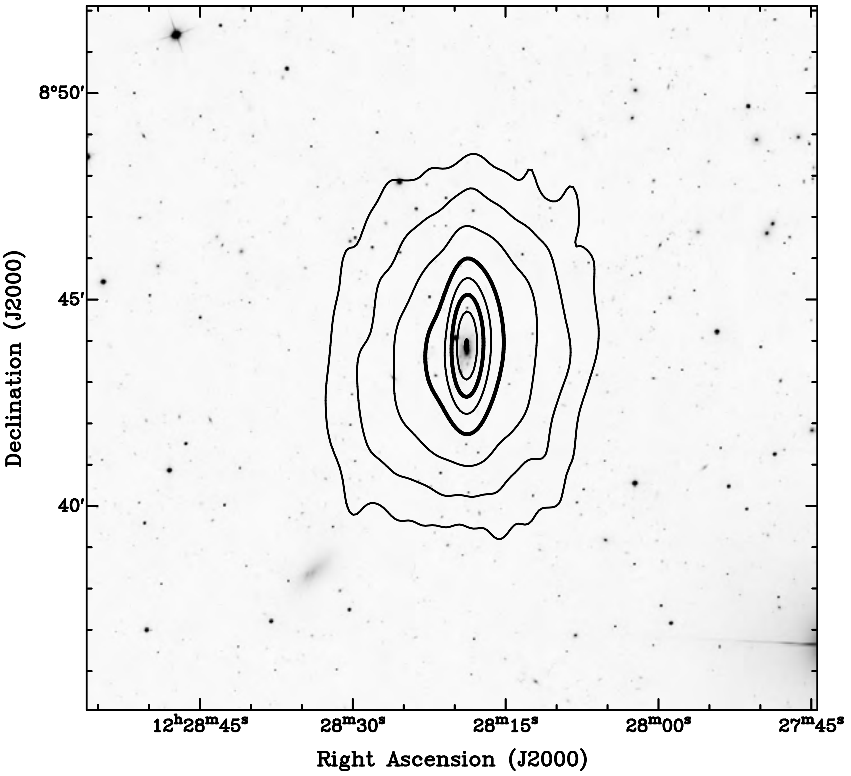

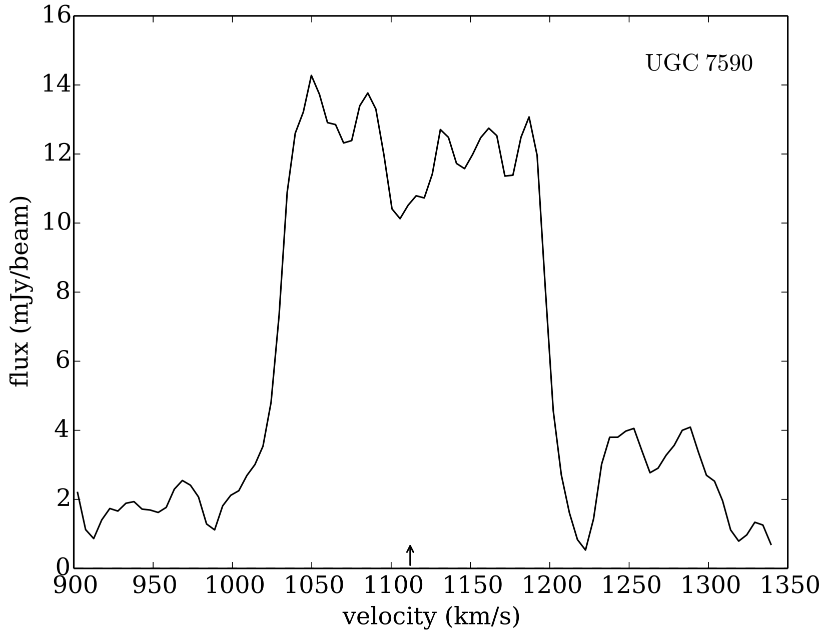

Figure A.4: **UGC 7590**. Contours: 2, 5, 10, 20, 30, ... 60 $\times 10^{19}\,\mathrm{atoms\,cm^{-2}}$. $v_{\mathrm{sys}} = 1112\,\mathrm{km\,s^{-1}}$.

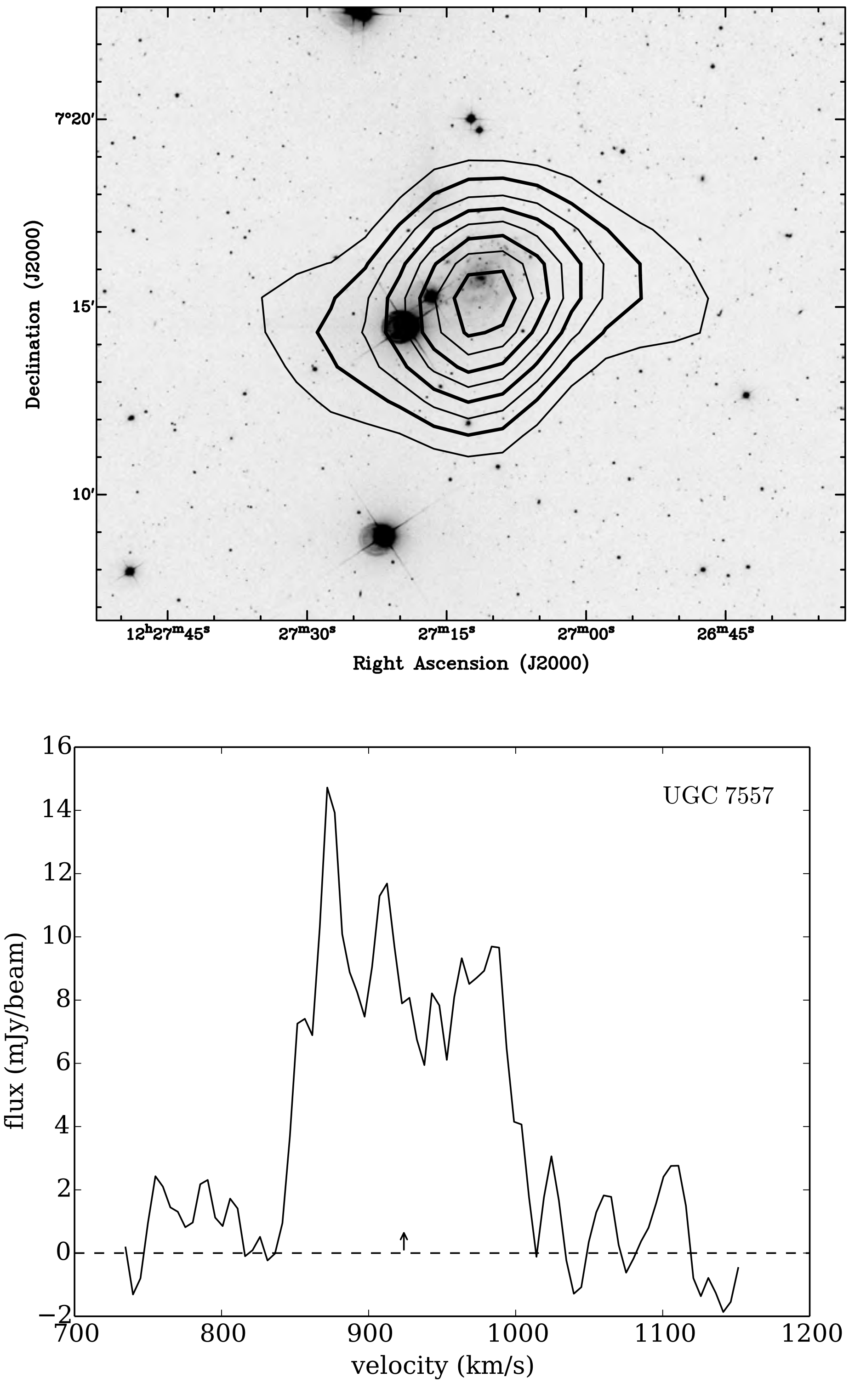

Figure A.5: **UGC 5775**. Contours: 1, 2, ..., 8 $\times 10^{19}$ atoms cm^{-2}. $v_{\mathrm{sys}} = 924\,\mathrm{km\,s^{-1}}$.

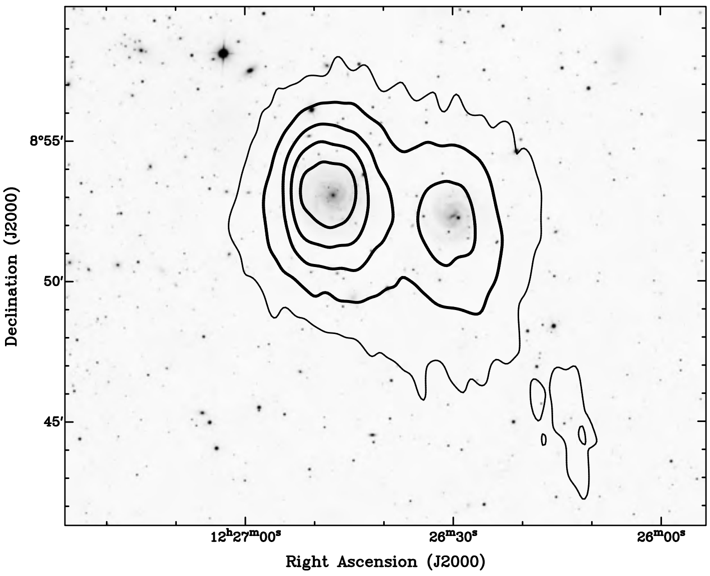

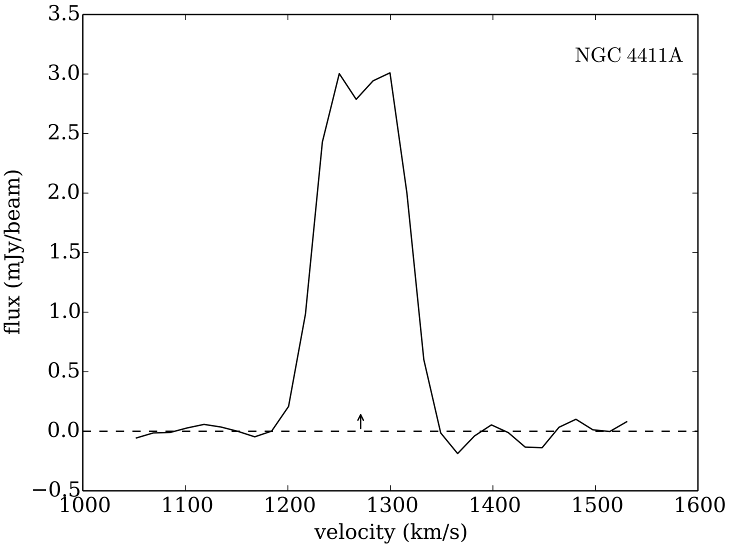

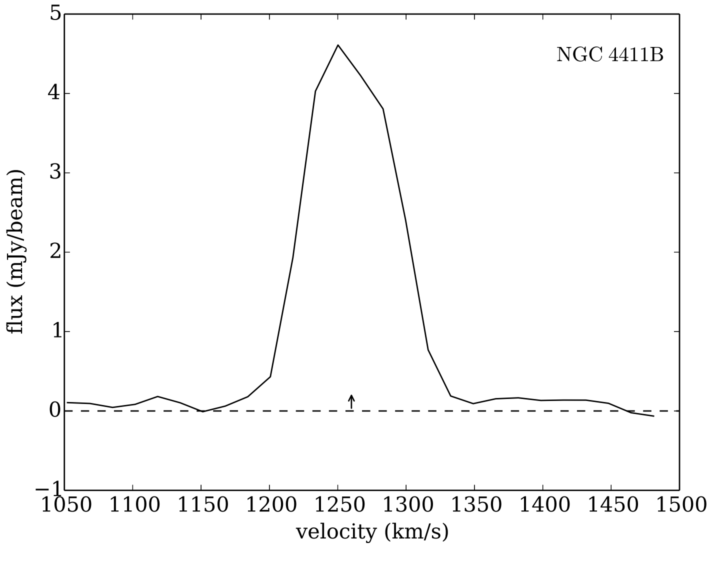

Figure A.6: **NGC 4411 A&B:**. Contours: 1, 5, 10, 15, 20 $\times 10^{19}$ atoms cm^{-2}. NGC 4411A: $v_{\rm sys} = 1271\,{\rm km\,s^{-1}}$. NGC 4411A: $v_{\rm sys} = 1260\,{\rm km\,s^{-1}}$

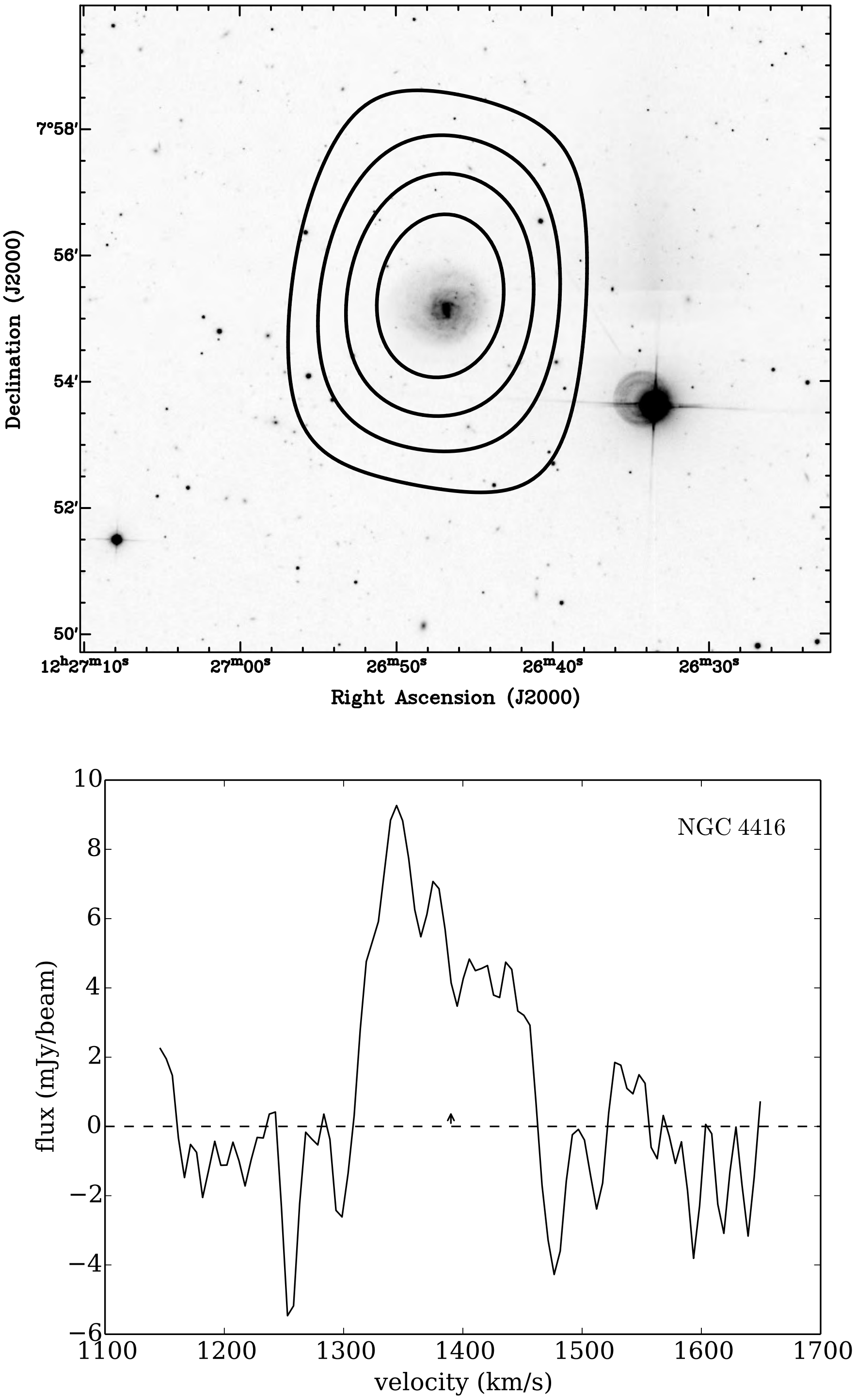

Figure A.7: **NGC 4416**. Contours: 0.5, 1.0, 1.5, 2.0 $\times 10^{19}$ atoms cm^{-2}. $v_{\mathrm{sys}} = 1390\,\mathrm{km\,s^{-1}}$.

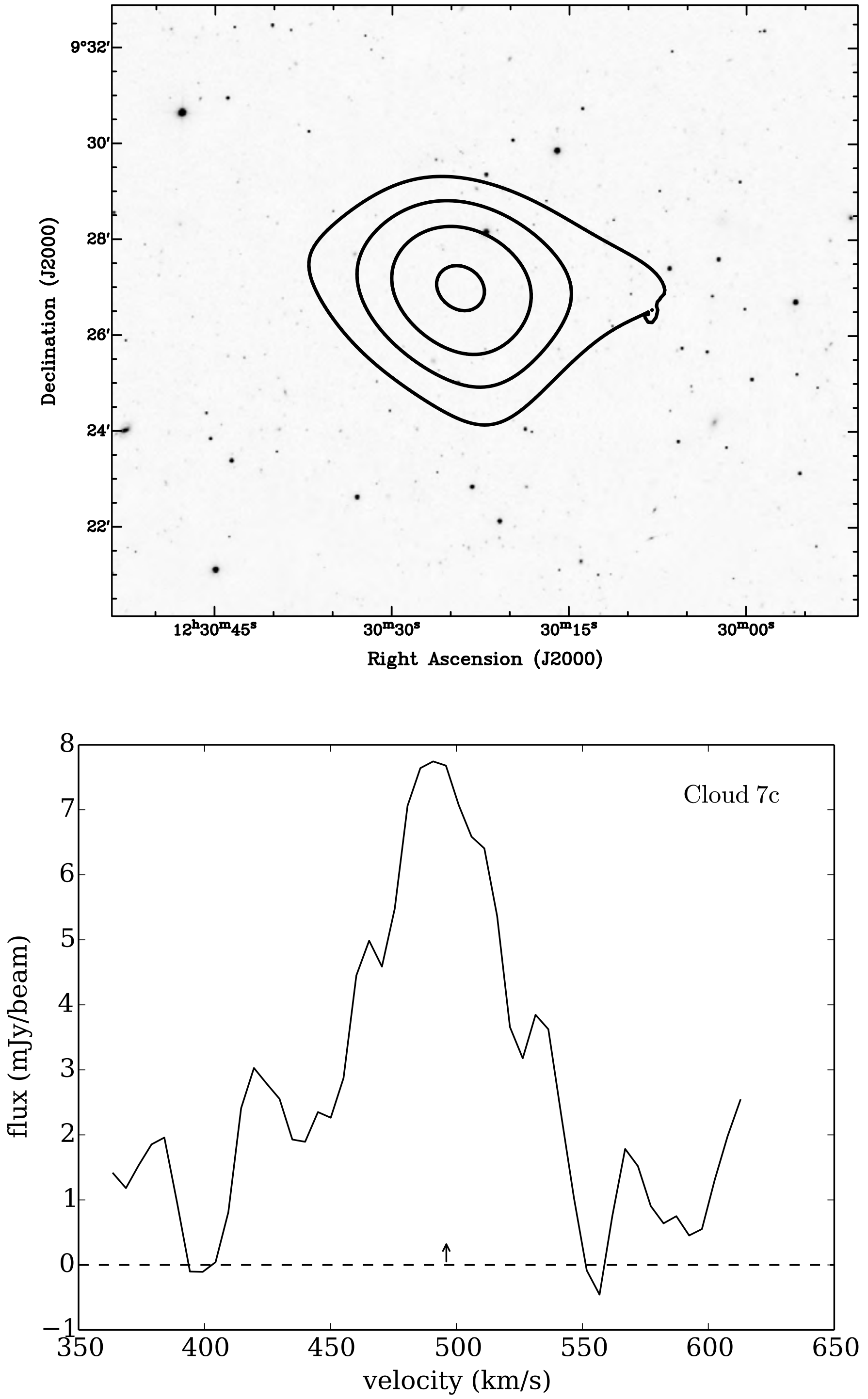

Figure A.8: **Cloud 7c**. Contours: 0.5, 1.0, 1.5, 2.0 $\times 10^{19}$ atoms cm^{-2}. $v_{\rm sys} = 496\,{\rm km\,s^{-1}}$.

Bibliography

Allamandola, L. J., Tielens, A. G. G. M., & Barker, J. R. 1985, Astrophys. J., 290, L25

Allamandola, L. J., Tielens, G. G. M., & Barker, J. R. 1989, Astrophys. J. Suppl. Ser., 71, 733

Alpaslan, M., Robotham, A. S. G., Driver, S., Norberg, P., Baldry, I., Bauer, A. E., Bland-Hawthorn, J., Brown, M., Cluver, M., Colless, M., Foster, C., Hopkins, A., Van Kampen, E., Kelvin, L., Lara-Lopez, M. A., Liske, J., Lopez-Sanchez, A. R., Loveday, J., McNaught-Roberts, T., Merson, A., & Pimbblet, K. 2013, Mon. Not. R. Astron. Soc., 438, 177

Arnaud, M., Pointecouteau, E., & Pratt, G. W. 2005, Astron. Astrophys., 441, 893

Bahe, Y. M., McCarthy, I. G., Balogh, M. L., & Font, A. S. 2013, Mon. Not. R. Astron. Soc., 430, 3017

Balogh, M. L., Morris, S. L., Yee, H. K. C., Carlberg, R. G., & Ellingson, E. 1997, Astrophys. J., 488, L75

Balogh, M. L., Navarro, J. F., & Morris, S. L. 2000, Astrophys. J., 540, 113

Bauer, A. E., Drory, N., Hill, G. J., & Feulner, G. 2005, Astrophys. J., 621, L89

Bekki, K. 2013, Mon. Not. R. Astron. Soc., 438, 444

Benson, A. J. 2005, Mon. Not. R. Astron. Soc., 358, 551

Binggeli, B., Popescu, C. C., & Tammann, G. A. 1993, Astron. Astrophys. Suppl. Ser., 98, 275

Binggeli, B., Sandage, A., & Tammann, G. A. 1985, Astron. J., 90, 1681

Binggeli, B., Tammann, G. A., & Sandage, A. 1987, Astron. J., 94, 251

Böhringer, H., Briel, U. G., Schwarz, R. A., Voges, W., Hartner, G., & Trümper, J. 1994, Nature, 368, 828

Bond, J. R., Kofman, L., & Pogosyan, D. 1996, Nature, 380, 603

Boselli, A. & Gavazzi, G. 2006, Publ. Astron. Soc. Pacific, 118, 517

Bothun, G. D., Sullivan, W. T., I., & Schommer, R. A. 1982, Astron. J., 87, 725

Bottinelli, L. & Gouguenheim, L. 1974, Astron. Astrophys., 36, 461

Boylan-Kolchin, M., Springel, V., White, S. D. M., Jenkins, A., & Lemson, G. 2009, Mon. Not. R. Astron. Soc., 398, 1150

Braun, R. & Thilker, D. A. 2004, Astron. Astrophys., 435, 421

Briggs, D. S. 1995, Am. Astron. Soc., 27

Briggs, F. H., Wolfe, A. M., Krumm, N., & Salpeter, E. E. 1980, Astrophys. J., 238, 510

Calzetti, D. 2013, Star Formation Rate Indicators

Calzetti, D., Kennicutt, R. C., Engelbracht, C. W., Leitherer, C., Draine, B. T., Kewley, L., Moustakas, J., Sosey, M., Dale, D. A., Gordon, K. D., Helou, G. X., Hollenbach, D. J., Armus, L., Bendo, G., Bot, C., Buckalew, B., Jarrett, T., Li, A., Meyer, M., Murphy, E. J., Prescott, M., Regan, M. W., Rieke, G. H., Roussel, H., Sheth, K., Smith, J. D. T., Thornley, M. D., & Walter, F. 2007, Astrophys. J., 666, 870

Calzetti, D., Wu, S.-Y., Hong, S., Kennicutt, R. C., Lee, J. C., Dale, D. A., Engelbracht, C. W., van Zee, L., Draine, B. T., Hao, C.-N., Gordon, K. D., Moustakas, J., Murphy, E. J., Regan, M., Begum, A., Block, M., Dalcanton, J., Funes, J., Gil de Paz, A., Johnson, B., Sakai, S., Skillman, E., Walter, F., Weisz, D., Williams, B., & Wu, Y. 2010, Astrophys. J., 714, 1256

Cantalupo, S., Arrigoni-Battaia, F., Prochaska, J. X., Hennawi, J. F., & Madau, P. 2014, Nature, 506, 63

Carignan, C., Frank, B. S., Hess, K. M., Lucero, D. M., Randriamampandry, T. H., Goedhart, S., & Passmoor, S. S. 2013, Astron. J., 146, 48

Catinella, B., Schiminovich, D., Cortese, L., Fabello, S., Hummels, C. B., Moran, S. M., Lemonias, J. J., Cooper, A. P., Wu, R., Heckman, T. M., & Wang, J. 2013, Mon. Not. R. Astron. Soc., 436, 34

Cautun, M., van de Weygaert, R., Jones, B. J. T., & Frenk, C. S. 2014, Mon. Not. R. Astron. Soc., 441, 2923

Cayatte, V., Balkowski, C., van Gorkom, J. H., & Kotanyi, C. 1990, Astron. J., 100, 604

Cen, R., Kang, H., Ostriker, J. P., & Ryu, D. 1995, Astrophys. J., 451, 436

Cen, R. & Ostriker, J. P. 1999, Astrophys. J., 514, 1

Chamaraux, P., Balkowski, C., & Gerard, E. 1980, Astron. Astrophys., 83, 38

Chengalur, J. N., Salpeter, E. E., & Terzian, Y. 1993, Astrophys. J., 419, 30

Chin, D. & O'Neil, K. 2000, Am. Astron. Soc., 32

Chung, A., van Gorkom, J. H., Kenney, J. D. P., Crowl, H., & Vollmer, B. 2009, Astron. J., 138, 1741

Chung, A., van Gorkom, J. H., Kenney, J. D. P., & Vollmer, B. 2007, Astrophys. J., 659, L115

Clemens, M. S., Alexander, P., & Green, D. A. 1998, Mon. Not. R. Astron. Soc., 297, 1015

Cluver, M. E., Jarrett, T. H., Hopkins, A. M., Driver, S. P., Liske, J., Gunawardhana, M. L. P., Taylor, E. N., Robotham, A. S. G., Alpaslan, M., Baldry, I., Brown, M. J. I., Peacock, J. A., Popescu, C. C., Tuffs, R. J., Bauer, A. E., Bland-Hawthorn, J., Colless, M., Holwerda, B. W., Lara-López, M. A., Leschinski, K., López-Sánchez, A. R., Norberg, P., Owers, M. S., Wang, L., & Wilkins, S. M. 2014, Astrophys. J., 782, 90

Cluver, M. E., Jarrett, T. H., Kraan-Korteweg, R. C., Koribalski, B. S., Appleton, P. N., Melbourne, J., Emonts, B., & Woudt, P. A. 2010, Astrophys. J., 725, 1550

Colless, M., Dalton, G., Maddox, S., Sutherland, W., Norberg, P., Cole, S., Bland-Hawthorn, J., Bridges, T., Cannon, R., Collins, C., Couch, W., Cross, N., Deeley, K., De Propris, R., Driver, S. P., Efstathiou, G., Ellis, R. S., Frenk, C. S., Glazebrook, K., Jackson, C., Lahav, O., Lewis, I., Lumsden, S., Madgwick, D., Peacock, J. A., Peterson, B. A., Price, I., Seaborne, M., & Taylor, K. 2001, Mon. Not. R. Astron. Soc., 328, 1039

Cornwell, T. 1995, Very Long Baseline Interferom. VLBANRAO Work. No. 22, 82

Cortés, J. R., Kenney, J. D. P., & Hardy, E. 2006, Astron. J., 131, 747

—. 2008, Astrophys. J., 683, 78

Cortese, L., Gavazzi, G., Boselli, A., Franzetti, P., Kennicutt, R. C., O'Neil, K., & Sakai, S. 2006, Astron. Astrophys., 453, 847

Crook, A. C., Huchra, J. P., Martimbeau, N., Masters, K. L., Jarrett, T., & Macri, L. M. 2007, Astrophys. J., 655, 790

Crowl, H. & Kenney, J. 2005, Astron. . . . , 1, 65

Dahlem, M., Ehle, M., Ryder, S. D., Vlajić, M., & Haynes, R. F. 2005, Astron. Astrophys., 432, 475

Dale, D. A., Giovanelli, R., Haynes, M. P., Scodeggio, M., Hardy, E., & Campusano, L. E. 1998, Astron. J., 115, 418

Dale, D. A., Smith, J. D. T., Schlawin, E. A., Armus, L., Buckalew, B. A., Cohen, S. A., Helou, G., Jarrett, T. H., Johnson, L. C., Moustakas, J., Murphy, E. J., Roussel, H., Sheth, K., Staudaher, S., Bot, C., Calzetti, D., Engelbracht, C. W., Gordon, K. D., Hollenbach, D. J., Kennicutt, R. C., & Malhotra, S. 2009, Astrophys. J., 693, 1821

Danforth, C. W. & Shull, J. M. 2008, Astrophys. J., 679, 194

Davé, R., Cen, R., Ostriker, J. P., Bryan, G. L., Hernquist, L., Katz, N., Weinberg, D. H., Norman, M. L., & O'Shea, B. 2001, Astrophys. J., 552, 473

Davé, R., Hernquist, L., Katz, N., & Weinberg, D. H. 1999, Astrophys. J., 511, 521

Davies, R. D. & Lewis, B. M. 1973, Mon. Not. R. Astron. Soc., 165, 231

Dawson, K. S., Schlegel, D. J., Ahn, C. P., Anderson, S. F., Aubourg, E., Bailey, S., Barkhouser, R. H., Bautista, J. E., Beifiori, A., Berlind, A. A., Bhardwaj, V., Bizyaev, D., Blake, C. H., Blanton, M. R., Blomqvist, M., Bolton, A. S., Borde, A., Bovy, J., Brandt, W. N., Brewington, H., Brinkmann, J., Brown, P. J., Brownstein, J. R., Bundy, K., Busca, N. G., Carithers, W., Carnero, A. R., Carr, M. A., Chen, Y., Comparat, J., Connolly, N., Cope, F., Croft, R. A. C., Cuesta, A. J., da Costa, L. N., Davenport, J. R. A., Delubac, T., de Putter, R., Dhital, S., Ealet, A., Ebelke, G. L., Eisenstein, D. J., Escoffier, S., Fan, X., Filiz Ak, N., Finley, H., Font-Ribera, A., Génova-Santos, R., Gunn, J. E., Guo, H., Haggard, D., Hall, P. B., Hamilton, J.-C., Harris, B., Harris, D. W., Ho, S., Hogg, D. W., Holder, D., Honscheid, K., Huehnerhoff, J., Jordan, B., Jordan, W. P., Kauffmann, G., Kazin, E. A., Kirkby, D., Klaene, M. A., Kneib, J.-P., Le Goff, J.-M., Lee, K.-G., Long, D. C., Loomis, C. P., Lundgren, B., Lupton, R. H., Maia, M. A. G., Makler, M., Malanushenko, E., Malanushenko, V., Mandelbaum, R., Manera, M., Maraston, C., Margala, D., Masters, K. L., McBride, C. K., McDonald, P., McGreer, I. D., McMahon, R. G., Mena, O., Miralda-Escudé, J., Montero-Dorta, A. D., Montesano, F., Muna, D., Myers, A. D., Naugle, T., Nichol, R. C., Noterdaeme, P., Nuza, S. E., Olmstead, M. D., Oravetz, A., Oravetz, D. J., Owen, R., Padmanabhan, N., Palanque-Delabrouille, N., Pan, K., Parejko, J. K., Pâris, I., Percival, W. J., Pérez-Fournon, I., Pérez-Ràfols, I., Petitjean, P., Pfaffenberger, R., Pforr, J., Pieri, M. M., Prada, F., Price-Whelan, A. M., Raddick, M. J., Rebolo, R., Rich, J., Richards, G. T., Rockosi, C. M., Roe, N. A., Ross, A. J., Ross, N. P., Rossi, G., Rubiño Martin, J. A., Samushia, L., Sánchez, A. G., Sayres, C., Schmidt, S. J., Schneider, D. P., Scóccola, C. G., Seo, H.-J., Shelden, A., Sheldon, E., Shen, Y., Shu, Y., Slosar, A., Smee, S. A., Snedden, S. A., Stauffer, F., Steele, O., Strauss, M. A., Streblyanska, A., Suzuki, N., Swanson, M. E. C., Tal, T., Tanaka, M., Thomas, D., Tinker, J. L., Tojeiro, R., Tremonti, C. A., Vargas Magaña, M., Verde, L., Viel, M., Wake, D. A., Watson, M., Weaver, B. A., Weinberg, D. H., Weiner, B. J., West, A. A., White, M., Wood-Vasey, W. M., Yeche, C., Zehavi, I., Zhao, G.-B., & Zheng, Z. 2013, Astron. J., 145, 10

De Lucia, G., Weinmann, S., Poggianti, B. M., Aragón-Salamanca, A., & Zaritsky, D. 2012, Mon. Not. R. Astron. Soc., 423, 1277

de Vaucouleurs, G., de Vaucouleurs, A., Corwin, H. G., J., Buta, R. J., Paturel, G., & Fouqué, P. 1991, Sky Telescope, 82

Donas, J. & Deharveng, J. M. 1984, Astron. Astrophys., 140, 325

Dove, J. B. & Shull, J. M. 1994, Astrophys. J., 423, 196

Draine, B. 2003, Annu. Rev. Astron. Astrophys., 41, 241

Dressler, A. 1980, Astrophys. J., 236, 351

Duc, P.-A., Belles, P.-E., Brinks, E., & Bournaud, F. 2013, Proc. Int. Astron. Union, 8, 323

Eggen, O. J., Lynden-Bell, D., & Sandage, A. R. 1962, Astrophys. J., 136, 748

Eke, V. R., Baugh, C. M., Cole, S., Frenk, C. S., Norberg, P., Peacock, J. A., Baldry, I. K., Bland-Hawthorn, J., Bridges, T., Cannon, R., Colless, M., Collins, C., Couch, W., Dalton, G., Propris, R. D., Driver, S. P., Efstathiou, G., Ellis, R. S., Glazebrook, K., Jackson, C., Lahav, O., Lewis, I., Lumsden, S., Maddox, S., Madgwick, D., Peterson, B. A., Sutherland, W., & Taylor, K. 2004, Mon. Not. R. Astron. Soc., 348, 866

Ewen, H. I. & Purcell, E. M. 1951, Nature, 168, 356

Fadda, D., Biviano, A., Marleau, F. R., Storrie-Lombardi, L. J., & Durret, F. 2008, Astrophys. J., 672, L9

Fang, T., Croft, R. A. C., Sanders, W. T., Houck, J., Davé, R., Katz, N., Weinberg, D. H., & Hernquist, L. 2005, Astrophys. J., 623, 612

Fang, T., Marshall, H. L., Lee, J. C., Davis, D. S., & Canizares, C. R. 2002, Astrophys. J., 572, L127

Farrah, D., Bernard-Salas, J., Spoon, H. W. W., Soifer, B. T., Armus, L., Brandl, B., Charmandaris, V., Desai, V., Higdon, S., Devost, D., & Houck, J. 2007, Astrophys. J., 667, 149

Fernández, X., van Gorkom, J. H., Hess, K. M., Pisano, D. J., Kreckel, K., Momjian, E., Popping, A., Oosterloo, T., Chomiuk, L., Verheijen, M. A. W., Henning, P. A., Schiminovich, D., Bershady, M. A., Wilcots, E. M., & Scoville, N. 2013, Astrophys. J., 770, L29

Fouqué, P., Bottinelli, L., Gouguenheim, L., & Paturel, G. 1990, Astrophys. J., 349, 1

Fouqué, P., Solanes, J. M., Sanchis, T., & Balkowski, C. 2001, Astron. Astrophys., 375, 770

Freeland, E., Stilp, A., & Wilcots, E. 2009, Astron. J., 138, 295

Fujita, Y. 2004, Publ. Astron. Soc. Japan, 56, 29

Fujita, Y. & Nagashima, M. 1999, Astrophys. J., 516, 619

Fukugita, M., Hogan, C. J., & Peebles, P. J. E. 1998, Astrophys. J., 503, 518

Fukugita, M. & Peebles, P. J. E. 2004, Astrophys. J., 616, 643

Galametz, M., Kennicutt, R. C., Calzetti, D., Aniano, G., Draine, B. T., Boquien, M., Brandl, B., Croxall, K. V., Dale, D. A., Engelbracht, C. W., Gordon, K. D., Groves, B., Hao, C.-N., Helou, G., Hinz, J. L., Hunt, L. K., Johnson, B. D., Li, Y., Murphy, E., Roussel, H., Sandstrom, K., Skibba, R. A., & Tabatabaei, F. S. 2013, Mon. Not. R. Astron. Soc., 431, 1956

Galliano, F., Madden, S. C., Tielens, A. G. G. M., Peeters, E., & Jones, A. P. 2008, Astrophys. J., 679, 310

Gavazzi, G., Boselli, A., Donati, A., Franzetti, P., & Scodeggio, M. 2003, Astron. Astrophys., 400, 451

Geller, M. J. & Huchra, J. P. 1983, Astrophys. J. Suppl. Ser., 52, 61

Giovanelli, R. & Haynes, M. P. 1985, Astrophys. J., 292, 404

—. 1988, Galact. Extragalactic Radio Astron., -1, 522

Giovanelli, R., Haynes, M. P., Salzer, J. J., Wegner, G., da Costa, L. N., & Freudling, W. 1994, Astron. J., 107, 2036

Giuricin, G., Marinoni, C., Ceriani, L., & Pisani, A. 2000, Astrophys. J., 543, 178

Gomez, P. L., Nichol, R. C., Miller, C. J., Balogh, M. L., Goto, T., Zabludoff, A. I., Romer, A. K., Bernardi, M., Sheth, R., Hopkins, A. M., Castander, F. J., Connolly, A. J., Schneider, D. P., Brinkmann, J., Lamb, D. Q., SubbaRao, M., & York, D. G. 2003, Astrophys. J., 584, 210

Gunn, J. E. & Gott, J. Richard, I. 1972, Astrophys. J., 176, 1

Haynes, M. P. & Giovanelli, R. 1986, Astrophys. J., 306, 466

Haynes, M. P., Giovanelli, R., Chamaraux, P., da Costa, L. N., Freudling, W., Salzer, J. J., & Wegner, G. 1999, Astron. J., 117, 2039

Haynes, M. P., Giovanelli, R., & Chincarini, G. L. 1984a, Annu. Rev. Astron. Astrophys., 22, 445

—. 1984b, Annu. Rev. Astron. Astrophys., 22, 445

Haynes, M. P., Giovanelli, R., Martin, A. M., Hess, K. M., Adams, E. A. K., Hallenbeck, G., Hoffman, G. L., Huang, S., Kent, B. R., Koopmann, R. A., Papastergis, E., Stierwalt, S., Balonek, T. J., Craig, D. W., Higdon, S. J. U., Kornreich, D. A., Miller, J. R., Donoghue, A. A. O., & Olowin, R. P. 2011, Astron. J., 170

Heald, G., Józsa, G., Serra, P., Zschaechner, L., Rand, R., Fraternali, F., Oosterloo, T., Walterbos, R., Jütte, E., & Gentile, G. 2011, Astron. Astrophys., 526, A118

Hess, K. M. & Wilcots, E. M. 2013, Astron. J., 146, 124

Högbom, J. A. 1974, Astron. Astrophys. Suppl., 15

Hollenbach, D. J. & Tielens, A. G. G. M. 1997, Annu. Rev. Astron. Astrophys., 35, 179

Hubble, E. & Humason, M. L. 1931, Astrophys. J., 74, 43

Huchra, J., Jarrett, T., Skrutskie, M., Cutri, R., Schneider, S., Macri, L., Steining, R., Mader, J., Martimbeau, N., & George, T. 2005, Nearby Large-Scale Struct. Zo. Avoid. ASP Conf. Ser., 329

Jarrett, T. H., Chester, T., Cutri, R., Schneider, S., Skrutskie, M., & Huchra, J. P. 2000, Astron. J., 119, 2498

Jarrett, T. H., Cohen, M., Masci, F., Wright, E., Stern, D., Benford, D., Blain, A., Carey, S., Cutri, R. M., Eisenhardt, P., Lonsdale, C., Mainzer, A., Marsh, K., Padgett, D., Petty, S., Ressler, M., Skrutskie, M., Stanford, S., Surace, J., Tsai, C. W., Wheelock, S., & Yan, D. L. 2011, Astrophys. J., 735, 112

Jenkins, A., Frenk, C. S., Pearce, F. R., Thomas, P. A., Colberg, J. M., White, S. D. M., Couchman, H. M. P., Peacock, J. A., Efstathiou, G., & Nelson, A. H. 1998, Astrophys. J., 499, 20

Kauffmann, G., White, S. D. M., Heckman, T. M., Ménard, B., Brinchmann, J., Charlot, S., Tremonti, C., & Brinkmann, J. 2004, Mon. Not. R. Astron. Soc., 353, 713

Kawata, D. & Mulchaey, J. S. 2008, Astrophys. J., 672, L103

Kenney, J. D. P., Crowl, H., van Gorkom, J., & Vollmer, B. 2004, Int. Astron. Union Symp. no. 217

Kenney, J. D. P., Koopmann, R. A., Rubin, V. C., & Young, J. S. 1996, Astron. J., 111, 152

Kennicutt, R. C. 1998, Annu. Rev. Astron. Astrophys., 36, 189

Kennicutt, R. C. & Evans, N. J. 2012, Annu. Rev. Astron. Astrophys., 50, 531

Kennicutt, Jr., R. C. 1998, Astrophys. J., 498, 541

Kennicutt, Jr., R. C., Armus, L., Bendo, G., Calzetti, D., Dale, D. A., Draine, B. T., Engelbracht, C. W., Gordon, K. D., Grauer, A. D., Helou, G., Hollenbach, D. J., Jarrett, T. H., Kewley, L. J., Leitherer, C., Li, A., Malhotra, S., Regan, M. W., Rieke, G. H., Rieke, M. J., Roussel, H., Smith, J. T., Thornley, M. D., & Walter, F. 2003, Publ. Astron. Soc. Pacific, 115, 928

Kilborn, V. A., Forbes, D. A., Barnes, D. G., Koribalski, B. A. S., Brough, S., & Kern, K. 2009, Mon. Not. R. Astron. Soc., 400, 1962

Koopmann, R. A. & Kenney, J. D. P. 2004, Astrophys. J., 613, 866

Larson, R. B., Tinsley, B. M., & Caldwell, C. N. 1980, Astrophys. J., 237, 692

Lee, J. C., Hwang, H. S., & Ko, J. 2013, Astrophys. J., 774, 62

Leger, A. & Puget, J. L. 1984, Astron. Astrophys. (ISSN 0004-6361), 137

Lewis, B. M. 1987, Astrophys. J. Suppl. Ser., 63, 515

Lewis, I., Balogh, M., De Propris, R., Couch, W., Bower, R., Offer, A., Bland-Hawthorn, J., Baldry, I. K., Baugh, C., Bridges, T., Cannon, R., Cole, S., Colless, M., Collins, C., Cross, N., Dalton, G., Driver, S. P., Efstathiou, G., Ellis, R. S., Frenk, C. S., Glazebrook, K., Hawkins, E., Jackson, C., Lahav, O., Lumsden, S., Maddox, S., Madgwick, D., Norberg, P., Peacock, J. A., Percival, W., Peterson, B. A., Sutherland, W., & Taylor, K. 2002, Mon. Not. R. Astron. Soc., 334, 673

Mahajan, S. 2011, Am. Astron. Soc., 43

—. 2013, Mon. Not. R. Astron. Soc. Lett., 431, L117

Mamon, G. A. 2007, in Groups of Galaxies in the Nearby Universe, ed. I. Saviane, V. D. Ivanov, & J. Borissova, ESO ASTROPHYSICS SYMPOSIA (Berlin, Heidelberg: Springer Berlin Heidelberg), 203

Masters, K. L., Crook, A., Hong, T., Jarrett, T. H., Koribalski, B. S., Macri, L., Springob, C. M., & Staveley-Smith, L. 2014a, Mon. Not. R. Astron. Soc., 443, 1044

Masters, K. L., Giovanelli, R., & Haynes, M. P. 2003, Astron. J., 126, 158

Masters, K. L., Springob, C. M., & Huchra, J. P. 2014b, Astron. J., 147, 124

McCarthy, I. G., Frenk, C. S., Font, A. S., Lacey, C. G., Bower, R. G., Mitchell, N. L., Balogh, M. L., & Theuns, T. 2008, Mon. Not. R. Astron. Soc., 383, 593

Meyer, M. J., Zwaan, M. A., Webster, R. L., Staveley-Smith, L., Ryan-Weber, E., Drinkwater, M. J., Barnes, D. G., Howlett, M., Kilborn, V. A., Stevens, J., Waugh, M., Pierce, M. J., Bhathal, R., de Blok, W. J. G., Disney, M. J., Ekers, R. D., Freeman, K. C., Garcia, D. A., Gibson, B. K., Harnett, J., Henning, P. A., Jerjen, H., Kesteven, M. J., Knezek, P. M., Koribalski, B. S., Mader, S., Marquarding, M., Minchin, R. F., O'Brien, J., Oosterloo, T., Price, R. M., Putman, M. E., Ryder, S. D., Sadler, E. M., Stewart, I. M., Stootman, F., & Wright, A. E. 2004, Mon. Not. R. Astron. Soc., 350, 1195

Mihos, J. C. & Hernquist, L. 1996, Astrophys. J., 464, 641

Molinari, S., Swinyard, B., Bally, J., Barlow, M., Bernard, J.-P., Martin, P., Moore, T., Noriega-Crespo, A., Plume, R., Testi, L., Zavagno, A., Abergel, A., Ali, B., Anderson, L., André, P., Baluteau, J.-P., Battersby, C., Beltrán, M. T., Benedettini, M., Billot, N., Blommaert, J., Bontemps, S., Boulanger, F., Brand, J., Brunt, C., Burton, M., Calzoletti, L., Carey, S., Caselli, P., Cesaroni, R., Cernicharo, J., Chakrabarti, S., Chrysostomou, A., Cohen, M., Compiegne, M., de Bernardis, P., de Gasperis, G., di Giorgio, A. M., Elia, D., Faustini, F., Flagey, N., Fukui, Y., Fuller, G. A., Ganga, K., Garcia-Lario, P., Glenn, J., Goldsmith, P. F., Griffin, M., Hoare, M., Huang, M., Ikhenaode, D., Joblin, C., Joncas, G., Juvela, M., Kirk, J. M., Lagache, G., Li, J. Z., Lim, T. L., Lord, S. D., Marengo, M., Marshall, D. J., Masi, S., Massi, F., Matsuura, M., Minier, V., Miville-Deschênes, M.-A., Montier, L. A., Morgan, L., Motte, F., Mottram, J. C., Müller, T. G., Natoli, P., Neves, J., Olmi, L., Paladini, R., Paradis, D., Parsons, H., Peretto, N., Pestalozzi, M., Pezzuto, S., Piacentini, F., Piazzo, L., Polychroni, D., Pomarès, M., Popescu, C. C., Reach, W. T., Ristorcelli, I., Robitaille, J.-F., Robitaille, T., Rodón, J. A., Roy, A., Royer, P., Russeil, D., Saraceno, P., Sauvage, M., Schilke, P., Schisano, E., Schneider, N., Schuller, F., Schulz, B., Sibthorpe, B., Smith, H. A., Smith, M. D., Spinoglio, L., Stamatellos, D., Strafella, F., Stringfellow, G. S., Sturm, E., Taylor, R., Thompson, M. A., Traficante, A., Tuffs, R. J., Umana, G., Valenziano, L., Vavrek, R., Veneziani, M., Viti, S., Waelkens, C., Ward-Thompson, D., White, G., Wilcock, L. A., Wyrowski, F., Yorke, H. W., & Zhang, Q. 2010, Astron. Astrophys., 518, L100

Moore, B., Katz, N., Lake, G., Dressler, A., & Oemler, A. 1996, Nature, 379, 613

Moore, B., Lake, G., & Katz, N. 1998, Astrophys. J., 495, 139

Nicastro, F., Elvis, M., Fiore, F., & Mathur, S. 2005, Adv. Sp. Res., 36, 721

Nilson, P. 1973, Acta Univ. Ups. Nov. Acta Regiae Soc. Sci. Ups. - Uppsala Astron. Obs. Ann.

Peeters, E., Allamandola, L. J., Hudgins, D. M., Hony, S., & Tielens, A. G. G. M. 2004a, Astrophys. Dust, 309

Peeters, E., Spoon, H. W. W., & Tielens, A. G. G. M. 2004b, Astrophys. J., 613, 986

Perez-Gonzalez, P. G., Gil de Paz, A., Zamorano, J., Gallego, J., Alonso-Herrero, A., & Aragon-Salamanca, A. 2003, Mon. Not. R. Astron. Soc., 338, 525

Perley, R. A. & Butler, B. J. 2013, Astrophys. J. Suppl. Ser., 204, 19

Péroux, C., McMahon, R. G., Storrie-Lombardi, L. J., & Irwin, M. J. 2003, Mon. Not. R. Astron. Soc., 346, 1103

Persic, M. & Salucci, P. 1992, Mon. Not. R. Astron. Soc. (ISSN 0035-8711), 258

Pimbblet, K. A., Drinkwater, M. J., & Hawkrigg, M. C. 2004, Mon. Not. R. Astron. Soc., 354, L61

Pisano, D. J., Barnes, D. G., Gibson, B. K., Staveley-Smith, L., Freeman, K. C., & Kilborn, V. A. 2007, Astrophys. J., 662, 959

Pisano, D. J., Barnes, D. G., Staveley-Smith, L., Gibson, B. K., Kilborn, V. A., & Freeman, K. C. 2011, Astrophys. J. Suppl. Ser., 197, 28

Porter, S. C., Raychaudhury, S., Pimbblet, K. A., & Drinkwater, M. J. 2008, Mon. Not. R. Astron. Soc., 388, 1152

Rasmussen, J., Mulchaey, J. S., Bai, L., Ponman, T. J., Raychaudhury, S., & Dariush, A. 2012, Astrophys. J., 757, 122

Raychaudhury, S. & Porter, S. C. 2005, Am. Astron. Soc. Meet. 207, 37

Rieke, G. H., Alonso-Herrero, A., Weiner, B. J., Pérez-González, P. G., Blaylock, M., Donley, J. L., & Marcillac, D. 2009, Astrophys. J., 692, 556

Rubin, V. C., Waterman, A. H., & Kenney, J. D. P. 1999, Astron. J., 118, 236

Safonova, E. S. 2011, Astron. Reports, 55, 1016

Sancisi, R., Thonnard, N., & Ekers, R. D. 1987, Astrophys. J., 315, L39

Sandage, A., Binggeli, B., & Tammann, G. A. 1985, Astron. J., 90, 395

Sauvage, M., Tuffs, R. J., & Popescu, C. C. 2005, Space Sci. Rev., 119, 313

Schlafly, E. F. & Finkbeiner, D. P. 2011, Astrophys. J., 737, 103

Schlegel, D. J., Finkbeiner, D. P., & Davis, M. 1998, Astrophys. J., 500, 525

Schneider, S. E., Helou, G., Salpeter, E. E., & Terzian, Y. 1986, Astron. J. (ISSN 0004-6256), 92, 742

Scoville, N. Z., Polletta, M., Ewald, S., Stolovy, S. R., Thompson, R., & Rieke, M. 2001, Astron. J., 122, 3017

Silk, J. & Sunyaev, R. A. 1976, Nature, 260, 508

Solanes, J. M., Giovanelli, R., & Haynes, M. P. 1996, Astrophys. J., 461, 609

Solanes, J. M., Sanchis, T., Salvador-Solé, E., Giovanelli, R., & Haynes, M. P. 2002, Astron. J., 124, 2440

Springel, V., White, S. D. M., Jenkins, A., Frenk, C. S., Yoshida, N., Gao, L., Navarro, J., Thacker, R., Croton, D., Helly, J., Peacock, J. A., Cole, S., Thomas, P., Couchman, H., Evrard, A., Colberg, J., & Pearce, F. 2005, Nature, 435, 629

Springob, C. M., Haynes, M. P., Giovanelli, R., & Kent, B. R. 2005, Astrophys. J. Suppl. Ser., 160, 149

Springob, C. M., Masters, K. L., Haynes, M. P., Giovanelli, R., & Marinoni, C. 2009, Astrophys. J. Suppl. Ser., 182, 474

Sramek, R. A. & Schwab, F. R. 1989, Synth. imaging radio Astron., 6

Stanimirovič, S. 1999, Ph.D. thesis

Theureau, G., Hanski, M. O., Coudreau, N., Hallet, N., & Martin, J.-M. 2007, Astron. Astrophys., 465, 71

Tonnesen, S., Bryan, G. L., & van Gorkom, J. H. 2007, Astrophys. J., 671, 1434

Toomre, A. & Toomre, J. 1972, Astrophys. J., 178, 623

Tripp, T. M., Savage, B. D., & Jenkins, E. B. 2000, Astrophys. J., 534, L1

Tully, R. B. & Fisher, J. R. 1977, Astron. Astrophys., 54, 661

Tully, R. B. & Fouqué, P. 1985, Astrophys. J. Suppl. Ser., 58, 67

Tully, R. B. & Shaya, E. J. 1984, Astrophys. J., 281, 31

Tully, R. B., Shaya, E. J., Karachentsev, I. D., Courtois, H. M., Kocevski, D. D., Rizzi, L., & Peel, A. 2008, Astrophys. J., 676, 184

Urban, O., Werner, N., Simionescu, A., Allen, S. W., & Böhringer, H. 2011, Mon. Not. R. Astron. Soc., 414, 2101

van de Hulst, H. C. 1945, Ned. Tijdschr. voor Natuurkd. (in Dutch; Repr. Sullivan III, Pap. 34), 11, 210

van de Weygaert, R. & Bond, J. R. 2008, A Pan-Chromatic View Clust. Galaxies Large-Scale Struct., 740

van Gorkom, J. 1991, Atoms, 16

Verheijen, M. A. W. & Sancisi, R. 2001, Astron. Astrophys., 370, 765

Vijayaraghavan, R. & Ricker, P. M. 2013, Mon. Not. R. Astron. Soc., 435, 2713

Vollmer, B., Beck, R., Kenney, J. D. P., & van Gorkom, J. H. 2004, Astron. J., 127, 3375

Vollmer, B., Cayatte, V., Balkowski, C., & Duschl, W. J. 2001, Astrophys. J., 561, 708

Walter, F., Brinks, E., de Blok, W. J. G., Bigiel, F., Kennicutt, R. C., Thornley, M. D., & Leroy, A. 2008, Astron. J., 136, 2563

Wang, J., Kauffmann, G., Jozsa, G. I. G., Serra, P., van der Hulst, T., Bigiel, F., Brinchmann, J., Verheijen, M. A. W., Oosterloo, T., Wang, E., Li, C., den Heijer, M., & Kerp, J. 2013, Mon. Not. R. Astron. Soc., 433, 270

Warmels, R. H. 1988, Astron. Astrophys. Suppl. Ser. (ISSN 0365-0138), 72, 19

Werner, M. W., Roellig, T. L., Low, F. J., Rieke, G. H., Rieke, M., Hoffmann, W. F., Young, E., Houck, J. R., Brandl, B., Fazio, G. G., Hora, J. L., Gehrz, R. D., Helou, G., Soifer, B. T., Stauffer, J., Keene, J., Eisenhardt, P., Gallagher, D., Gautier, T. N., Irace, W., Lawrence, C. R., Simmons, L., Van Cleve, J. E., Jura, M., Wright, E. L., & Cruikshank, D. P. 2004, Astrophys. J. Suppl. Ser., 154, 1

White, S. D. M. & Frenk, C. S. 1991, Astrophys. J., 379, 52

White, S. D. M. & Rees, M. J. 1978, Mon. Not. R. Astron. Soc., 183, 341

Wright, E. L., Eisenhardt, P. R. M., Mainzer, A. K., Ressler, M. E., Cutri, R. M., Jarrett, T., Kirkpatrick, J. D., Padgett, D., McMillan, R. S., Skrutskie, M., Stanford, S. A., Cohen, M., Walker, R. G., Mather, J. C., Leisawitz, D., Gautier, T. N., McLean, I., Benford, D., Lonsdale, C. J., Blain, A., Mendez, B., Irace, W. R., Duval, V., Liu, F., Royer, D., Heinrichsen, I., Howard, J., Shannon, M., Kendall, M., Walsh, A. L., Larsen, M., Cardon, J. G., Schick, S., Schwalm, M., Abid, M., Fabinsky, B., Naes, L., & Tsai, C.-W. 2010, Astron. J., 140, 1868

Wu, H., Cao, C., Hao, C.-N., Liu, F.-S., Wang, J.-L., Xia, X.-Y., Deng, Z.-G., & Young, C. K.-S. 2005, Astrophys. J., 632, L79

York, D. G., Adelman, J., Anderson, Jr., J. E., Anderson, S. F., Annis, J., Bahcall, N. A., Bakken, J. A., Barkhouser, R., Bastian, S., Berman, E., Boroski, W. N., Bracker, S., Briegel, C., Briggs, J. W., Brinkmann, J., Brunner, R., Burles, S., Carey, L., Carr, M. A., Castander, F. J., Chen, B., Colestock, P. L., Connolly, A. J., Crocker, J. H., Csabai, I., Czarapata, P. C., Davis, J. E., Doi, M., Dombeck, T., Eisenstein, D., Ellman, N., Elms, B. R., Evans, M. L., Fan, X., Federwitz, G. R., Fiscelli, L., Friedman, S., Frieman, J. A., Fukugita, M., Gillespie, B., Gunn, J. E., Gurbani, V. K., de Haas, E., Haldeman, M., Harris, F. H., Hayes, J., Heckman, T. M., Hennessy, G. S., Hindsley, R. B., Holm, S., Holmgren, D. J., Huang, C.-h., Hull, C., Husby, D., Ichikawa, S.-I., Ichikawa, T., Ivezić, v., Kent, S., Kim, R. S. J., Kinney, E., Klaene, M., Kleinman, A. N., Kleinman, S., Knapp, G. R., Korienek, J., Kron, R. G., Kunszt, P. Z., Lamb, D. Q., Lee, B., Leger, R. F., Limmongkol, S., Lindenmeyer, C., Long, D. C., Loomis, C., Loveday, J., Lucinio, R., Lupton, R. H., MacKinnon, B., Mannery, E. J., Mantsch, P. M., Margon, B., McGehee, P., McKay, T. A., Meiksin, A., Merelli, A., Monet, D. G., Munn, J. A., Narayanan, V. K., Nash, T., Neilsen, E., Neswold, R., Newberg, H. J., Nichol, R. C., Nicinski, T., Nonino, M., Okada, N., Okamura, S., Ostriker, J. P., Owen, R., Pauls, A. G., Peoples, J., Peterson, R. L., Petravick, D., Pier, J. R., Pope, A., Pordes, R., Prosapio, A., Rechenmacher, R., Quinn, T. R., Richards, G. T., Richmond, M. W., Rivetta, C. H., Rockosi, C. M., Ruthmansdorfer, K., Sandford, D., Schlegel, D. J., Schneider, D. P., Sekiguchi, M., Sergey, G., Shimasaku, K., Siegmund, W. A., Smee, S., Smith, J. A., Snedden, S., Stone, R., Stoughton, C., Strauss, M. A., Stubbs, C., SubbaRao, M., Szalay, A. S., Szapudi, I., Szokoly, G. P., Thakar, A. R., Tremonti, C., Tucker, D. L., Uomoto, A., Vanden Berk, D., Vogeley, M. S., Waddell, P., Wang, S.-i., Watanabe, M., Weinberg, D. H., Yanny, B., & Yasuda, N. 2000, Astron. J., 120, 1579

Zabludoff, A. I. & Franx, M. 1993, Astron. J., 106, 1314

Zabludoff, A. I. & Mulchaey, J. S. 1998, Astrophys. J., 496, 39

Zamorano, J., Gallego, J., Rego, M., Vitores, A. G., & Alonso, O. 1996, Astrophys. J. Suppl. Ser., 105, 343

Zamorano, J., Rego, M., Gallego, J. G., Vitores, A. G., Gonzalez-Riestra, R., & Rodriguez-Caderot, G. 1994, Astrophys. J. Suppl. Ser., 95, 387

Zeldovich, Y. B., Einasto, J., & Shandarin, S. F. 1982, Nature, 300, 407

Zubko, V., Dwek, E., & Arendt, R. G. 2004, Astrophys. J. Suppl. Ser., 152, 211